

1 2 9 0



UNIVERSIDADE D
COIMBRA

Ricardo de Abreu Silvério Cabrita

**DIFFUSE REFLECTANCE STUDIES IN A LIQUID
INTERFACE**
WITH APPLICATION TO NOBLE LIQUID DETECTORS

Dissertação no âmbito do Mestrado em Física, ramo de Física Nuclear e de Partículas orientada pelo Professor Doutor Cláudio Frederico Pascoal da Silva e pelo Professor Doutor Vladimir Solovov e apresentada ao Departamento de Física da Faculdade de Ciências e Tecnologia.

Março de 2021

Master in Nuclear and Particle Physics

***DIFFUSE REFLECTANCE STUDIES IN A LIQUID
INTERFACE - WITH APPLICATION TO NOBLE LIQUID
DETECTORS***

by

Ricardo Cabrita

Supervised by Dr. Cláudio Silva and Dr. Vladimir Solovov



UNIVERSIDADE D
COIMBRA

DEPARTMENT OF PHYSICS
UNIVERSITY OF COIMBRA

March 2021

Acknowledgements

First I would like to thank my supervisors. Dr. Cláudio Silva, for his continuous support and guidance as well as his genuine readiness to teach. Dr. Vladimir Solovov for the opportunity to learn from his vast experience, objectiveness and extraordinary problem-solving skills. I also thank Dr. Vladimir for his great care and support as supervisor of my work with the Slow Control group of the LUX-ZEPLIN (LZ) collaboration.

I would like to thank Professor Maria Isabel Lopes for welcoming me into the Dark Matter group at LIP Coimbra and for her unwavering care and support ever since. I also thank the support and friendship of my colleagues from the Dark Matter group: Alexandre Lindote, Francisco Neves, Paulo Braz, Elias Asamar, Guilherme Pereira and Davide Porzio. Special thanks to Guilherme, for making me feel welcome in LZ and showing me the ropes to Ignition and, to Davide, for his support in the lab work. I would also like to thank all my colleagues from the LUX-ZEPLIN collaboration, it has been a privilege to work with everyone.

This thesis would not have been possible without the help, support and dedication of the colleagues from the LIP workshop. Special thanks to Alberto Blanco, Rui Alves, Américo Pereira, Nuno Dias and Carlos Silva.

I also would like to thank all the friends I made over the last few years in the Master and Nuclear Particle Physics. To name just a few: Andrey, Cédric, Marcela, Jacinto, Filipe, Euclides, Joaquim, Susana — you have made this journey far more interesting and fun.

Last, but not least I thank my parents for their love and support, and my brother for his kindness and advice. Finally, I thank Maria for her warm, patient friendship and loving support.

Abstract

Noble liquid xenon and argon detectors are being used in particle and astroparticle physics, including dark matter direct detection experiments and neutrino physics. Polytetrafluoroethylene (PTFE) is commonly used in these detectors as a reflector to improve the light collection and, consequently, the experiment sensitivity. As such, describing the reflectance from the surfaces encasing a detector is paramount. For the xenon scintillation wavelength (175 nm), PTFE is known to have a reflectance of 50–80% in gaseous xenon. In liquid xenon, however, it has been observed to be >95%. The reason for such an increase in reflectance is still unclear.

Additionally, optical simulations of noble liquid detectors generally model the reflectance of PTFE according to the Lambert diffuse law. Observations indicate, however, that reflection from diffusers like PTFE and others most often deviates significantly from Lambertian behaviour. In truth, a fraction of specular reflection is always present due to the change in refractive index at the interface. Surface roughness also contributes to this deviation, due to masking, shadowing and interreflection effects. Finally, there is also total internal reflection at the optical interface to take into account.

In this work, we report on an experimental study of reflectance in a liquid-PTFE interface. A dedicated experimental set-up was designed, from inception to completion, to measure the change in the reflectance when the medium interfacing PTFE changes from air to liquid. To that end, a Spectralon® (PTFE-based) total integrating sphere was adapted for use with liquid. The set-up also includes an array of 7 LEDs covering the wavelength range 255–490 nm, a photomultiplier to detect the reflected photons, and a time resolved data acquisition system. Experimental data for the reflectance of the sphere walls was taken with the sphere filled in turn with air and pure water. The experimental data was compared with the results of simulations of light collection in the geometry of the experimental set-up with the help of the ANTS2 software package. In those simulations, different models of diffuse reflection were tested, namely the Lambertian model and a modified version of the Wolff model, which includes the Fresnel reflection at the interface.

Analysis with the Lambertian model indicates a clear increase in the bi-hemispherical reflectance in the pure water interface, $+2.94 \pm 0.03\%$ at 255 nm and $+1.09 \pm 0.08\%$ at 490 nm. The increase in the multiple scattering albedo in the modified Wolff, which is independent of the optical interface, suggests that the enhancement of reflection in the liquid interface may be due to other parameters besides the changing refractive index. Based on the developments made in the course of this work, the upgrade of the set-up is planned, after which it will be used to take more measurements with various liquids and material samples, following up on the initial results of this work.

Resumo

Os detectores de xénon e argon líquidos são utilizados em física de partículas e astropartículas, nomeadamente em experiências de detecção directa de matéria escura e física de neutrinos. Normalmente, politetrafluoretileno (PTFE) é utilizado como reflector nestes detectores de forma a melhorar a colecção de luz e, conseqüentemente, a sensibilidade da experiência em questão. Desta forma, descrever a reflectância das superfícies que envolvem o detector é fundamental. Para o comprimento de onda de cintilação do xénon (175 nm), sabe-se que o PTFE tem uma reflectância entre 50–80%. No entanto, em xénon líquido, a reflectância observada é acima de 95%. A razão para um aumento tão demarcado da reflectância não é clara.

Adicionalmente, regra geral, as simulações de óptica de detectores de líquidos nobres simulam a reflectância do PTFE de acordo com a lei difusa de Lambert. No entanto, observações indicam que difusores como o PTFE e, outros, têm um comportamento diferente do Lambertiano. Na verdade, está sempre presente uma componente de refração especular devido à alteração do índice de refração no interface. A rugosidade da superfície também contribui para esta diferença devido a efeitos de obscurecimento, sombreamento e inter-reflexões. Finalmente, há que também ter em conta o fenómeno de reflexão interna total no interface óptico.

Neste trabalho, é reportado um estudo experimental da reflectância no interface líquido-PTFE. Para o efeito, foi concebido e desenvolvido um *set-up* experimental dedicado para medir a alteração na reflectância quando o interface muda de ar para líquido. Uma esfera integradora de Spectralon® (à base de PTFE) foi adaptada para uso com líquidos. O *set-up* também inclui uma matriz de 7 LEDs nos comprimentos de onda 255–490, um fotomultiplicador para detectar os fótons reflectidos e um sistema de aquisição de dados resolvido no tempo. Medidas da reflectância da superfície interna da esfera foram feitas, à vez, com a esfera cheia de ar e àgua pura. Os dados experimentais foram comparados com os resultados da simulação de colecção de luz para a geometria da experiência com o programa de simulação ANTS2. Nessas simulações diferentes modelos de reflexão difusa foram testados, nomeadamente o modelo Lambertiano e uma versão modificada do modelo de Wolff, que inclui reflexão de Fresnel no interface.

A análise com o modelo de Lambert indica um claro aumento da reflectância bi-hemisférica no interface de àgua pura, $+2.94 \pm 0.03\%$ a 255 nm e $+1.09 \pm 0.08\%$ a 490 nm. O aumento no albedo de espalhamento múltiplo com o modelo modificado de Wolff, que é independente do interface óptico, sugere que o aumento da reflectância no interface líquido se poderá dever a outros parâmetros para além do índice de refração. Com base nos desenvolvimentos deste trabalho um conjunto de melhoramentos ao *set-up* foram planeados, após os quais mais medidas com vários líquidos e amostras de várias materias se seguirão.

TABLE OF CONTENTS

List of Figures	v
List of Tables	ix
1 Introduction	1
1.1 Main Contributions	3
1.2 Dissertation Outline	4
2 PTFE Reflectance in the Context of Noble Liquid Particle Detectors	5
2.1 Energy Transfer in Noble Liquids	6
2.2 Particle Physics with Noble Liquid detectors	7
2.3 PTFE Reflectance Measurements for LNG Detectors and Diffuse Reflectance Modelling	12
3 Optics, Radiometry and Reflectance	19
3.1 Reflection and Refraction of Plane Waves	20
3.2 Reflection in Radiometry	25
3.3 Diffuse Reflectance	29
3.4 Reflection from Rough Surfaces	34
3.5 The Wolff and Oren-Nayar Model	39
4 Experimental Set-up and Simulations	42
4.1 Experimental Set-up Overview	42
4.2 The Total Integrating Sphere	44
4.3 Adapting the TIS for a liquid interface	47
4.4 The LED matrix and the collimation system	50
4.5 Photon Propagation Inside the Total Integrating Sphere	56
5 Measuring Reflectance in a Liquid Interface	61
5.1 Experiment Control	61
5.2 Photodetection and Data Acquisition	63
5.3 Measuring the Reflectance of the TIS	68
5.4 Measuring the input flux	70
5.5 Designing a New Set-Up: continuous input flux measurements	71
6 Results and Data Analysis	73
6.1 Measurements of the Incident Flux	73
6.2 Measurements of the Flux in the Total Integrating Sphere	74
6.3 Analysis with a Monte-Carlo simulation in ANTS2	76

7	Conclusions and Future Work	81
----------	------------------------------------	-----------

List of Figures

2.1	Schematic of scintillation light generation in noble liquids.	6
2.2	Exclusion limits for the spin-independent WIMP-nucleon cross section set by past experiences as well as LZ's projected sensitivity. From [49]. . . .	8
2.3	Simplified view of an event in a dual-phase TPC from [19]	10
2.4	Renderig of the LZ detector from [1]. (1) LXe TPC; (2) GdLs Outer detector; (3) Outer detector PMTs; (4) Water which proved shielding and Cherenkov radiation based veto; (5) Cathode high voltage connection; (6) pipe for deployment of neutron calibration sources.	12
2.5	Hemispherical reflectance factor of PTFE measured with a total integrating sphere and a collimated source with incident angle of 6° with respect to the sample surface normal to make sure specular reflectance is included in the measurement. From [14]	13
2.6	From the LUX III run analysis [13], χ^2 map for PTFE reflectivity and LXe absorption length, the two free parameters with greatest impact on light collection.	14
2.7	Cross section diagram of the test platform TPC and the cathode high-voltage feed-through from [19]. Detail of the ring based PTFE structure can be seen. The liquid xenon skin around the TPC is shown too.	15
2.8	3D view (left) and schematic illustration (right) of the chamber for measuring the PTFE reflectance in LXe. The ^{241}Am source is shown placed below the top wall, and the PMT positioned at the bottom. From [12].	16
2.9	Hemispherical reflectance versus incident angle [64]	17
3.1	Left: separation of an incident plane wave into a transmitted and a reflected wave according to Snell-Descarte's laws. Right: illustration of Fermat's principle of least time applied to the law of refraction.	20
3.2	Reflection and refraction on the plane of incidence (XOZ). Boundary plane $z = 0$. From [68].	22
3.3	The three components of reflection. The diffuse component is centred around the normal while the specular components are centred around the specular direction (from [16]).	25
3.4	Definition of angles and solid angles relevant for radiometry in the general case where sub-surface scattering is also taken into account (adapted from [70]).	26
3.5	Example of common reflected and incident beam geometries (from [18]).	28
3.6	Geometric refraction of incident light and outgoing light after multiple subsurface scatterings.	30

3.7	Fresnel transmittance coefficient into/from the dielectric according to Fresnel coefficients for wavelength of 380 nm. Legend shows the refractive indexes used.	31
3.8	Parallel plane geometry and angle definitions in radiative transfer theory (adapted from [75]).	32
3.9	Chandrasekhar's isotropic diffuse reflection at normal viewing for multiple albedos over the range of incident angles, compared with Lambertian reflection (dashed) (borrowed from [20])	34
3.10	Illustration of a v-cavity and the dependence of reflected light on viewing angle. From [24]	37
3.11	Geometry of rough surfaces. Note that if reflection is considered specular, then $\theta'_i = \theta'_r = \theta'$. Masking and shadowing effects are illustrated too.	38
3.12	Schematic of internal scattering in the bulk of material, showing multiple reflections in the dielectric/air interface (from [16]).	39
4.1	Photo of the experimental set-up inside the optical chamber: (1) LED matrix; (2) diffuser window; (3) first pinhole; (4) second pinhole; (5) light input port with a fused quartz window and Spectralon® pinhole on the inside; (6) Integrating Sphere; (7) PMT holder piece, also from where the sphere is filled with liquid; (8) PMT and PMT base.	43
4.2	Exchange factor in a spherical geometry.	45
4.3	On the left a scheme (top view) of the sphere is given, from the Newport website [92]. On the right the top view of the 3D cad model is shown, with the 4 ports identified.	47
4.4	Schematic views of the PMT holder: (left) the front view of all the pieces including the PMT; (middle) PTFE adaptor piece attached to the sphere port 90 deg; (right) left-handed vertical section of the middle piece, rotated for legibility.	48
4.5	close up of the PMT holder with the holding posts to fix the PMT in position. The wiring on top is for base biasing and grounding of the posts.	49
4.6	Light input port filled with water on the interior of the fused quartz window interface. The back of the pinhole can be seen, which is made of POM plastic with multiple creases to form a light trap.	50
4.7	3D CAD picture of the internal pinhole: (left) front; (centre) back; (right) cross section. The front piece is made of Spectralon® while the back piece is a light trap made of black POM. The evacuation canals on the outside of the piece can be seen. These are used to guarantee the space is completely filled with water without any air bubbles.	51
4.8	Photo of the PCB matrix. The three DIP LEDs were tilted ($\sim 8^\circ$) towards the centre of the diffuser, which was 50 mm away.	52
4.9	Schematic cross-section of the experimental set-up, including details of the collimation system, with the baffle in the sphere's interior not shown for simplicity.	52
4.10	The geometric positioning of the LEDs in the PCB Matrix and reference axes used in simulations.	53
4.11	Polar angle distributions with respect to the direction of propagation after the diffuser. The histogram is not centred around 0 due to an effect of the solid angle, proportional to $\sin \theta$	55

4.12	Polar angle distributions with respect to the direction of propagation after the two pinholes. Histograms are normalised for each LED for comparison.	55
4.13	Scatter plot of the photon (x,z) "spot" distribution on the plane of the Spectralon® pinhole at y = 279 mm.	56
4.14	Geometry of the experiment implemented in ANTS2 as seen in the geometry visualisation window in the ANTS2 graphical user interface. The red lines show the optical path of a photon with multiple reflections before being detected.	57
4.15	Top panel shows the average distance travelled by detected photons in a non-absorbing medium for increasing Lambertian albedo (simulated for the TIS geometry in ANTS2). Bottom panel shows the absorption length values for pure water taken from literature [96, 97, 98].	60
5.1	Photo of the Arduino shield for controlling the LEDs. The axial through-hole resistors are switched depending on the LEDs being used.	62
5.2	Schematic of the LED shield: the encoder output is connected to the input of the buffer channels, which are shown individually instead of a monolithic IC view, for clarity. Some of the buffer channels are wired together to allow for a higher current load.	62
5.3	Diagram and photo of the electronic set-up for photon counting with the PMT.	64
5.4	Photo of a typical photon pulse signal after amplification as seen on the oscilloscope.	65
5.5	Schematic of the voltage divider base used with the R762P PMT from Hamamatsu®.	66
5.6	Example plot of time-stamp difference between two consecutive photons in ns. Example signal acquired with the PMT on top of the sphere with LED 255 nm on.	67
5.7	The dependence of the rate of observed photons on the true rate of photons.	67
5.8	Set-up for measuring the input flux of photons, the PMT is installed horizontally on the 0° (1.5") port. Photo was taken with the optical chamber open. Measurements are of course done with the chamber closed, in the dark.	70
5.9	Schematic top-view of the new experimental set-up proposed. The beam sampler and the second PMT are shown.	72
6.1	Attenuation factor, Φ_{in}/Φ_{TIS} in air and water interfaces. Computed for all runs, both high and low counts.	76
6.2	Reflectance factor obtained for the analytic method and a simulation with the Lambert model in ANTS2. The calibration reference values from Lab-sphere are shown for comparison [115].	77
6.3	Lambertian albedos estimated in ANTS2 simulations in both air and water interfaces in accordance with the attenuation factors obtained experimentally.	78
6.4	On the left, Fresnel transmission coefficient at the optical interfaces. On the right the refractive index for different wavelengths.	79
6.5	Multiple-scattering albedo from the Wolff model estimated in ANTS2 simulations in both air and water interfaces according to the attenuation factors obtained experimentally.	79

6.6	Dependence of the multiple-scattering albedo of the Wolff model on the absorption length of water, for the 255 nm wavelength.	80
-----	---	----

List of Tables

2.1	Comparison of dual-phase TPC detectors for WIMP SI search	9
2.2	Best fit values of the optical parameters in the LZ System Test optical simulations [19]	16
2.3	Reflection values for various PTFE samples and interfaces.	18
4.1	Roithner® LEDs used in the experiment.	51
4.2	Fraction of photons through both pinholes for each LED configuration . .	55
4.3	Materials definitions in ANTS2, for 255 nm and 405 nm[*]	58
5.1	Arduino commands for experiment control	63
5.2	LED configuration used in data taking.	69
6.1	Incident flux measurements for each LED.	74
6.2	Photon fluxes measured in the TIS for each LED (high counts).	75
7.1	Possible liquids to be used in the TIS	83

Chapter 1

Introduction

Noble liquid scintillation detectors are at the forefront of particle and astroparticle physics, contributing to dark matter searches [1, 2], detection of coherent elastic neutrino-nucleus scattering (CE ν NS) [3], searches for neutrinoless double beta decay [4], and detection of rare nuclear decays [5, 6].

Dark matter is one of the essential ingredients of the standard cosmological model [7]. Although compelling clues abound at all astrophysical scales, its nature has remained a mystery since Fritz Zwicky first suggested its existence in 1933 [8]. A classical particle dark matter candidate is the Weakly Interacting Massive Particle (WIMP). This particle candidate gained relevance due to the realisation that the annihilation cross-section at the electro-weak scale naturally leads to the appropriate relic abundance as determined by cosmological evidence [9]. Most developments in noble liquid detectors in the last decades were made with the detection of WIMPs in mind [10, 11]: allured by the prospect of solving the mystery of dark matter and, at the same time, opening a door to new physics at the electro-weak scale.

Detection of CE ν NS and WIMPs share many similarities. Both are cases of low energy interactions that profit from the coherence of the scattering across all nucleons in the nucleus, and thus their interaction requires similar treatment [10]. The study of CE ν NS has the potential to constraint or present proof of a fourth sterile neutrino or gain an understanding of neutrino dynamics in neutron stars and supernovae [10].

A new generation of detectors, such as LUX-ZEPLIN and XENONnT, are currently being developed to search for dark matter and neutrinoless double beta decay [1, 2]. These noble liquid detectors are looking to detect rare events with small interaction cross-sections in a large amount of background. To that end, thorough background and data analysis and a deep understanding of the detector's optical response are necessary. Understanding and modelling light collection is part of that effort. The performance parameters of these detectors, such as energy resolution, discrimination, and sensitivity, depend on the collection of scintillation light, which, in turn, depends on the reflectance of the material around the active region of the detector [12, 13]. Most often, tetrafluoroethylene, (C₂F₄)_n (PTFE, commonly used trade name Teflon®), is the reflector of choice to encase the target liquid. The main reason for that is its very high reflectance for a broad range of wavelengths, $\sim 99\%$ in the 350–800 nm range [14], combined with its high chemical stability and relatively low outgassing [15].

The reflection of PTFE is mostly of a diffuse nature. In contrast to specular reflection, which occurs at the interface between two media, diffuse reflection occurs in the interior of the material. Discontinuities in the refraction index in the bulk of the material cause

the light to scatter multiple times, before being absorbed or refracted back to the first medium [16].

For the xenon scintillation light (175 nm in gas, 178 nm in liquid [10]), there is a puzzling difference between the values of the reflectance of PTFE, reported to be 50–80% in the gaseous xenon phase [17, 18], versus 95–99% in the liquid xenon (LXe) phase [12, 13, 19]. The diffuse reflectance is expected to be enhanced by matching of the refractive indices of the two interfacing media, since more light gets transmitted into the diffuser and light also gets back to the original medium more easily [20]. However, it is still unclear what prompts such a significant increase in the observed reflectance [12]. Diffuse reflectance models fail to accurately extrapolate the reflectance in the liquid interface from the value in air, underestimating the reflectance values observed experimentally [16].

Detector simulations of the encasing PTFE surfaces generally model its reflectance according to the Lambert model [13, 21], which models diffuse reflection so that a reflecting surface appears equally bright independently of the viewing angle [22]. It is important to note that the Lambert law is an ideal approximation since there will always be a fraction of specularly reflected light due to the difference in the refractive index at an optical interface, as mediated by the Fresnel equations. In fact, significant deviations from Lambertian behaviour were observed for PTFE and other diffuse reflecting surfaces [12, 23]. Reasons for these deviations can be possible due to surface roughness or even the internal structure of the diffuser [24, 20].

Note that while these considerations do not apply directly to the standard liquid argon (LAr) detectors, there are plans for future detectors where small amounts of xenon are added to the LAr, shifting the scintillation peak wavelength from 128 nm to 175 nm [25]. In these cases, the discussion of PTFE reflectance to the VUV in a liquid interface is equally relevant. Of course, LAr's optical properties are different from LXe, which affects the PTFE reflectance in the doped LAr medium.

This thesis' main objective is to study the diffuse reflectance of PTFE in a liquid interface. To that end, a dedicated experimental set-up was designed, from inception to completion, that allows measuring the change in reflectance when the interface changes from air to liquid. A total integrating sphere (TIS) with inner walls of Spectralon® (pressed PTFE) was used. Spectralon® is often used as an optical calibration reference in photometry and radiometry applications [26, 27]. Total integrating spheres are generally used to measure the total scattering of light, being employed in many applications such as rating the radiated power of lamps or measuring the transmittance or reflectance of various samples [28, 17]. The sphere was adapted for use with liquids, with two custom port pieces: one to interface the sphere with the collimation light system and another to fit a photomultiplier to detect the reflected photons. A set of seven LEDs were used to cover the wavelength range of 255–490 nm. The photon flux in the sphere after multiple reflections was measured both in air and pure water (type II [29]). The incident flux from the collimation system into the sphere was also measured.

The ANTS2 software package [30] was used to simulate the total integrating sphere set-up. Two diffuse reflectance models, the classic Lambertian model and a modified version of the Wolff model [31, 16], were used to reproduce the experimental results. ANTS2 is an optical simulation package that has been used to study anger camera type detectors [30], design the PMT arrangement for the LUX-ZEPLIN dark matter experiment [32] and in optical simulations of an experiment to measure the reflectance of PTFE in LXe [12].

There is also added value to this work outside the field of scintillation detectors. In the field of computer graphics and computer vision, an understanding of diffuse reflectance in a liquid interface and validation of the existing models is extremely important. For example, to improve life-like graphical simulations of reflections in liquid media, or to improve existing computer vision techniques that need to deal with diffuse reflectance. Many algorithms fundamentally rely upon assumptions about the nature of diffuse reflection from everyday dielectric materials, some examples are shape-from-shading, photometric-stereo and photometric-based binocular stereo algorithms [31].

Finally, there is interest in modelling the reflection of Spectralon® itself, since it is the best known diffuser material in the visible range [27]. It has been widely used in remote sensing and space applications, most often as a calibration reference, so there is great interest in modelling its reflectance as past efforts show [27, 26].

1.1 Main Contributions

In this work, we designed, developed and built a dedicated experimental set-up, using a total integrating sphere, to measure the reflectance of PTFE in air and different liquid media.

The experiment uses a photon-counting set-up with a PMT to measure the output photon fluxes after multiple reflections off the inner surfaces of the TIS. This method achieved good stability and linearity. Measurements of the photon flux in both air and pure water were seen to be consistent for the multiple data taking runs performed over the period of a few weeks. The experimental set-up appears to be mechanically stable and there is no indication of significant systematic errors (either from unwanted reflections in the collimation system, geometry instabilities or contamination of the inside of the sphere).

Monte Carlo (MC) simulations in ANTS2 using detailed geometry of the experimental set-up were developed to reproduce the experimental data. The simulations permitted to test different diffuse reflectance models. In this work, the Lambertian model and a modified version of the Wolff model were tested.

From the analysis of the experimental data with the MC simulations in ANTS2, it is clear that the reflectance increases for a liquid interface. Using the Lambert model for analysis, which can be directly compared with past measurements, an increase in the bi-hemispherical reflectance of the PTFE in water was observed, $2.94 \pm 0.03\%$ at 255 nm and $1.09 \pm 0.08\%$ at 490 nm. This is in good agreement with what was observed in [33] for a Spectralon® plate submerged in water, an increase of about 2% at 633 nm.

Analysis with the modified Wolff model fitted the multiple scattering albedo, which is the probability of a scattered photon inside the diffuser makes it to the interface between the diffuser and the original medium without being absorbed. This quantity is independent of the optical interfaces and a function only of the scattering and absorbing properties of the material. A small, but clear increase was seen for the multiple scattering albedo with the changing interface. This may indicate that other parameters maybe relevant for diffuse reflectance in a liquid interface besides the changing refractive indices. Further studies of the effect of the roughness of the surface might explain this observation. Trying out different internal scattering models, like the Chandrasekar model [34] might also be of interest.

Measuring the reflectance of PTFE in LXe is difficult, especially due to uncertainties

in the absorption length of LXe, which depends on the purity of the xenon being used. A degeneracy in the reflectance of LXe-PTFE interface and the absorption length of LXe makes it difficult to set an upper limit on the value of the reflectance [13], even with dedicated experiments [12]. Our set-up is less dominated by the absorption length of liquids since the integrating sphere is of relatively small size, 3.3" diameter, and to that regard, the ability to test multiple liquids is also an advantage.

The possibility of making measurements with different liquids is an opportunity to further understand the diffuse reflectance of PTFE in a liquid interface without the difficulties of using LXe. Besides the tests already done with pure water, future tests with this set-up and analysis methods are in line with ethanol and glycerine. It will be very interesting to verify whether other physical parameters, like polarity of the liquid molecules, might have an impact on diffuse reflection in a liquid interface.

Ultimately, the experimental set-up and simulation analysis developed in this thesis can be used to test the diffuse reflection of various material samples in various liquids and even test custom empirical models before they are to be used in simulations of diffuse reflection for a noble liquid detector.

1.2 Dissertation Outline

This thesis is organised into seven chapters. The first one and present chapter is the Introduction. Chapter two gives a brief of review of noble liquid detectors and their applications as well as the relevance of the diffuse reflection of PTFE in optical simulations of these detectors. Additionally, a review of experimental measurements of PTFE reflectance in LXe is presented. Chapter three introduces theoretical notions of radiometry, the reflection of plane waves and the modelling of diffuse reflection relevant to the present work.

Chapter four describes the design and implementation of the experimental set-up as well as the simulations developed in the course of this work. This includes ray tracing simulations to understand the light input to the total integrating sphere, as well as the Monte Carlo simulations of the total integrating sphere in ANTS2. Chapter five describes the technical developments for the experiment control system and data acquisition. It also describes in detail how the experimental measurements were performed, both for the incident flux and for the output flux resulting from multiple reflections inside the TIS .

The experimental results are detailed in chapter six as well as their analysis in ANTS2. Finally, chapter seven concludes this thesis with a summary of the results and conclusions reached and a brief overview of future prospects in the context of the work developed here.

Chapter 2

PTFE Reflectance in the Context of Noble Liquid Particle Detectors

Since the 1970's that liquefied noble gases (LNGs) have played a substantial role in experimental particle physics. The good scintillation properties of these liquids allied with the fact that ionisation electrons can remain free to be drifted across considerable distances favour them as unique detection mediums. Due to low electron diffusion, noble liquids lend themselves well to particle tracking. In addition, they also offer good energy resolution, with great benefit for spectrometry applications [10].

The two noble liquids which have seen more applications in experimental physics are liquid xenon (LXe) and liquid argon (LAr). These applications include γ -ray astrophysics [35], neutrinoless double beta decay [36], dark matter searches and coherent elastic neutrino-nucleus scattering ($CE\nu NS$) [37, 3].

The last three, dark matter in the form of WIMPs, $CE\nu NS$ and neutrinoless double-beta decay, are expected to have very low interaction rates and, for that reason, dealing with backgrounds is of critical importance [10]. Besides background reduction (radio-cleanliness, passive shielding) and vetoing systems (liquid scintillator), particle tracking and position reconstruction is very important. A good estimation of the position of the detected interactions allows for the selection of events within a background free (or at least a region where the background is very well known/controlled), fiducial volume: away from the walls of the detector for example. This is achieved through the detection of both the scintillation and ionisation electrons in Time-Projection Chambers (TPC) [38].

In both cases of WIMPs and $CE\nu NS$, the deposited energy is very low and the sensitivity of the detector is limited in the amount of photons that arrive at the photodetectors. So, in terms of the scintillation light, maximising its collection is of extreme importance to decrease the energy threshold of the detector [10]. For this reason, detectors that depend on the scintillation signal generally surround the target medium with an efficient reflector material, in most cases, PTFE [39, 2].

Naturally, Monte Carlo (MC) simulations of these detectors need to consider the PTFE reflectance as it affects the light collection, which impacts the energy resolution, discrimination, and sensitivity of the detector [40, 12].

In the visible range, PTFE displays a very high reflectance around 99% [14]. However, for the xenon scintillation wavelength, 175 nm, it has been estimated between 50% and 80% [17, 18]. When measured in LXe however, much higher values of PTFE reflectance, in the range 95–99%, were reported [12, 13, 19]. For this reason, in this review, we will focus more on LXe detectors, for which the impact of PTFE reflectance in a liquid

interface is especially relevant.

Recent developments in LAr detectors use small amounts of xenon to dope the LAr, shifting the scintillation peak wavelength from 128 nm to 175 nm [25]. For this use case, the discussion regarding PTFE reflectance to VUV in a liquid interface is equally relevant.

First a brief description of the particle energy transfer mechanisms in noble liquids is given. Then, the operating principles and scientific opportunities of noble liquid detectors are reviewed. Finally, a discussion on recent studies of PTFE diffuse reflectance and its application to this type of detectors are presented.

2.1 Energy Transfer in Noble Liquids

As illustrated in figure 2.1, energy deposited in a noble liquid develops through three channels - excitation, ionisation and heat. Excitation leads to scintillation through intermediate creation of excimers – metastable excited dimers [11]. Upon return to the ground state, these excimers dissociate, releasing scintillation photons in the process. Their decay rate depends on if they are in singlet or triplet states. Triplets are naturally slower to decay, ~ 1500 ns in LAr and ~ 22 ns in LXe, against ~ 7 and ~ 4.5 ns for the singlet states, respectively [10]. Because the ratio of triplet to singlet states depends on the dE/dx of the incoming particle, the timing of the scintillation profile can be exploited to great effect in pulse shape discrimination. The relative weights of the three channels, excitation, ionisation and heat, are also dependent on the incident particle’s energy and the kind of interaction. For example, in nuclear recoils (NR), a large fraction of the deposited energy translates as heat due to elastic scattering of the nuclei; the same is not true for electronic recoils. It is important to note that as the scintillation light is produced by excimer emission, its photon energy is lower than the excitation energy of the corresponding noble gas atoms. As a result, the LNG are highly transparent to their own scintillation light, allowing for efficient light collection even for large volumes [41].

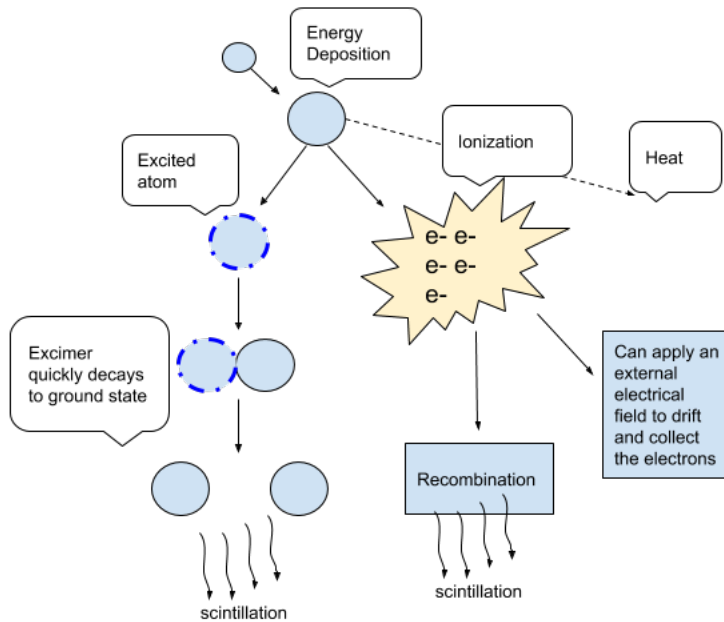


Figure 2.1: Schematic of scintillation light generation in noble liquids.

Ionisation kicks off a number of electrons from the atoms. In the absence of an electric field, they will eventually recombine with positive ions, giving rise to more excited atoms and more excimers that will relax to the ground state through the same scintillation process (although the fraction of triplet and singlet states is not exactly the same). Recombination is an inverted parabola, $\sim t^{-2}$, and in the case of LXe, it is notably slower than the de-excitation times of the excimers. It is in the order of ~ 1 ns in the case of LAr, while in LXe there are reports of average recombination times of 34 ns and 45 ns, but a 1% tail of electrons has been observed to take up to $2 \mu\text{s}$ to recombine [10]. Most of the times, however, detectors will employ external electric fields to drift the ionisation ions into a collection grid, competing against the process of recombination.

Instead of collecting the ionised charge via some collection grid, some detectors combine a gaseous phase to exploit its electroluminescence effect. Electrons that go through the phase barrier are accelerated by applying an electric field, exciting the gaseous atoms and originating a great amount of VUV photons in the process. Dual-phase time projection chambers, as we will see next, exploit this ability to great effect. Not only the ionisation signal is amplified, but it can also be detected with the same PMTs used to collect the initial scintillation in the liquid phase [10].

On a final note, energy transfer mechanisms in LNG are very complex and this is but a brief overview of the subject. There are other relevant effects, such as the effect of quenching when excited species collide with each other, suppressing the scintillation signal. Another thing that affects the dynamics of signal generation is the impurities in the liquid medium. Any detector and ensuing analysis must, of course, account for all of these details [42].

2.2 Particle Physics with Noble Liquid detectors

In this chapter, we will mainly focus on the developments concerning dual-phase detectors, which are the detectors leading the search for dark matter. The current highest sensitivity to WIMPs is held by the XENON1T detector, a xenon dual-phase time projection chamber (TPC) chamber [43]. The expected WIMP signature is a nuclear recoil in the keV range (up to 100 keV), for the expected WIMP mass range between 10 and 100 GeV [44]. The recoil spectrum from CE ν NS is similar, with recoil energies up to the tens of keV for high energy neutrinos [45], and sub-keV for reactor antineutrinos [46].

Another link between the detection of CE ν NS and dark matter searches is that in future WIMP detection experiments, CE ν NS by atmospheric neutrinos will be a dominant background source [47]. This is depicted in figure 2.2 in the form of the “Neutrino Discovery Limit” curve. If it turns out necessary to look for dark matter below the neutrino floor, a thorough understanding of CE ν NS in LNG detectors will be essential.

The first detection of CE ν NS on liquid argon nuclei was recently published by the COHERENT collaboration [3]. It used a single-phase 24 kg LAr detector, encased in a PTFE reflective chamber. The first run in high-energy-threshold mode constrained an upper limit on the CE ν NS cross section and quantified background sources. An upgrade of the detector resulting in an eight-fold improvement in light collection efficiency allowed for a lower energy threshold which yielded this result [48].

The CE ν NS interaction is uniquely sensitive to N^2 (number of neutrons in the nucleus) and the nuclear neutron distribution, so this result is especially important to help settle standard model uncertainties in neutron distribution on argon [3]. It is also sensitive to

non-standard neutrino quark interactions and this result has already helped to constrain the degeneracy of non-standard interactions in neutrino mass ordering experiments, which will greatly help future neutrino oscillation experiments [48].

Generally, in the case of WIMP searches, detection limits are computed for spin-independent (SI) and spin-dependent (SD) interactions. While the SI cross section does not depend on the net spin of the target nucleus, SD analysis considers the possibility of the WIMP coupling to the nucleon's spin instead of its mass. Figure 2.2 shows a comparison of the exclusion limits for SI WIMP-nucleon interactions set by different past experiments as well as the projected sensitivities for the upcoming LZ experiment [49]. Moreover, the DARWIN experiment, a next-generation 40-tonne LXe detector still in the conceptual design phase, is expected to push these limits further down and into the neutrino floor [50].

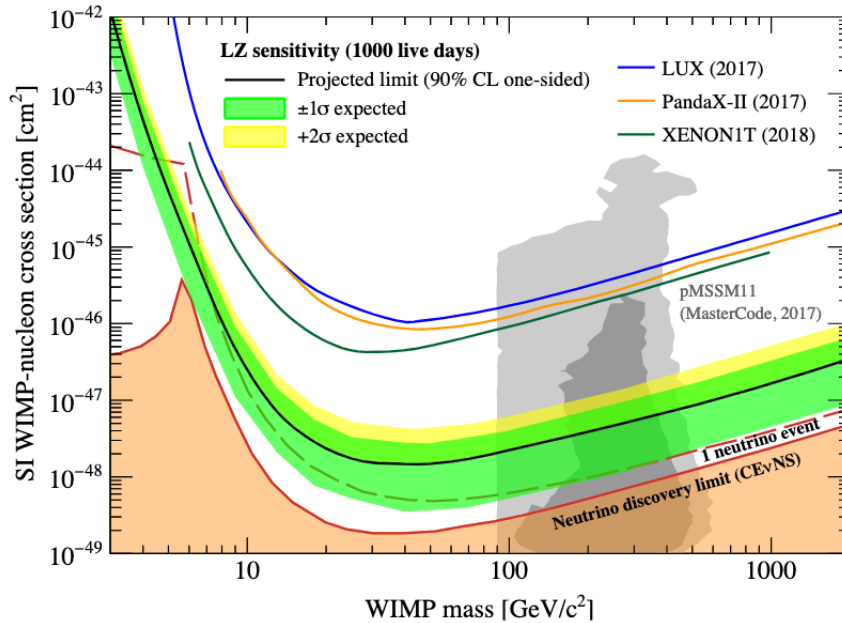


Figure 2.2: Exclusion limits for the spin-independent WIMP-nucleon cross section set by past experiences as well as LZ's projected sensitivity. From [49].

For dark matter masses increasingly below the mass of the Xe nucleus ($A=131.293$), the recoil energy from the nuclear recoil quickly gets below the energy threshold of these detectors. However, upon an elastic nuclear scattering, the Xe nucleus suffers a sudden momentum change with respect to the orbital atomic electrons. This results in perturbations in the atom electron shells which, it turn, may lead to electron emission, enhancing the signal resulting from the original nuclear recoil. This is called the Migdal effect [51]. Current dual-phase TPC detectors have exploited the Migdal effect in their analysis being able to probe down to mass ranges outside of the traditional WIMP scope. Recent analysis with data from the LUX experiment resulted in exclusion limits for masses from 0.4 to 5 GeV [49], while another sub-GeV analysis with the XENON1T detector yielded exclusion limits for masses as low as 85 MeV [43].

Additional novel physics within reach of these detectors are, for example, solar axions [52] and neutrinoless double beta decay in ^{136}Xe [4]. Neutrinoless double beta decay is a theorised type of double beta decay in which the only emitted products are two electrons. This can only happen if the neutrino is its own anti-particle (Majorana particle), allowing

it to be emitted and absorbed within the nucleus. This is considered to be the most precise probe of the neutrino mass scale and, if detected, would prove the neutrino to be of Majorana nature resulting in a major breakthrough in neutrino physics [36].

Due to the large volumes involved, there is also opportunity to measure rare decay events. A recent success in this area came from the XENON collaboration which reported for the first time the observation of two-neutrino double electron capture, where two protons form two neutrons by capturing two orbital electrons, in ^{124}Xe with the XENON1T detector. This is the radioactive decay with the longest half-life ever detected, 1.8×10^{22} years [5].

In the field of dark matter search, LUX-ZEPLIN (LZ), XENONnT, and PandaX-4T, still under development but close to completion, are expected lead the field employing LXe and a dual-phase TPC [39, 2, 53]. Using LAr, DarkSide-20k, another dual-phase TPC currently under development, is expected to have high sensitivity to high mass WIMP candidates [38]. Table 2.1 summarises the noble liquid active masses and expected sensitivities to WIMP of these detectors [49, 54, 53, 38].

Table 2.1: Comparison of dual-phase TPC detectors for WIMP SI search

Detector	active mass (t)	max. sensitivity (cm^2)	exposure (t·year)	
LZ (LXe)	7 (5.6 fiducial)	1.4×10^{-48} (40 GeV)	15	[49]
XENONnT (LXe)	6 (4 fiducial)	1.4×10^{-48} (50 GeV)	20	[54]
PandaX-4T (LXe)	4 (2.8 fiducial)	6×10^{-48} (40 GeV)	5.6	[53]
DarkSide-20k (LAr)	23 (20 fiducial)	1.2×10^{-47} (1 TeV)*	100	[38]

* DarkSide-20k plans in the future to further deplete the LAr of ^{39}Ar (it's a source of backgrounds), and with an increased exposure of 200 t·year, would yield a maximum sensitivity of 7.4×10^{-48} for 1 TeV WIMP mass.

2.2.1 Operating Principles of Dual-Phase TPCs

Dual-phase TPCs exploit the gas phase to amplify the ionisation signal in the form of scintillation signal. Extraction of electrons from the liquid phase into the gas phase can be understood as a potential barrier problem, since the potential energy of the (quasi-free) electrons is lower in the condensed phase than in the gas phase. The difference is 0.67 eV in LXe and 0.2 eV in LAr. This extraction process is promoted by application of an external field to the liquid-gas interface which helps in various ways, one one hand by accelerating the electrons towards the interface so that those with sufficient kinetic energy can jump the barrier and at the same time by reducing the value of the potential barrier itself [10].

Figure 2.3 illustrates how this is used in an actual TPC. Upon a scattering, prompt scintillation, S1, is generated and collected by the PMT arrays. A downward-pointing electric field is applied between the gate grid and the cathode grid at the bottom of the chamber, causing the ionisation electrons to drift to the top. Another, much stronger electric field is applied between the gate grid and the anode grid, with the gas-liquid

interface in the middle. This field extracts the electrons to the gaseous phase, which will generate the delayed signal S2 via electroluminescence.

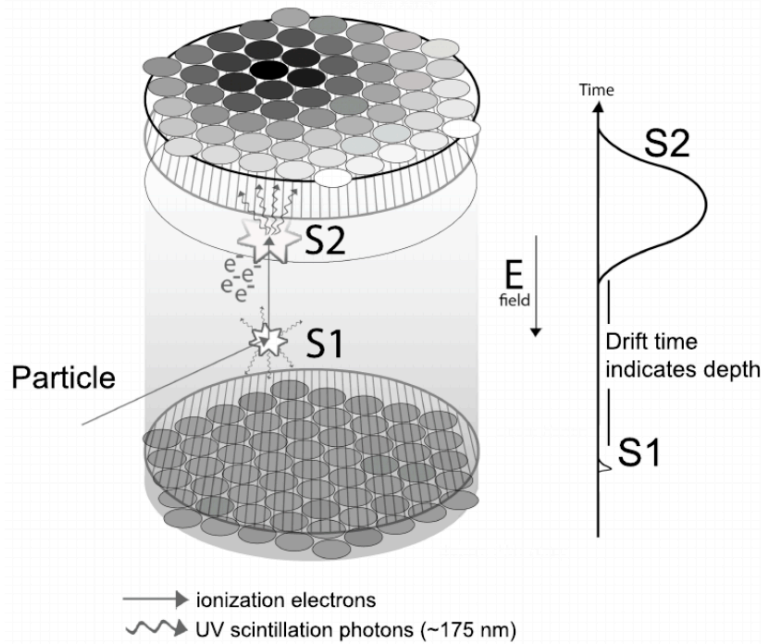


Figure 2.3: Simplified view of an event in a dual-phase TPC from [19]

Due to the amplification in the gas phase, S2 will be of much larger magnitude than S1. The analysis of the relative magnitude and timing of these two signals is a powerful discrimination tool since the ratio of S1 to S2 is different for electronic and nuclear recoils [55]. In a NR a bigger fraction of energy is lost as heat, the track length is smaller and thus a higher local charge density makes recombination more likely. For this reason, ERs result in a larger S2 signal. Additionally, because the fraction of triple state excitations is bigger for an ER, average decay times are slower and the S2 signal is more delayed for an ER than for a NR [10].

Another advantage of dual-phase detection, is that the TPC allows for 3D reconstruction of the position of the interaction. The distribution of S2 signal in the PMTs gives the (x,y) position while the drift time, delay between the S1 and S2, gives the x position of the event [19]. This is what makes fiducialisation of the active volume possible along with the self-shielding properties of LXe, resulting in unprecedented background reduction efficiency. Due to its high atomic number (54) and density ($\sim 2.85 \text{ g/cm}^3$), most beta and γ rays are absorbed by the outer regions of the active mass, reducing the background greatly in the inner regions [10].

In dark matter and CE ν NS searches, interaction rates are small and great care is needed to avoid being dominated by backgrounds. In the past, single-phase (liquid) detectors have been used for dark matter search, such as the DEAP collaboration's detector [56]. However, the absence of an S2 signal leads to a lack of precise fiducialisation of the detecting medium. Most backgrounds for these experiments originate from the surfaces of the detector, namely the detector walls, grid and PMTs. Thus, defining a fiducial volume is very important for experiments like dark matter searches, which have very small rates of interaction [38]. Dual-phase TPC chambers are ideal in these cases [10, 38].

2.2.2 Background Considerations

A huge challenge of both dark matter searches and the detection of $CE\nu NS$ with dual-phase TPCs is to minimise backgrounds so that the NR spectrum of dark matter particle interactions or the coherent elastic scattering of neutrinos might be observed. Backgrounds mainly consist of electronic recoils (ER) from γ rays and beta radiation and nuclear recoils (NR) from neutrons. The most challenging background comes from neutron NR interactions, which mimic the expected signal from a WIMP.

Sources of backgrounds can be either internal or external to the detector. Internal sources of backgrounds refer to natural radiation from the materials used in the detector or radioactive isotopes of the target medium or radioactive contaminants. For example, atmospheric sourced argon contains significant amounts of ^{39}Ar with 1 Bq/kg [10]. Underground sourced LAr is known to be a pure alternative in regards to this isotope and is currently being used in active detectors [38]. In the case of xenon, most of the naturally found isotopes are stable, with the exception of ^{124}Xe and ^{136}Xe which, nonetheless, have very high half lives and are not a matter of concern [5, 6]. Contamination from ^{85}Kr . This contaminant can be removed, for example via adsorption-based chromatography, to great effect. The LUX-ZEPLIN collaboration's Kr removal system was designed to achieve a Kr content as low as 0.015 ppt [57]. The PTFE itself can be a source of backgrounds. Contamination by plate-out during manufacture is possible (Polonium and Lead) [1]. Additionally, Radon (^{210}Rn) emanated by detector components is a great source of backgrounds (from Radon decay chain products like ^{214}Pb and ^{214}Bi) [1]. The ^{214}Pb source is especially problematic since it has a significant probability of naked beta decay emission, so there is no accompanying γ ray for vetoing the interaction.

External sources of backgrounds include γ rays from the rock walls around the detectors, spallation neutrons from interactions with cosmic ray muons, and cosmogenic activation of materials from those muon induced neutrons [1]. For example, xenon activation can occur, giving origin to unstable isotopes like ^{127}Xe , ^{129m}Xe , ^{131m}Xe , ^{133}Xe , which can become problematic for the searches in question [55].

Background mitigation consists of three main components: material assay and background reduction, detector shielding and background rejection and discrimination.

Background reduction efforts include materials screening and assay to select radio-pure materials for the detector, cleanliness protocols to avoid activation and contamination of materials, and the removal of radioactive contaminants from the target medium, such as the krypton removal from xenon mentioned above.

Detector shielding includes fiducialization of the volume as already discussed, as well as moving the detector underground and using water as shield. Generally, dark matter detectors are installed deep underground where they are shielded from cosmic muons, with the muon flux being reduced exponentially with depth [58]. The LZ detector, for example, is installed in the Stanford Underground Research Lab (SURF), 1478 m underground in the old Homestake Mine near Lead, South Dakota, USA. Additionally, the detectors are immersed in a water tank (figure 2.4) that shields the detector from γ rays and neutrons from the rock walls of the laboratory, either of natural or cosmogenic (from cosmic muon capture) origin [58, 1].

The last resort against backgrounds is discrimination and rejection. The water tank that serves as shielding can also be instrumented with PMTs to detect the Cherenkov radiation from incoming muons so that coincident signals in the detector can be correctly tagged as having originated from muon backgrounds [55]. In the case of the LZ detector,

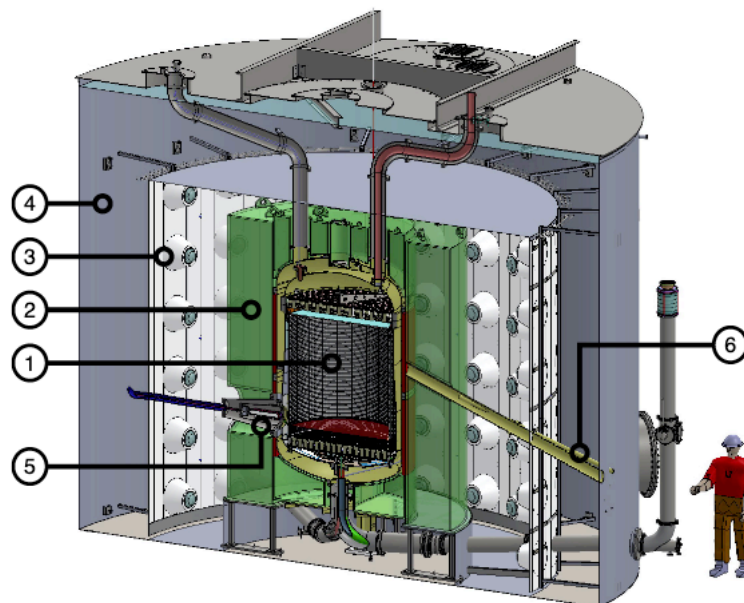


Figure 2.4: Renderig of the LZ detector from [1]. (1) LXe TPC; (2) GdLs Outer detector; (3) Outer detector PMTs; (4) Water which proved shielding and Cherenkov radiation based veto; (5) Cathode high voltage connection; (6) pipe for deployment of neutron calibration sources.

a “skin” with 2 tonnes of LXe surrounding the detector vessel, instrumented with PMTs, is used as scintillation only veto for γ rays. Additionally, an acrylic container with gadolinium loaded liquid scintillator is used for neutron tagging, given the high cross section of neutron capture in ^{155}Gd and ^{157}Gd [1]. Figure 2.4 is a schematic representation of these systems in the LZ detector. Pulse shape analysis and event topology aid in tagging and vetoing the backgrounds. Most backgrounds, apart from neutrons, result in electronic recoils. As discussed above, due to the differences in energy deposition, the ratio of S2 and S1 signals is an efficient tool to discriminate most of these backgrounds [55].

2.3 PTFE Reflectance Measurements for LNG Detectors and Diffuse Reflectance Modelling

Understanding scintillation light collection in the detectors is of utmost importance, and subsequently, understanding the reflectivity of the detector materials is critical. As we have seen, most LNG detectors described employ PTFE as a reflector, normally covering most of the total surface in contact with the target medium. Its high diffuse reflectivity for a broad range of wavelengths as well as its high electric insulation and relatively low outgassing make it one of the best materials for this purpose. Additionally, it is chemically inert, has excellent dielectric properties over a wide range of temperatures [59] and a high

melting point at 600 k, although decomposition becomes non-negligible from ~ 500 k on [60]. It is possible to manufacture it in appreciable quantities as a highly radio-pure material (U and Th contamination on the order of ppb) [61, 62]. Finally, it displays relatively slow outgassing, which is important to avoid contaminating the noble liquid [15]. This is important since optical properties, like the refractive index and absorption length, as well as light yield in the noble liquid, depend on the purity of the noble liquid [10].

For wavelengths in the range 350–1800 nm, PTFE displays a very high reflectivity, around 99% (figure 2.5) [14]. For the xenon scintillation wavelength in the vacuum ultraviolet (VUV), 175 nm, it has been estimated between 50% and 80% using a total integrating sphere (TIS) [17]. A more recent study, with different samples of PTFE obtained from different manufacturing processes (extruded, expanded, skived and pressed) reported reflectivity values from 47 to 66% in the VUV (normal incidence). A goniometer, or angle-resolved system (ARS) was used to measure the reflectance of the samples for varying viewing angle and angle of incidence. This system allows to rotate the sample being studied, and in doing so varies the incident and viewing angles. It was observed, besides diffuse reflection, an additional specular lobe with increasing relevance for lower wavelengths [18]. Both these experiments were conducted in a controlled atmosphere using noble gases, argon in the case of [18], otherwise the oxygen molecules in the air would absorb most of light below 200 nm. In the case of argon, most of the scintillation light, with the peak wavelength of 128 nm, is absorbed by the PTFE, being below the dielectric's absorption peak at 161 nm, hence the use of tetraphenyl butadiene (TPB) for wavelength shifting [21].

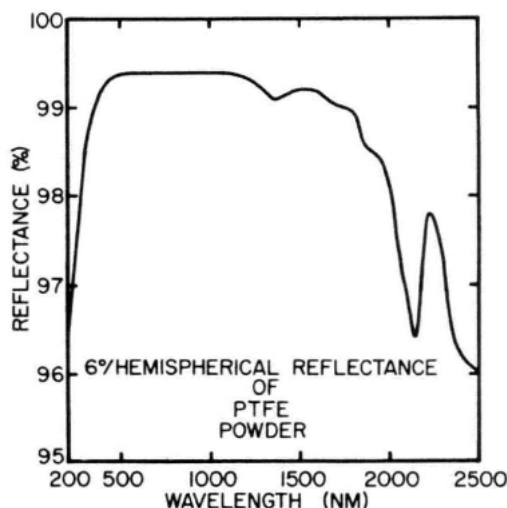


Figure 2.5: Hemispherical reflectance factor of PTFE measured with a total integrating sphere and a collimated source with incident angle of 6° with respect to the sample surface normal to make sure specular reflectance is included in the measurement. From [14]

When one moves away from a gaseous interface to a liquid interface, as is of most interest to LNG detectors, the PTFE reflection of VUV light is significantly enhanced. In-situ measurements are generally made with the LNG detectors. In the science run III of the LUX detector, the analysis identified the PTFE reflectivity, taken to be as purely Lambertian in the simulations, and the xenon absorption length as the two free parameters with the greatest impact on light collection. Multiple simulations with varying

values for the two free parameters were compared with the observed run III data, and a reduced χ^2 was obtained (figure 2.6). It can be readily seen from the map that the two parameters display degeneracy, with both having similar effects on the reduction of light collection. Remarkably, the PTFE reflectivity must be at least 96% to be compatible with the experimental results, even assuming infinite absorption length [13].

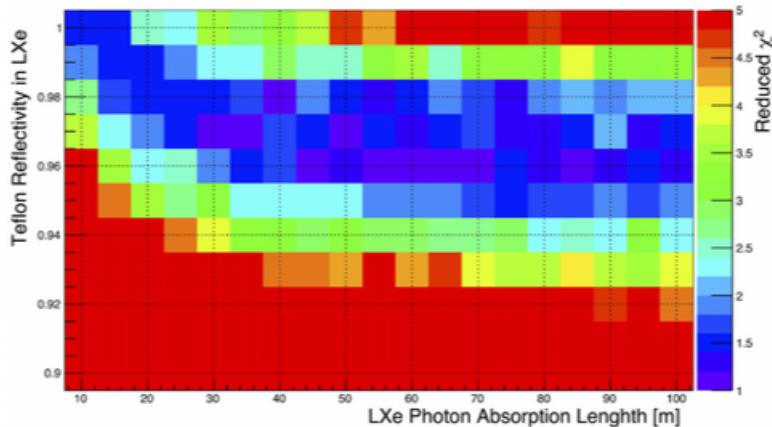


Figure 2.6: From the LUX III run analysis [13], χ^2 map for PTFE reflectivity and LXe absorption length, the two free parameters with greatest impact on light collection.

During the R&D phase of the LZ project, some PTFE optical studies were performed at SLAC National Accelerator Laboratory using the System Test platform - a prototype set-up to validate technologies for the LZ detector [19]. Fig 2.7 shows a cross section of the TPC used for the system test. The TPC design follows for the most part that of the LZ chamber, with a structure of PTFE rings stacked upon each other with steel field shaping rings in between.

This study addressed the degeneracy between LXe absorption length and the PTFE reflectivity on the basis of the detector geometry. The system test platform has a cylindrical geometry with an aspect ratio (length/diameter) of 3.57. The LUX (and also LZ) detectors also have a cylindrical geometry with an aspect ratio (length/diameter) of 1. It was shown that the asymmetrical aspect ratio facilitates discerning the reflectivity effect on light collection from the absorption length effect according to the different event topology [19].

The measurement of the PTFE reflectivity itself was made by matching the measured light yield against the simulation of photon propagation in the test platform for a range of optical parameters: the LXe absorption length, Rayleigh scattering in the LXe and also four reflecting interfaces: PTFE - LXe, PTFE - gaseous Xe, the reflectivity of the PEEK spacers in the extraction region and the reflectivity of the top cone made of polyimide film (Kapton®) in the gaseous Xe zone. The simulations considered solely Lambertian diffuse reflection. The effect of Rayleigh scattering and the LXe absorption length in the estimation of the PTFE reflectance were observed to be degenerate, and so a fixed value of 35 cm from the literature was set for Rayleigh scattering and the absorption length was left as a free parameter. A final best fit value of 95% confidence level reflectivity value was found for PTFE-LXe interface: $99.0^{+0.4}_{-0.2}\%$. A summary of the best fit values for all parameters is presented in table 2.2.

Besides in-situ measurements, dedicated experiments have also been performed to study the reflectance of PTFE in LXe. These tend to give better constrained results

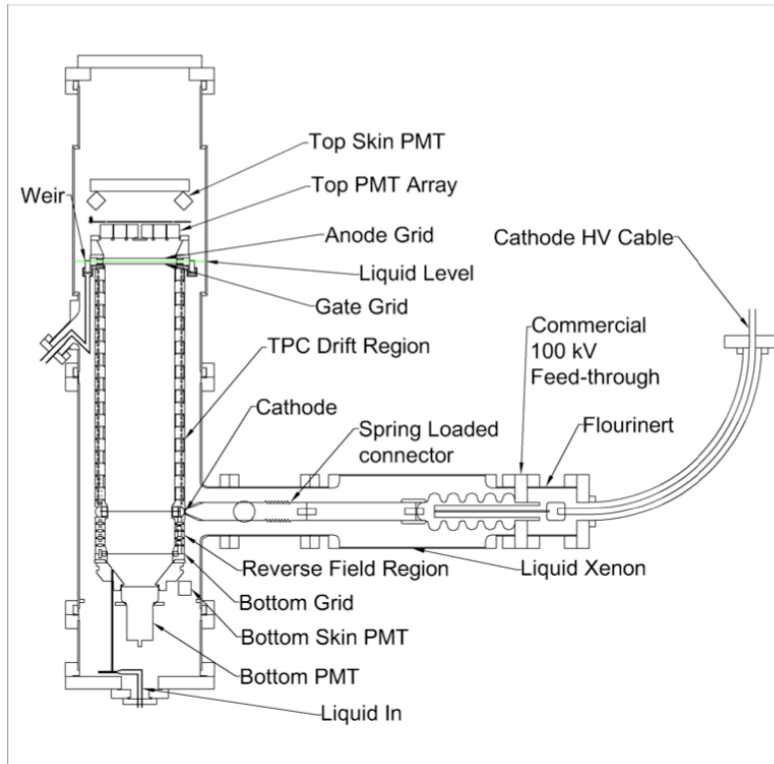


Figure 2.7: Cross section diagram of the test platform TPC and the cathode high-voltage feed-through from [19]. Detail of the ring based PTFE structure can be seen. The liquid xenon skin around the TPC is shown too.

given the simpler set-ups. In order to obtain a result, it is necessary to fit the measured light collected against a range of parameters. In a full detector there are generally more parameters to consider, like other reflecting surfaces (high voltage grids, etc) [13, 19] and the geometry cannot be changed to constrain absorption length and Rayleigh scattering the way it is sometimes done in dedicated experiments [12].

A dedicated experiment, performed at LIP Coimbra employing LXe and a ^{241}Am alpha source (5.6 MeV) to induce scintillation, reported an absolute reflection value of PTFE for 178 nm of $\geq 97\%$ [12]. The active region was enclosed in 1 cm PTFE thick walls. The top wall was movable allowing to change the geometry of the active volume changing the height of the chamber between 19 and 147 mm (figure 2.8). The PMT pulse height spectrum was acquired for each position of the top wall and the energy deposition from the alpha particles was estimated from a Gaussian fit.

Light collection for the varying geometry was modelled by Monte Carlo simulations performed in the ANTS2 software package [30]. The Rayleigh scattering was fixed at 29 cm and the absorption length was left as a free parameter along with the PTFE diffuse albedo. For the LXe-PTFE optical interface, two models were used. One model considered only diffuse Lambertian reflectance in the bulk of the material, and another considered specular reflection at the LXe-PTFE interface and diffuse reflection of the photons refracted into the PTFE. The relative variation of the light collected with changing height was compared with that of the simulations. The diffuse only model was seen to underestimate the collected light, indicating that a significant specular component was present. Given the limitations of the set-up in constraining the absorption length in LXe

Table 2.2: Best fit values of the optical parameters in the LZ System Test optical simulations [19]

Parameter	Literature	Best fit
PTFE-Gaseous Xe	75 % $^{+10}_{-5}$ [13]	70 %
Kapton®	Unknown	0 %
PEEK	67 % [23]	40 %
PTFE-LXe	≥ 97.5 % [12]	99.0 %
LXe Rayleigh Scattering	35 \pm 2 cm [63]	35 cm
LXe Absorption Length	30 $^{+40}_{-20}$ m [13]*	330 m

* Best-fit value found in the optical simulations LUXsim of the LUX dark matter experiment [13].

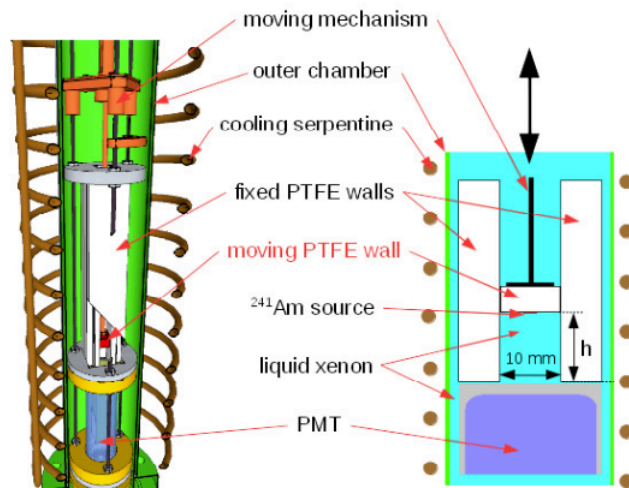


Figure 2.8: 3D view (left) and schematic illustration (right) of the chamber for measuring the PTFE reflectance in LXe. The ^{241}Am source is shown placed below the top wall, and the PMT positioned at the bottom. From [12].

past a certain point, it was only possible to obtain a lower bound for the reflectance of the PTFE in LXe, $\geq 97\%$.

Another experiment at the Lawrence and Berkley National laboratory used an angle-resolution system to measure the reflectance of various PTFE samples in LXe [64]. The ARS changed the incident angle by rotating the sample, while the PMT was rotated within the plane of incidence (the plane made by the surface normal and the incident direction). The model developed in [65] by Silva et al., was used to extrapolate the full hemispherical reflectance for each incident angle from the data obtained for the multiple viewing angle positions. This model describes reflection as composed of three components. One is a diffuse lobe, from internal scattering in the bulk of the material. The remaining two are specular components from the Fresnel reflection at a surface of random roughness: a broad specular lobe and a narrow specular spike, [65]. Figure 2.9 shows the extrapolated

hemispherical reflectance for each component over the range of incident angles for one of the tested samples in both air and LXe interfaces.

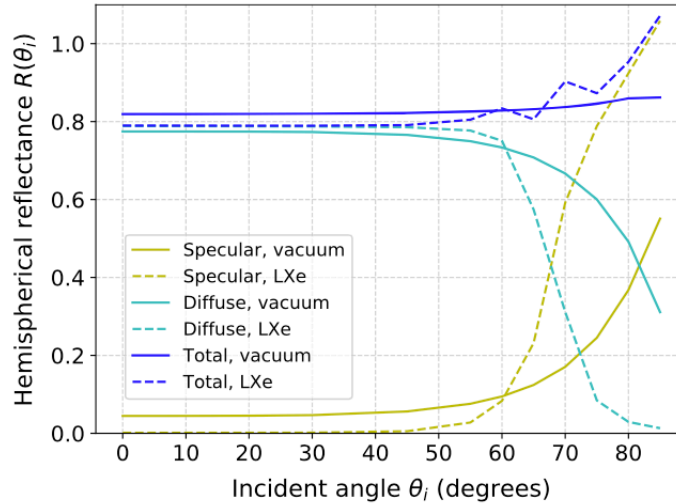


Figure 2.9: Hemispherical reflectance versus incident angle [64]

It clearly shows deviation from the ideal Lambertian behaviour, which neglects the effect of Fresnel reflection due to the change in refractive index at the interface. Also, this result is in tension with the measurements done at LIP in [12], having obtained a lower value for the total reflectance of PTFE in LXe. Some of the possible reasons given in [64] for this tension are differences in light source, fluorescence effects and surface degradation [64]. However, the most relevant reason mentioned is that angle-resolved measurements tend to underestimate the total reflectance measurement [18]. Finally, direct comparison between the two different geometries is complicated, due to the dependence of reflection on the incident angle [64].

Table 2.3 summarises multiple results of PTFE reflection to xenon scintillation in both liquid and gaseous interfaces from multiple experiments for comparison.

While an ideally diffuse Lambertian surface will appear equally bright from all viewing directions, real materials will always have some fraction of specular reflectance due to the change in refractive indexes at the interface. It can be readily seen from the last rows of table 2.3 that reflectivity varies with the incident angle. Although it is not shown in the table, the increase for $\theta_i = 65^\circ$ is not always accompanied by an increase in the diffuse reflectance, but by an increase in the specular component. Also, there is a significant difference depending on the machining method, which impacts surface roughness [18]. This is in accord with much older research from 1995, where reflection from rough surface dielectrics was studied and reflection was seen to increase as the viewing angle approached the incident angle, in a clear deviation from Lambertian behaviour. [24]. Additionally, Voss and Zhang studied the reflectance of a Spectralon® plate both in air and submerged in water. Also, in deviation from Lambertian behaviour, a narrowing of the angular profile of the Spectralon® reflectance factor was observed [33].

Despite the results mentioned above, MC simulations of LNG detectors almost always model PTFE reflection as a purely Lambertian surface. Such is the true for the cases

Table 2.3: Reflection values for various PTFE samples and interfaces.

Interface	Material	<i>Reflection</i> * (%)	Measured at..
PTFE-LXe	LUX PTFE	97_{-2}^{+3}	LUX in-situ [13]
PTFE-LXe	LUX PTFE sample	≥ 97.5	LIP Coimbra [12]
PTFE-LXe	807NX sample	≥ 95.5	LIP Coimbra [12]
PTFE-LXe	NXT85 sample	≥ 97.3	LIP Coimbra [12]
PTFE-LXe	LUX PTFE sample	$99.3_{-0.2}^{+0.4}$	SLAC [19]
PTFE-gas Xe	LUX PTFE	75_{-5}^{+10}	LUX in-situ [13]
PTFE-gas Xe	Molded	$49 \pm 2, \theta_i = 0^\circ$	LIP Coimbra [18]
	(unpolished)	$53 \pm 2, \theta_i = 65^\circ$	
PTFE-gas Xe	Molded (polished)	$74 \pm 0.06, \theta_i = 0^\circ$	LIP Coimbra [18]
		$81 \pm 8, \theta_i = 65^\circ$	
PTFE-gas Xe	Extruded	$69 \pm 6, \theta_i = 0^\circ$	LIP Coimbra [18]
		$73 \pm 4, \theta_i = 65^\circ$	
PTFE-gas Xe	Skived	$55 \pm 2, \theta_i = 0^\circ$	LIP Coimbra [18]
		$59 \pm 2, \theta_i = 65^\circ$	

* Bi-hemispherical reflectance is shown unless the angle of incidence is included;

mentioned above as well as the simulations of DarkSide-50. Analysis with the DarkSide-50 detectors were used to fine tune the optical parameters of its successor, DarkSide-20k. The reflectivity of PTFE was modelled as a purely Lambertian albedo of 98% for the wavelength shifted scintillation (400–480 nm) and 7.5% for the VUV scintillation. [21].

Given these considerations and the dramatic change in reflectivity of PTFE while immersed in liquid [12, 13], we believe it to be of interest to study the effect of the liquid interface in diffuse reflection besides the trivial change in the refractive index it adds, as pointed out by Silva et al. [18]. This would not only improve simulations which are crucial for data analysis, but also provide better informed assumptions or extrapolations from liquid to gaseous interfaces with dielectrics and vice-versa when needed. It is also important to point out, that the set-up developed in this work, making use of a total integrating sphere, is more adequate than an angle-resolved system to measure the total reflectance of samples in a geometry-independent way [28].

Chapter 3

Optics, Radiometry and Reflectance

The focus of this work is to study diffuse reflectance in a liquid interface. Reflectance in some dielectrics like PTFE is very different from the mirror-like reflection of metals and other materials. In diffuser materials with high reflectivity, a big portion of reflectance is from a diffuse component. This component originates from light light refracted to the bulk of the diffuser which is internally scattered due to inhomogeneities in the refractive index in the bulk of the material and, eventually, is refracted back out to the original medium. Thus, diffuse reflectance is a function not only of the scattering and absorbing properties of the diffuser, but also of the incoming and outgoing optical interfaces.

Another critical component in the reflectance is surface roughness. Surface roughness is a characteristic of the microscopic shape of the surface, generally quantified by deviations of the normal vector of a real surface from its “ideal”, smooth, form. The most popular model that includes this component in the surface reflectance originates from the work of Torrance and Sparrow. In it, reflection in rough surfaces was modelled as a collection of randomly oriented smooth micro-facets for which Fresnel theory individually applies [66].

For our own study of diffuse reflectance of PTFE in a liquid interface, an experimental set-up using a total integrating sphere was developed (described in chapter 4). In this chapter we lay out the theoretical groundwork in optics relevant to understand the underlying mechanics of diffuse reflectance.

This chapter starts with a review of the basic Snell-Descartes laws and the Fresnel equations in the context of plane waves. Next, a discussion about reflection in radiometry follows, laying out concepts, notation and geometric considerations crucial for understanding the remainder of this work.

After that, diffuse reflectance is discussed in more detail, in light of the Lambert law and also Chandrasekhar’s results in radiative transfer with application to the internal scattering of diffusers. Next, important aspects of reflection from rough surfaces are discussed.

The chapter closes with an overview of the Wolff and Oren-Nayar model [31], which takes the aspects discussed in the previous sections to present a significantly complete and rigorous reflection model. Some relevant aspects of its implementation by Silva et al. in [16] are also discussed. This model, implemented in the ANTS2 simulation software package, was also used to simulate the experimental data of PTFE reflectance in LXe by Neves et al. in [12].

3.1 Reflection and Refraction of Plane Waves

3.1.1 Snell-Descartes Refraction and Reflection laws

When an electromagnetic plane wave crosses a boundary between two homogeneous media with different optical properties, it is split into two separate parts (fig 3.1): a reflected wave, back towards the first medium (with refractive index n_1), and a transmitted wave, across the second medium (with refractive index n_2). This happens according to the well known Snell-Descartes laws:

$$\theta_r = \theta_i, \quad (3.1)$$

$$n_1 \sin \theta_i = n_2 \sin \theta_t. \quad (3.2)$$

The angles θ_i , θ_r and θ_t are defined in relation to the normal vector of the reflecting surface. At the time of their derivation the theory of electromagnetic waves did not exist yet. John Clerk Maxwell first conjectured that light waves were electromagnetic waves, which was later proved by Heinrich Hertz in 1888. The Snell-Descartes laws can be easily explained through Pierre Fermat's Principle of Least Time (1662) and the use of trigonometry [67].

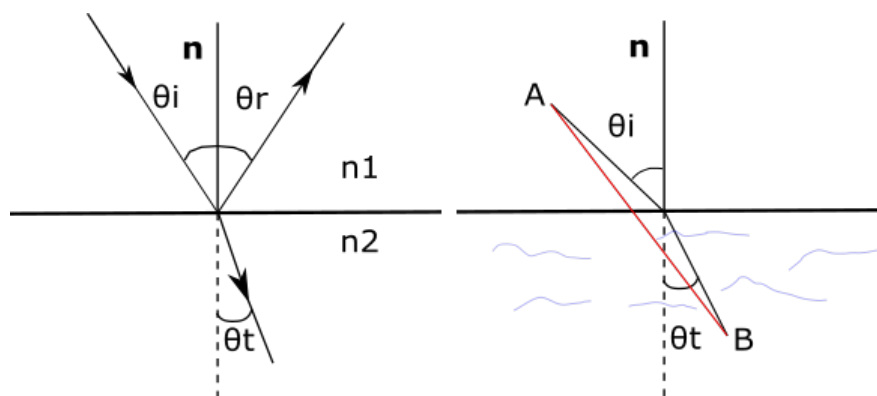


Figure 3.1: Left: separation of an incident plane wave into a transmitted and a reflected wave according to Snell-Descartes laws. Right: illustration of Fermat's principle of least time applied to the law of refraction.

Simply put, the Principle of Least Time dictates that out of all possibilities, light always takes that which requires the shortest time to cross. In the case of refraction, at a first glance, the quickest path from A to B (fig. 3.1) would be in a straight line. A simple example will prove this wrong. Imagine someone is screaming for help in the sea (point B), while you are laying on sand (point A). The quickest way to the person in need might seem to be in a straight line. However, as you most probably are substantially faster on land — it is then intelligent to run a longer way on land in order to swim less. There is such a path, with such portions of land and sea that minimises the time to get to the person in need, depending on your speed in land and sea and said path is given exactly by Snell's law (eq. 3.2). The same thing happens with light when crossing from air to water, or from one medium to another with different refractive indexes.

Getting back to a plane wave falling on a boundary between two homogeneous media; there is more to it than just the geometry of the light ray propagating. From the

boundary conditions one can derive not only the reflection and refraction laws, but also the amplitudes for the reflected and transmitted waves. Consider a propagating plane wave whose direction is given by unitary vector \vec{s}^i . At the boundary plane $z=0$ between media 1 and 2, for a point $r=(x,y,0)$ and considering the reflected (\vec{s}^r), and transmitted (\vec{s}^t) unitary vectors, one can write [68]:

$$\frac{\vec{r} \cdot \vec{s}^i}{v_1} = \frac{\vec{r} \cdot \vec{s}^r}{v_2} = \frac{\vec{r} \cdot \vec{s}^t}{v_2}, \quad (3.3)$$

where v_1 and v_2 are the speed of propagation of the plane wave in media 1 and 2 respectively. Since 3.3 must be true all for any x and y , then:

$$\frac{s_x^i}{v_1} = \frac{s_x^r}{v_1} = \frac{s_x^t}{v_2} \qquad \frac{s_y^i}{v_1} = \frac{s_y^r}{v_1} = \frac{s_y^t}{v_2}. \quad (3.4)$$

We will now work on the *plane of incidence*, which is the plane defined by \vec{s}^i and the normal to the boundary plane. Taking the plane of incidence as the plane XOZ (remember the boundary plane is $z = 0$) and considering θ_i , θ_r and θ_t the angles which the respective direction vectors make with the z axis (figure 3.2) we get:

$$\begin{aligned} s_x^i &= \sin \theta_i, & s_y^i &= 0, & s_z^i &= \cos \theta_i \\ s_x^r &= \sin \theta_r, & s_y^r &= 0, & s_z^r &= \cos \theta_r \\ s_x^t &= \sin \theta_t, & s_y^t &= 0, & s_z^t &= \cos \theta_t, \end{aligned} \quad (3.5)$$

substituting 3.5 in 3.4 for the x coordinates, gives:

$$\frac{\sin \theta_i}{v_1} = \frac{\sin \theta_r}{v_1} = \frac{\sin \theta_t}{v_2}. \quad (3.6)$$

From 3.6 we can derive both reflection and refraction's laws. It is clear right away that $\sin \theta_i = \sin \theta_r$, also, acknowledging that for waves propagated in the opposite direction to incidence the z component is negative, we see that $\cos \theta_r = -\cos \theta_i$ and hence:

$$\theta_r = \pi - \theta_i. \quad (3.7)$$

We are back to Snell-Descartes reflection law, along with the knowledge that \vec{s}^r sits on the plane of incidence.

From the definition of the absolute refractive index $n_i = c/v_i$ (where c is the speed of light) it follows that $\frac{v_1}{v_2} = \frac{n_2}{n_1}$. From this result and equation 3.6 we get the Snell's refraction law, along with the knowledge that \vec{s}^t sits on the plane of incidence:

$$\frac{\sin \theta_i}{\sin \theta_t} = \frac{n_2}{n_1}. \quad (3.8)$$

Close inspection of this relation shows that when the second medium is optically denser than the first, $n_2 > n_1$, the equation can be solved for all real angles. However, if the inverse is true, $n_1 > n_2$, the equation can only be solved for real angles as long as $\sin \theta_i \leq \frac{n_2}{n_1}$. For larger angles no refraction happens and we have the phenomenon of total internal reflection.

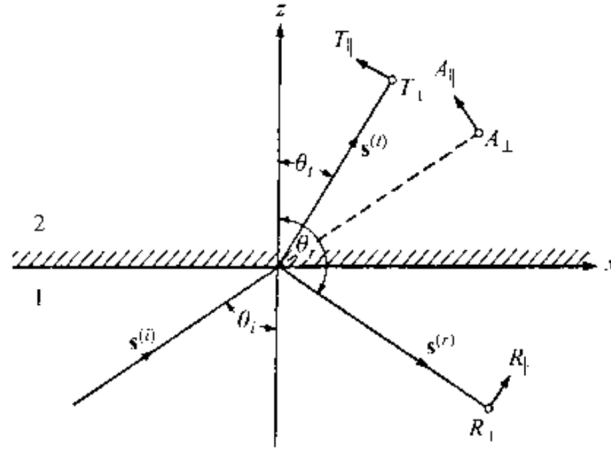


Figure 3.2: Reflection and refraction on the plane of incidence (XOZ). Boundary plane $z = 0$. From [68].

3.1.2 Fresnel Equations

Let us assume that the two media are perfectly non conducting since we are primarily concerned with that type of materials in this work. Take the electric vector of the incoming, reflected and transmitted (plane) waves with A , R and T amplitudes respectively and write them in terms of two components, one parallel (\parallel subscript) and another perpendicular (\perp subscript) to the plane of incidence. For example for the incoming wave, the electric vector can be written as:

$$E_x^{(i)} = -A_{\parallel} \cos \theta_i e^{-i\tau_i}, \quad E_y^{(i)} = -A_{\perp} e^{-i\tau_i}, \quad E_z^{(i)} = A_{\parallel} \sin \theta_i e^{-i\tau_i}, \quad (3.9)$$

where the phase $\tau_i = \omega(t - \frac{x \sin \theta_i + z \cos \theta_i}{v_1})$. The magnetic vector, in the case of a plane wave is related to the electric vector by $H = \sqrt{\epsilon} \vec{s} \times E$, where ϵ is the dielectric constant. Thus, for the incoming wave, the magnetic vector components can be written as:

$$H_x^{(i)} = -A_{\perp} \cos \theta_i \sqrt{\epsilon_1} e^{-i\tau_i}, \quad H_y^{(i)} = -A_{\parallel} \sqrt{\epsilon_1} e^{-i\tau_i}, \quad H_z^{(i)} = -A_{\perp} \sin \theta_i \sqrt{\epsilon_1} e^{-i\tau_i}, \quad (3.10)$$

similarly for the reflected (R, θ_r, ϵ_1) and transmitted waves (T, θ_t, ϵ_2). From Maxwell's equations, it can be seen that the components of the electric and magnetic vectors tangential to the interfacing surface must be continuous. If we apply this to the incident, reflected and transmitted waves, this implies, with the coordinate frame of the plane of incidence as shown in figure 3.2:

$$\begin{aligned} E_x^{(i)} + E_x^{(r)} &= E_x^{(t)}, & E_y^{(i)} + E_y^{(r)} &= E_y^{(t)} \\ H_x^{(i)} + H_x^{(r)} &= H_x^{(t)}, & H_y^{(i)} + H_y^{(r)} &= H_y^{(t)}. \end{aligned} \quad (3.11)$$

Solving these expressions in terms of the incident wave using the electric and magnetic vector expressions above, one arrives at the Fresnel equations for the reflected and transmitted waves:

$$\begin{aligned}
 T_{\parallel} &= \frac{2n_1 \cos \theta_i}{n_2 \cos \theta_i + n_1 \cos \theta_t} A_{\parallel} \\
 T_{\perp} &= \frac{2n_1 \cos \theta_i}{n_1 \cos \theta_i + n_2 \cos \theta_t} A_{\perp} \\
 R_{\parallel} &= \frac{n_2 \cos \theta_i - n_1 \cos \theta_t}{n_2 \cos \theta_i + n_1 \cos \theta_t} A_{\parallel} \\
 R_{\perp} &= \frac{n_1 \cos \theta_i - n_2 \cos \theta_t}{n_1 \cos \theta_i + n_2 \cos \theta_t} A_{\perp}.
 \end{aligned} \tag{3.12}$$

Or, alternatively, using the law of refraction, these can be written in a maybe more common form:

$$\begin{aligned}
 T_{\parallel} &= \frac{2 \sin \theta_t \cos \theta_i}{\sin (\theta_i + \theta_t) \cos (\theta_i - \theta_t)} A_{\parallel} \\
 T_{\perp} &= \frac{2 \sin \theta_t \cos \theta_i}{\sin (\theta_i + \theta_t)} A_{\perp} \\
 R_{\parallel} &= \frac{\tan (\theta_i - \theta_t)}{\tan (\theta_i + \theta_t)} A_{\parallel} \\
 R_{\perp} &= -\frac{\sin (\theta_i - \theta_t)}{\sin (\theta_i + \theta_t)} A_{\perp}.
 \end{aligned} \tag{3.13}$$

One thing to note is that the waves parallel to the plane of incidence and those perpendicular are independent of each other since there are no \perp terms for \parallel waves and vice-versa. Additionally, the weight of these \perp and \parallel terms, actually depends on the polarisation of the respective wave. If α_i is the angle the electric vector of the incident wave makes with the plane of incidence then (similarly for the reflected and transmitted waves):

$$A_{\parallel} = A \cos \alpha_i, \quad A_{\perp} = A \sin \alpha_i. \tag{3.14}$$

Now, consider the amount of energy in the waves per unit area of surface boundary (either incoming, or leaving, depending on the incident, reflected or transmitted wave). For the incident wave:

$$\begin{aligned}
 J^{(i)} &= S^{(i)} \cos \theta_i = \frac{cn_1}{4\pi} |A|^2 \cos \theta_i \\
 J^{(r)} &= S^{(r)} \cos \theta_i = \frac{cn_1}{4\pi} |R|^2 \cos \theta_i \\
 J^{(t)} &= S^{(t)} \cos \theta_t = \frac{cn_2}{4\pi} |T|^2 \cos \theta_t,
 \end{aligned} \tag{3.15}$$

where S is the Poynting vector, and similarly for the reflected $J^{(r)}$ and transmitted $J^{(t)}$ waves. One can now define the following ratios:

$$\mathcal{R} = \frac{J^{(r)}}{J^{(i)}} = \frac{|R|^2}{|A|^2}, \quad \mathcal{T} = \frac{J^{(t)}}{J^{(i)}} = \frac{n_2 \cos \theta_t |T|^2}{n_1 \cos \theta_i |A|^2} \quad (3.16)$$

These are the reflectivity and transmissivity respectively, which verify the law of conservation of energy $\mathcal{R} + \mathcal{T} = 1$. They also depend on the polarisation of the incident wave. In fact, introducing equation 3.14 for the incident energy, yields:

$$\begin{aligned} J_{\parallel}^{(i)} &= \frac{cn_1}{4\pi} |A_{\parallel}|^2 \cos \theta_i = J^{(i)} \cos \alpha_i^2 \\ J_{\perp}^{(i)} &= \frac{cn_1}{4\pi} |A_{\perp}|^2 \cos \theta_i = J^{(i)} \sin \alpha_i^2. \end{aligned} \quad (3.17)$$

And similar for the reflected and transmitted energy. Thus, the reflectivity and transmissivity can be written in terms of the \parallel and \perp components:

$$\begin{aligned} \mathcal{R} &= \mathcal{R}_{\parallel} \cos \alpha_i^2 + \mathcal{R}_{\perp} \sin \alpha_i^2 \\ \mathcal{T} &= \mathcal{T}_{\parallel} \cos \alpha_i^2 + \mathcal{T}_{\perp} \sin \alpha_i^2, \end{aligned} \quad (3.18)$$

where, using the Fresnel equations,

$$\begin{aligned} \mathcal{R}_{\parallel} &= \frac{J_{\parallel}^{(r)}}{J_{\parallel}^{(i)}} = \frac{|R_{\parallel}|^2}{|A_{\parallel}|^2} = \frac{\tan(\theta_i - \theta_t)^2}{\tan(\theta_i + \theta_t)^2}, \\ \mathcal{R}_{\perp} &= \frac{J_{\perp}^{(r)}}{J_{\perp}^{(i)}} = \frac{|R_{\perp}|^2}{|A_{\perp}|^2} = \frac{\sin(\theta_i - \theta_t)^2}{\sin(\theta_i + \theta_t)^2}, \\ \mathcal{T}_{\parallel} &= \frac{J_{\parallel}^{(t)}}{J_{\parallel}^{(i)}} = \frac{n_2 \cos \theta_t |T_{\parallel}|^2}{n_1 \cos \theta_i |A_{\parallel}|^2} = \frac{\sin 2\theta_i \sin 2\theta_t}{\sin(\theta_i + \theta_t)^2 \cos(\theta_i - \theta_t)^2}, \\ \mathcal{T}_{\perp} &= \frac{J_{\perp}^{(t)}}{J_{\perp}^{(i)}} = \frac{n_2 \cos \theta_t |T_{\perp}|^2}{n_1 \cos \theta_i |A_{\perp}|^2} = \frac{\sin 2\theta_i \sin 2\theta_t}{\sin(\theta_i + \theta_t)^2}. \end{aligned} \quad (3.19)$$

Note that the denominator in \mathcal{R}_{\parallel} goes to infinity when $\theta_i + \theta_t = \frac{\pi}{2}$ since $\tan \frac{\pi}{2} = \infty$. In that case $\mathcal{R}_{\parallel} = 0$ and the reflected and transmitted directions are perpendicular to each other. In fact, applying the law of refraction, and since $\sin \theta_t = \sin \frac{\pi}{2} - \theta_i = \cos \theta_i$ we arrive at the Brewster or polarising angle [68]:

$$\frac{\sin \theta_i}{\cos \theta_i} = \tan \theta_i = \frac{n_2}{n_1} \quad (3.20)$$

David Brewster first noted its significance in 1815, noting that if light is incident under this angle, it has no direction in the plane of incidence. Or in other words, light becomes completely polarised in the component perpendicular to the plane of incidence.

It should again be stressed that this discussion concerns dielectrics only, which is the relevant case for this thesis. In the case of conducting materials, an imaginary complex index of refraction has to be used, of which the real part is the refractive index, n , and the imaginary is generally referred to as the extinction coefficient, κ , which describes the

electromagnetic attenuation within the material. That is also the reason why diffuse reflection is only present in dielectrics, since in conducting material most of the transmitted energy into the material gets absorbed and reflection is mostly specular at the surface interface. The aspects of diffuse reflectance will be reviewed in the subsequent sections.

3.2 Reflection in Radiometry

Reflected light off a surface is generally divided in three distinct components (figure 3.3) [69]: (1) a specular spike; (2) a specular lobe; (3) a diffuse lobe. The first two result from specular reflection, which is governed by Fresnel theory and is the result of the change of the refractive index in the interface between two media. Assuming a non-smooth surface, the specular spike is the result of a coherent field reflected at the average boundary with surface normal \mathbf{n} and oriented in the specular reflection. The specular lobe is the product of an incoherent field fluctuating around the average boundary of surface, resulting from the reflection on multiple points with different heights and orientations. Thus, it results in a lobe oriented in the specular spike direction.

The diffuse lobe is the result of multiple scattering in the bulk of the second medium. Transmitted (refracted) light goes through multiple scatterings within the material due to inhomogeneities in the refractive index. A fraction of it is eventually refracted back into the first medium. Due to the random nature of the scattering in the bulk of the material it originates a broader lobe [20].

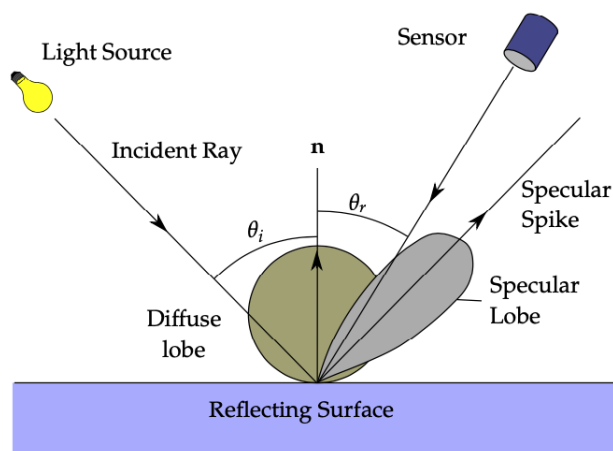


Figure 3.3: The three components of reflection. The diffuse component is centred around the normal while the specular components are centred around the specular direction (from [16]).

Before proceeding, it is important to write down some definitions from radiometry and agree on the nomenclature. Radiometry is concerned with the measurement of optical radiation, which roughly, corresponds to radiation from the ultraviolet up to the infrared. For this reason, it has a very useful body of knowledge and techniques relevant to the experimental work developed.

Radiant flux, Φ , is the amount of radiation in terms of energy, Q , or number of photons (for monochromatic light) per unit time incident upon (Φ_i), transmitted (Φ_t) or reflected (Φ_r) by an object or surface:

$$\Phi = \frac{dQ}{dt} \quad [\text{W}] \qquad \Phi = \frac{dNph}{dt} \quad [\text{Nphs}^{-1}] \quad (3.21)$$

Irradiance, E , is the radiant flux received by a surface per unit area, also known as radiant density:

$$E = \frac{d\Phi}{dA}. \quad (3.22)$$

Radiance, L , is the radiant flux received, reflected, transmitted or emitted by a surface per unit solid angle, $d\omega$, per unit projected area, dA :

$$L = \frac{d^2\Phi}{dA \cos \theta d\omega}, \quad (3.23)$$

where θ is the angle that the incident, reflected or transmitted direction makes with the surface normal. Figure 3.4 establishes the angles and solid angles relevant to radiometry and the measurement of reflectance. Note that both the incident and reflected directions concerning a particular point S , are inside a hemisphere with origin in S . Thus, the same detector, placed in different positions, will receive radiation from different amounts of surface areas. A detector at grazing angles will view a larger radiating surface area, while a detector closer to the normal to the surface will probe a smaller surface. In fact, the radiating area effectively probed by the detector is given by $A \cos \theta_r$ [18], as seen in figure 3.4.

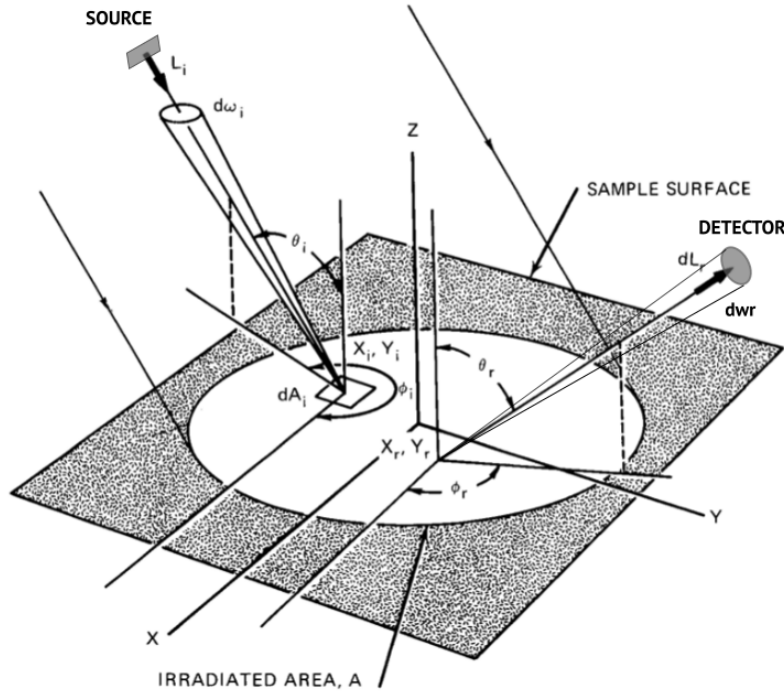


Figure 3.4: Definition of angles and solid angles relevant for radiometry in the general case where sub-surface scattering is also taken into account (adapted from [70]).

Consider now the radiant flux incident on a surface as depicted in figure 3.4 from direction (θ_i, ϕ_i) and solid angle $d\omega_i$. The portion of flux that strikes an element dA_i of

the radiated surface A_i is denoted $d\phi_i$. The reflected radiance dL_r in consideration will be proportional to that portion of flux:

$$dL_r = S \cdot d\phi_i \quad [\text{Wm}^{-2}\text{sr}^{-1}]. \quad (3.24)$$

The S function depends solely on the geometry of the incoming and reflected beams with the only assumption of geometric rays [70] and no physical reasoning behind how the interaction of light with matter that prompted such reflection is given:

$$S = S(\theta_i, \phi_i, x_i, y_i, \theta_r, \phi_r, x_r, y_r) \quad [\text{m}^{-2}\text{sr}^{-1}]. \quad (3.25)$$

This function is called the bidirectional scattering-surface reflectance distribution function (BSSRDF) and it effectively describes what one observes in a radiometric measurement of reflection.

In most practical applications, including those discussed in this thesis, the above model can be simplified. For example, it can be assumed that the surface element is uniformly irradiated and thus, the radiance is only dependent on the incident direction. The incident flux can then be written as [70, 18]:

$$d\Phi_i = L_i \cos \theta_i d\omega_i dA_i. \quad (3.26)$$

Furthermore, considering that the scattering properties of the sample are uniform and isotropic across the reference plane, the scattering function S will no longer depend on the actual coordinates (x_i, y_i) and (x_r, y_r) but solely on the distance r between them. Hence, the reflected radiance becomes:

$$dL_r = \varrho_r(\theta_i, \phi_i, \theta_r, \phi_r) \frac{d\Phi_i}{dA_i} \quad [\text{Wm}^{-2}\text{sr}^{-1}]. \quad (3.27)$$

The function ϱ_r is called the bidirectional reflectance-distribution function (BRDF) and it represents the amount of reflectance per steradian:

$$\varrho_r(\theta_i, \phi_i, \theta_r, \phi_r) = \int_{A_i} S(\theta_i, \phi_i, \theta_r, \phi_r, r) \cdot dA_i \quad [\text{sr}^{-1}]. \quad (3.28)$$

In other words, it is the ratio of the differential radiance and incident irradiance:

$$\varrho_r(\theta_i, \phi_i, \theta_r, \phi_r) = \frac{dL_r(\theta_i, \phi_i, \theta_r, \phi_r)}{L_i \cos \theta_i d\omega_i}. \quad (3.29)$$

Another useful simplification, comes from considering the detector is in a great enough distance to view the reflected surface element as a point-like source. In this case the radiance can be replaced by the intensity $I = \int L_r \cos \theta_r dA_r$. And so, a bidirectional reflected-radiance-distribution function (BRIDF) can be defined [18]:

$$\varrho_r^I(\theta_i, \phi_i, \theta_r, \phi_r) = \frac{dI_r(\theta_i, \phi_i, \theta_r, \phi_r)}{d\Phi_i(\theta_i, \phi_i)}. \quad (3.30)$$

If the surface element dA_i is small enough so that L_r can be considered constant over it, then BRDF and BRIDF are related by $\cos \theta_r$:

$$\varrho_r^I(\theta_i, \phi_i, \theta_r, \phi_r) = \varrho_r(\theta_i, \phi_i, \theta_r, \phi_r) \cos \theta_r. \quad (3.31)$$

At this point it is important to note that the conceptual bidirectional reflectance cannot be directly measured since it deals with infinitesimal angles and solid angles, and

in reality measurement apparatus deals with finite angles, however small they may be. One such quantity that can be in fact measured, is reflectance:

$$R(\omega_i, \omega_r, L_i) = \frac{d\Phi_r}{d\Phi_i} \quad [\text{dimensionless}], \quad (3.32)$$

which, can be written in terms of the BRDF by substituting in equations 3.22, 3.26 and 3.29 and defining the element of projected solid angle $d\Omega = \cos\theta d\omega$ for commodity:

$$R(\omega_i, \omega_r, L_i) = \frac{\int_{\omega_r} \int_{\omega_i} \varrho_r(\theta_i, \phi_i, \theta_r, \phi_r) L_i(\theta_i, \phi_i) d\Omega_i d\Omega_r}{\int_{\omega_i} L_i(\theta_i, \phi_i) d\Omega_i}. \quad (3.33)$$

Still, for this expression to be useful in a real application, it is necessary to consider the real beam geometry. In figure 3.5 some relevant incident and reflected beam geometries are pictured:

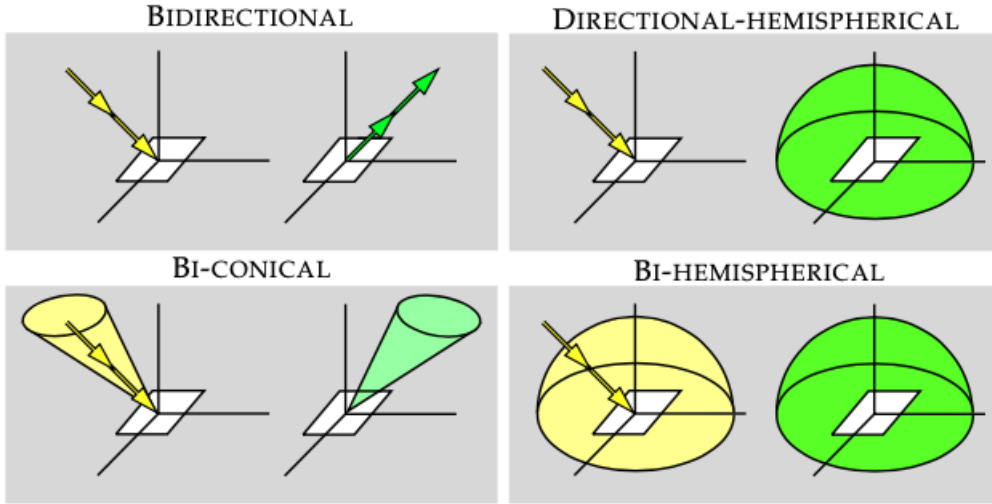


Figure 3.5: Example of common reflected and incident beam geometries (from [18]).

For example, by considering that L_i is uniform and isotropic within the solid angle of the incident beam, the constant value L_i comes out of both integrals and cancels out, resulting in the **biconical reflectance** [70]:

$$R(\omega_i, \omega_r) = \frac{1}{\Omega_i} \int_{\omega_r} \int_{\omega_i} \varrho_r(\theta_i, \phi_i, \theta_r, \phi_r) d\Omega_i d\Omega_r. \quad (3.34)$$

Or, if we take the hemispherical solid angle equal to 2π , to which will correspond the projected solid angle $\Omega = \int_{2\pi} \cos\theta d\omega = \pi$, the **bihemispherical reflectance** is obtained:

$$R(2\pi, 2\pi) = \frac{1}{\pi} \int_{2\pi} \int_{2\pi} \varrho_r(\theta_i, \phi_i, \theta_r, \phi_r) d\Omega_i d\Omega_r. \quad (3.35)$$

Finally, an interesting quantity is the reflectance factor, which is the ratio of the radiant flux actually reflected from a surface and the radiant flux reflected from an ideal perfectly diffuse surface, or in other words, a lossless Lambertian surface:

$$REFF = d\Phi_r / d\Phi_r^{ideal}. \quad (3.36)$$

In the case of Lambertian surface, L_r is constant for all values of (θ_r, ϕ_r) . Writing down the reflectance in such case, yields:

$$R(\omega_i, 2\pi) = \frac{d\Phi_r}{d\Phi_i} = \frac{L_r^{const} dA \int_{2\pi} d\Omega_r}{E_i dA} = \varrho_r(\theta_i, \phi_i, \theta_r, \phi_r)\pi. \quad (3.37)$$

Taking into account that it is a lossless surface, returns $\varrho_r^{ideal} = \frac{1}{\pi}$. Hence, the ideal radiant flux will be:

$$d\Phi_r^{ideal} = (dA/\pi) \int_{\omega_r} \int_{\omega_i} L_i(\theta_i, \phi_i) d\Omega_i d\Omega_r. \quad (3.38)$$

And so, for example the biconical reflectance factor is:

$$REFF(\omega_i, \omega_r) = \frac{\pi \int_{\omega_r} \int_{\omega_i} \varrho_r(\theta_i, \phi_i, \theta_r, \phi_r) d\Omega_i d\Omega_r}{\Omega_i \Omega_r}. \quad (3.39)$$

The reflectance factor was used by the authors Voss et al. in [33] when studying the reflectance of a spectralon plaque when submerged in water. It was found that even though in air there was very high agreement with a perfectly Lambertian surface, in water, there were clear deviations from it as there was a narrowing of the angular profile, with intensity focusing around the smaller angles. This can be explained if we think about what happens to the Fresnel coefficients in the dielectric-water interface, as we will see in the next section on diffuse reflectance.

3.3 Diffuse Reflectance

3.3.1 Lambertian Diffuse Law

Johann Heinrich Lambert noted that certain materials appeared equally bright independently of the viewing angle. His empirical description of diffuse reflection was published in 1760 in his work titled *Photometria*. There he established the Lambert law, for which the reflected radiated intensity distribution (BRIDF) has the following form [22]:

$$\varrho_r^I(\theta_r) = \frac{\rho_l}{\pi} \cos \theta_r \quad [\text{sr}^{-1}], \quad (3.40)$$

where ρ_l is the Lambertian albedo: the ratio of the flux diffusely reflected relative to the incident flux. The factor π is a normalising term so that the integral over the hemisphere is one. Referring back to the previous section about the reflectance factor, this term cancels out the integration of the projected solid angle over the full hemisphere.

In some dielectrics, light that gets transmitted suffers multiple subsurface scatterings in the bulk of the material (see figure 3.6) from discontinuities in the index of refraction. For example, PTFE is composed of both amorphous and crystalline regions, with the crystalline regions having a larger refractive index than the amorphous regions [71]. These differences in refractive index inside the PTFE are responsible for the scattering and absorption of light and are closely related to the value of the albedo [18]. A fraction of the scattered light eventually gets transmitted back into the first medium and when it does, its angle no longer has any relation to the original incident (or refracted) angle. Assuming it is a purely random process, the multiple scattering should be well described by Lambert's law (eq. 3.40). This is, however, a phenomenological law that describes an

ideal situation. In truth, there can be no purely Lambertian interface between two media with different refractive indexes because there will always be a fraction, however small, of specular reflection.

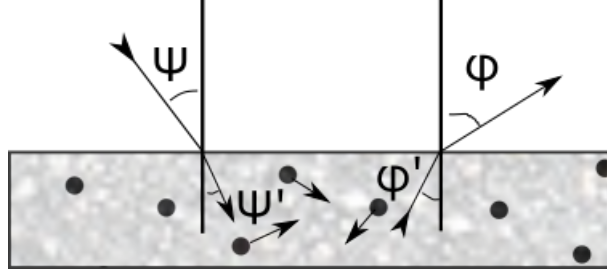


Figure 3.6: Geometric refraction of incident light and outgoing light after multiple sub-surface scatterings.

3.3.2 Geometry of Snell's Law and the Fresnel Coefficients

Let us start with assuming a smooth dielectric surface. It is useful to look at the geometry of Snell's law and the Fresnel coefficients at both entering the dielectric and leaving the dielectric interfaces [20]. This will make clear the effect of the surface on diffuse reflection.

Using the angles from figure 3.6 and assuming an azimuthal angle ϕ that does not change with crossing the interface and solid angles $d\omega = \sin \Psi d\Psi d\phi$ on medium 1 and similarly $d\omega'$ on medium 2, for the incident beam. Note that from Snell's law (with $n = n_2/n_1$):

$$\sin \Psi = n \sin \Psi' \leftrightarrow \cos \Psi d\Psi = n \cos \Psi' d\Psi' \leftrightarrow d\Psi' = \frac{\cos \Psi d\Psi}{n \cos \Psi'} \quad (3.41)$$

And so, using the previous relation and again Snell's law, the refracted solid angle $d\omega'$ becomes:

$$d\omega' = \sin \Psi' d\Psi' d\phi = \frac{\cos \Psi}{n^2 \cos \Psi'} d\omega \quad (3.42)$$

Or restating it in terms of the projected solid angle Ω :

$$\Omega = \cos \Psi' d\omega' = (1/n^2) \cos \Psi d\omega \quad (3.43)$$

From here we see that the solid angle gets compressed, assuming $n_2 > n_1$, by a factor of $\cos \Psi / (n^2 \cos \Psi')$ and the projected solid angle by a factor of $1/n^2$. The same thing happens in the outgoing interface, medium 2 to medium 1, except, assuming once again $n_2 > n_1$, the angles will open. When describing diffuse reflectance it is important to understand what happens to light going in to and out of the diffuser as that will impact internal scattering in the material.

The other surface effect is Fresnel reflection. Figure 3.7 shows transmittance to and from quartz and PTFE for the air and water case. It is this effect that might explain the difference between the reflectance in the gas and in the liquid

From figure 3.7 it can be seen that, on the one hand more light enters the dielectric in a water interface since the refractive indexes are better matched, especially more pronounced for larger angles. On the other, there is more light being refracted into the original medium, and substantially larger angles are allowed. Assuming the dielectric is

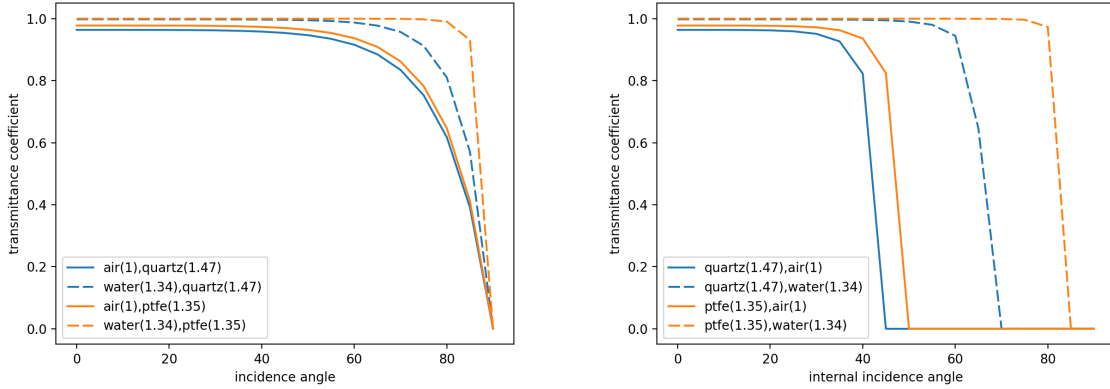


Figure 3.7: Fresnel transmittance coefficient into/from the dielectric according to Fresnel coefficients for wavelength of 380 nm. Legend shows the refractive indexes used.

semi-infinite, meaning light cannot leave anywhere except towards the first medium, if light escapes more easily, there will be less absorbed light inside the dielectric and hence more "reflected" light.

Having seen discussed the optical interfaces, we will now look at the details of sub-surface multiple scattering in the bulk of the diffuser.

3.3.3 Subsurface Scattering and Radiative Transfer Theory

Internal scattering of light inside a dielectric occurs due to inhomogeneities of the dielectric constant inside the bulk material. This effect can be likened to that of the scattering of incident light by gaseous molecules on stellar and planetary atmospheres, assuming isotropic scattering [20, 34].

Assuming a slablike geometry, or in other words, a medium where the optical properties only change as a function of depth (see the plane-parallel geometry in figure 3.8), the medium in question will scatter, absorb or emit radiation as a function of depth. The formalism used in radiative transfer theory is derived from Boltzman transport where photons are treated as particles diffusing through a medium. Mischenko has shown that this theory is valid for media with sparse discrete particles [72], making it suitable to study planetary atmospheres, neutron stars and even supernovae neutrinos [73]. Even though the formalism's validity for closely packed media, like powders or other dense materials hasn't been as rigorously established, there is some work to that regard, theoretical [74] and experimental to model the reflectance of Spectralon® [26]. While in the case of atmospheres radiation emission is of thermal nature and cannot be ignored, in the context of diffuse reflection, emission in the bulk of the dielectric will be neglected. Even though emission happens through fluorescence and phosphorescence, it is not necessary to include this in the treatment for diffuse reflection. In plane parallel geometry it is thus possible to write the following linear transport function for an inhomogeneous dielectric [75] (with the wavelength dependence suppressed for convenience):

$$\cos\theta \frac{dI(z, \cos\theta, \phi)}{dz} = -(\alpha_{sca} + \alpha_{abs})I(z, \cos\theta, \phi) + \frac{\alpha_{sca}}{4\pi} \int_0^{2\pi} d\phi' \int_{-1}^1 I(z, \cos\theta', \phi') \chi(\theta_s) \sin\theta' d\theta', \quad (3.44)$$

where α_{sca} and α_{abs} are the scattering and absorbing coefficients respectively. Introducing the vertical optical depth, $\tau = \int_z^{\text{inf}} \alpha_{sca}(z') + \alpha_{abs}(z') dz'$, and the change of variables $\mu = \cos \theta$ and $\mu' = \cos \theta'$, one can write more simply [26]:

$$\frac{dI(z, \cos \theta, \phi)}{d\tau} = -I(z, \mu, \phi) + \frac{\rho_s(\tau)}{4\pi} \int_0^{2\pi} d\phi' \int_{-1}^1 I(z, \mu', \phi') \chi(\theta_s) d\mu', \quad (3.45)$$

where $\rho_s(\tau)$ is the wavelength dependent (λ) single-scattering albedo, the probability that a photon is not absorbed between two consecutive scatterings inside the diffuser, defined as [75]:

$$\rho_s(\tau) = \frac{\alpha_{sca}(\lambda)}{\alpha_{sca}(\lambda) + \alpha_{abs}(\lambda)}. \quad (3.46)$$

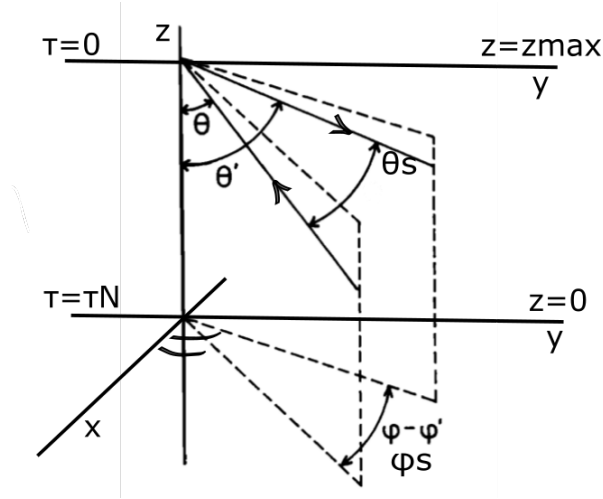


Figure 3.8: Parallel plane geometry and angle definitions in radiative transfer theory (adapted from [75]).

Likewise, the phase function $\chi(\theta_s)$, also known as scattering indicatrix function or scattering diagram, is a probability density function used to model an arbitrary anisotropic scattering medium. It depends on the scattering angle θ_s (figure 3.8). The phase function has the normalization condition:

$$\frac{1}{4\pi} \int_{4\pi} \chi(\theta_s) d\Omega = 1. \quad (3.47)$$

For example, for Rayleigh scattering, the phase function takes the form:

$$\chi(\theta_s) = \frac{3}{4} (1 + \cos^2 \theta_s), \quad (3.48)$$

however, the more general Henyey-Greenstein model is frequently used [26, 18]:

$$\chi(\theta_s) = \frac{1 - g^2}{(1 + g^2 - 2g \cos \theta_s)}. \quad (3.49)$$

This empirical formula is characterized by the parameter g which characterizes the anisotropy of the internal scattering. A value of $g < 0$ favours backward scattering while $g > 0$ favours forward scattering. Huber et al. estimated these parameters for PTFE

finding positive values of g [76]. The authors in [26] estimated g values between 0.6 and 0.7 for Spectralon®. In the case of isotropic scattering $g = 0$ and the phase function $\chi(\theta_s)$ takes the value of 1, reducing to the Lambert's law.

Despite the fact that isotropic scattering is not observed for PTFE and Spectralon®[26], it is a common assumption that most subsurface scattering in dielectrics is isotropic [20], with azimuth-symmetric reflection with respect to the surface normal. In these conditions, in his comprehensive and groundbreaking work on Radiative Transfer, Chandrasekhar derived the exact solution for the bi-direction reflectance factor from a semi-infinite scattering medium [34] (using the same notation as above):

$$R(\mu', \mu) = \frac{\rho}{2} \frac{\mu'}{\mu + \mu'} H(\mu, \rho) H(\mu', \rho). \quad (3.50)$$

The H functions are called the Ambartsumian-Chandrasekhar H function, and describe the intensity of radiation scattered in the semi-infinite scattering medium. It is the solution of the following non-linear integral equation:

$$H(x, \rho) = 1 + \frac{\rho}{2} x H(x) \int_0^1 \frac{H(x')}{x + x'} dx'. \quad (3.51)$$

Various tabulations for this equation over multiple parameters exist, computed for example by Chandrasekhar and Breen, and published in Chandrasekhar's book [77]. It is common however to approximate the H function, Hapke presents such an approximation, with a maximum 1% error over the whole parameter space [73]. As x goes to 0 then $H(x)$ goes to 1, indicating that for large angles of incidence single scattering is what matters. Additionally, since $H(x)$ is almost linear over most of its range, an obvious approximation is of the form $H(x) \approx A + Bx$, where the integral over x is required to be equal to the average of $H(x)$, or in other words, its 0th moment, whose exact value can be computed and is widely known:

$$h_0 = \int_0^1 H(x) dx = \frac{2}{\rho} (1 - \sqrt{1 - \rho}) \quad (3.52)$$

Thus, it follows that $A + B/2 = h_0$ and since $H(0) = 1$ it makes sense to pick $A = 1$, resulting in the approximation:

$$H(x) \approx 1 + 2\left(\frac{2}{\rho}(1 - \sqrt{1 - \rho}) - 1\right)x = 1 + 2r_0x \quad (3.53)$$

Where

$$r_0 = \frac{2}{1 + \sqrt{1 - \rho}} - 1 \quad (3.54)$$

The approximation in equation 3.53 can be substituted in 3.51 to yield, after manipulation, Hapke's approximation [73]:

$$H(x) \approx \left[1 - (1 - \sqrt{1 - \rho})x \left\{r_0 + \left(1 - \frac{\rho}{2} - r_0x\right) \ln \frac{1+x}{x}\right\}\right]^{-1} \quad (3.55)$$

Figure 3.9 shows a polar plot of Chandrasekhar's isotropic diffuse law (eq. 3.50) from [20] in comparison to Lambert's law (dashed line). It is interesting to note that the angular reflection law approximates Lambert's law for increasing albedos, while it flattens out as the albedo moves away from that of a perfect reflector.

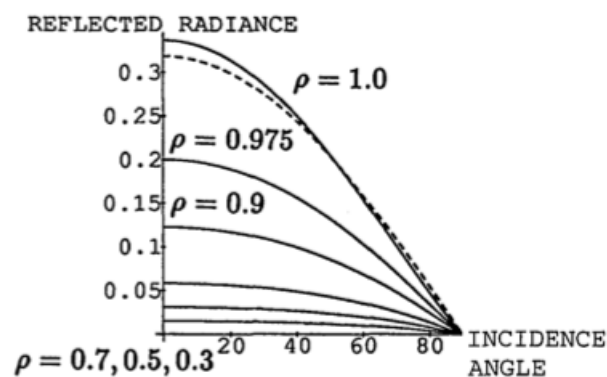


Figure 3.9: Chandrasekhar’s isotropic diffuse reflection at normal viewing for multiple albedos over the range of incident angles, compared with Lambertian reflection (dashed) (borrowed from [20])

Next, we will discuss surface roughness, which is another important factor when modelling reflectance due to its impact in the angular distribution of reflection.

3.4 Reflection from Rough Surfaces

Early studies of reflection from rough surfaces were motivated by the need to model the observed visible and infrared reflectance data from the Moon’s surface. Studies indicated that the Moon’s surface radiates more energy back towards the sun than in the normal or forward direction, this is called backscattering [24]. Roughness is very complex and often impossible to describe in complete detail, and, instead, it is approximated by several statistical parameters.

The height distribution function [16], approximates the surface by a random variation from an ideally smooth plane surface. The height function $h(x, y)$ maps the height profile across the x, y plane and it is defined such that its average is zero. The root mean square of the distribution is of the form,

$$\sigma_h = \sqrt{\frac{1}{S} \int_S h^2(x, y) dx dy}, \tag{3.56}$$

where S is the surface area being described. The root mean square quantifies the variations with respect to the smooth plane and it is used to describe surface roughness. It can be experimentally probed by measuring the height of multiple points across the surface, even though it would be impossible, of course, to know its exact form across the entire surface. Thus, in practice, a distribution function $P_z(h)$ is used, defined as the probability to find in the vicinity of x, y a height with value within the interval $[h, h + dh]$.

To accurately describe a surface’s roughness with this model, it is also necessary to take into account the correlation function, $C(x_2 - x_1, y_2 - y_1)$, which ultimately constraints the variation of $h(x, y)$ across the surface with respect to the distance separating two points. For a surface profile formed by a truly random process, it is common to assume a Gaussian form both the probability distribution and correlation functions:

$$P_z(h) = \frac{1}{\sqrt{2\pi}\sigma_h} \exp\left\{\frac{-h^2}{2\sigma_h^2}\right\}, \tag{3.57}$$

$$C(r) = \exp\left\{\frac{-r^2}{T^2}\right\}, \quad (3.58)$$

where r is the distance between two points and T , the correlation length, is the average length such that $C(T)$ falls to $1/e$. A Gaussian distribution of heights has been observed for lunar soil [78], rubber [79], fused quartz [80] and metallic deposits [81]. However, not all surfaces are produced by truly random processes. In that case, the skewness of a surface can be computed, resulting in a skewed probability distribution to describe it [16].

Another distribution is the slope distribution model. In this model, surface structure is approximated by a collection of micro-facets, each with its own local normal, n' , distributed around a global normal, n . Thus, the slope of a facet, α , is given by the angle between n' and n , with a value of $\pi/2$ at most. A surface's roughness will be characterized by a probability distribution function, which, in the case of an isotropic rough surface, it is sufficient to describe the distribution of the alpha angles, $P(\alpha)$, otherwise, the azimuthal angle is also needed, $P(\alpha, \phi_\alpha)$. The probability function should respect the following normalization condition [16]:

$$\int_{-\pi}^{+\pi} \int_0^{\frac{\pi}{2}} P(\alpha, \phi_\alpha) \cos \alpha \sin \alpha d\alpha d\phi_\alpha = 1. \quad (3.59)$$

It is clear from this discussion, that the expressions to describe the roughness of a surface are not simple, and their complexity make computing the scattering of electromagnetic waves a difficult matter.

Consider two media, where the surface of medium 2 interfacing with medium 1 is described by a height distribution $h(x,y)$. Consider the propagation of monochromatic and non-polarised radiation. The reflected fields above the surface and the transmitted fields below the surface are understood by solving the corresponding Helmholtz equations, which hold for both sides of the surface [82, 16]:

$$\nabla^2 E(\mathbf{r}) = k_1^2 E(\mathbf{r}), \quad z > h(x, y), \quad (\text{medium 1}), \quad (3.60)$$

$$\nabla^2 E(\mathbf{r}) = k_2^2 E(\mathbf{r}), \quad z < h(x, y) \quad (\text{medium 2}), \quad (3.61)$$

where $k_1 = \frac{2\pi n_1}{\lambda}$ and $k_2 = \frac{2\pi n_2}{\lambda}$ are the respective wave numbers. The Helmholtz equations can be solved using Green's theorem, resulting in [83]:

$$E(\mathbf{r}) = \frac{1}{4\pi} \oint_S dS [G(\mathbf{r}, \mathbf{r}') \nabla E(\mathbf{r}') - E(\mathbf{r}') \nabla G(\mathbf{r}, \mathbf{r}')]. \quad (3.62)$$

The Green functions need to obey the boundary conditions for the Maxwell equations [82, 16]:

$$\begin{aligned} E^{in}(\mathbf{r})|_{z=h^+(x,y)} &= E^{out}(\mathbf{r})|_{z=h^-(x,y)} \\ \left[\frac{\partial E^{in}(\mathbf{r})}{\mathbf{n}'} \right]_{z=h^+(x,y)} &= \left[\frac{\partial E^{out}(\mathbf{r})}{\mathbf{n}'} \right]_{z=h^-(x,y)} \end{aligned} \quad (3.63)$$

where $\frac{\partial}{\partial \mathbf{n}'} = \mathbf{n}' \cdot \nabla$, \mathbf{n}' being the local normal:

$$\mathbf{n}' = \left(\sqrt{1 + (h'_x)^2 + (h'_y)^2} \right)^{-1} (h'_x \hat{e}_x + h'_y \hat{e}_y + \hat{e}_z), \quad h'_i = \frac{\partial h(x, y)}{\partial i}. \quad (3.64)$$

The enclosed surface in this instance of the Green's theorem refers to the volume (medium 1) above the surface and so it can be divided in two regions: an upper half sphere of infinite radius S^{inf} and the rough surface S' described by $h(x,y)$ [82]. Naturally, the integral relative to S^{inf} results in the incident electrical field E_0 . The scattered field will in turn depend on the height distribution function because of the local normal \mathbf{n}' :

$$E(\mathbf{r}) = E_0 + \frac{1}{4\pi} \oint_{S'} dS' [G(\mathbf{r}, \mathbf{r}') \frac{\partial E(\mathbf{r}')}{\mathbf{n}'} - E(\mathbf{r}') \frac{\partial G(\mathbf{r}', \mathbf{r}')}{\mathbf{n}'}]. \quad (3.65)$$

In most cases, the integral of equation 3.65 cannot be solved analytically due to the complexity of the $h(x,y)$ function. Numerical methods exist, however they present elevated computational costs and complexity. Other alternatives are for example perturbation methods, for cases of moderate to little roughness [84]. Alternatively, the Kirchhoff approximation assumes that each point has the same optical properties as the plane tangent to it. This means the total scattered field will be the sum of the reflected fields originating at each local plane as given by the Fresnel equations. Thus, it only works in the limit where the surface appears locally flat to the incident wavelength [16].

Naturally, the scattering of the electromagnetic field on a surface will be correlated with the surface's roughness. It follows that the electric field can be described by a random function over (x,y) . It will have an average $\langle E \rangle$, generally called the coherent field, and an additional zero-average fluctuating field, F , called the incoherent field:

$$E(\mathbf{r}) = \langle E \rangle + F(\mathbf{r}). \quad (3.66)$$

The intensity of the scattered field will be $I = E(\mathbf{r})E^*(\mathbf{r})$, which can be written as:

$$EE^* = \langle E \rangle \langle E^* \rangle + \langle E \rangle F^* + \langle E^* \rangle F + FF^*. \quad (3.67)$$

Thus, the average intensity can be written as the sum of a coherent and an incoherent component [16]:

$$\langle I \rangle = I_C + I_D$$

$$I_C = \frac{\epsilon}{2} |\langle E \rangle|^2 \quad (3.68)$$

$$I_D = \frac{\epsilon}{2} \langle |F|^2 \rangle = \frac{\epsilon}{2} \langle |E|^2 \rangle - \frac{\epsilon}{2} |\langle E \rangle|^2.$$

The coherent field intensity corresponds to the specular spike that is observed in data [31]. It can be seen that this effect of the average field can only be observed at the specular direction, where the reflected waves are all in phase. Additionally, it decreases with increasing roughness and with decreasing incident wavelength [16]. The incoherent intensity corresponds to the specular lobe, and since it consists of a fluctuating field around the average field, it is oriented in the same general direction as the specular spike.

3.4.1 Geometric Optical Approximation

In the limit where dimensions of the irregularities on a surface are significantly larger than the wavelength of incident light ($\sigma/\lambda \gg 1$) the geometric optical approximation (GOA) can be used. This is a more straightforward approach with less computational costs, which describes reflection off surfaces of different scales of roughness with significant

success. Generally, it models a surface as a collection of micro-facets randomly oriented and with dimensions much larger than the incident wavelength [16].

Torrance and Sparrow, for example, use a collection of v-cavities to model specular reflection in rough surfaces, each cavity displaying two opposing faces [66]. Figure 3.10, shows such a v-cavity to illustrate how roughness can affect reflectance. A distant source illuminates both facets, assuming both have the same reflectivity, the left facet will be brighter since it receives more incident light. However, when seen from a distant observer on the left, a larger fraction appears darkened then when seen from the viewing direction of the source. This observation is inline with the increased backscattering of rough surfaces, as is the case of the Moon [85].

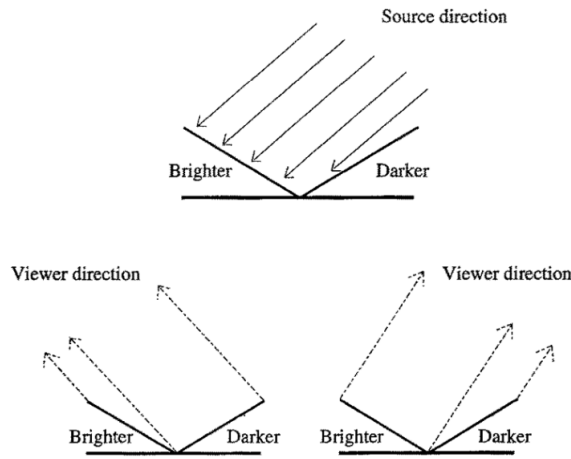


Figure 3.10: Illustration of a v-cavity and the dependence of reflected light on viewing angle. From [24]

The model of Torrance and Sparrow [66] assumes the micro-surfaces are specularly reflecting and are isotropically distributed around the surface normal following a normal distribution with zero average:

$$P(\alpha, \sigma) = \frac{1}{\sigma_\alpha \sqrt{2\pi}} \exp\left\{-\frac{\alpha^2}{2\sigma_\alpha^2}\right\}, \quad (3.69)$$

where σ_α is the standard deviation of the slope angle α and represents, ultimately, the surface roughness. In practice, a normalisation constant needs to be added to $P(\alpha, \sigma_{alpha})$ to verify the normalisation condition 3.59. Later, Cook and Torrance [86], when developing a comprehensive reflectance model for computer graphics utilised instead the Beckman distribution function, which doesn't need arbitrary normalisation factors and takes the following form:

$$P(\alpha, m) = \frac{1}{\pi m^2 \cos \alpha^4} \exp\left\{-\frac{\tan \alpha^2}{m^2}\right\}, \quad (3.70)$$

where $m = \sqrt{2\sigma}$ represents the surface roughness in this instance.

Quantitatively, a collection of micro-surfaces is oriented according to a probability distribution function $P(\alpha)$ as introduced above. With \mathbf{n} the average surface normal and \mathbf{n}' the local normal, the α angle is given by $\alpha = \arccos(\mathbf{n} \cdot \mathbf{n}')$. The incident flux upon an element δA of surface illuminated by a source of radiance L_i and associated solid angle Ω_i is:

$$d\Phi_i = L_i \cos \theta_i \delta A d\Omega_i. \quad (3.71)$$

The number of local normals \mathbf{n}' falling within a solid angle $d\Omega'$ will be $P(\alpha)d\Omega'$, and the corresponding area of micro-facets falling on such solid angle is $P(\alpha)d\Omega'\delta A$. Thus, the incident flux will be:

$$d\Phi'_i = L_i \cos \theta'_i \delta A d\Omega_i P(\alpha) d\Omega', \quad (3.72)$$

where θ'_i is the angle that the incident radiation makes with the local normal \mathbf{n}' (see figure 3.11). In turn, the specularly reflected flux from surface area δA into a direction \mathbf{r} is, in terms of the incident flux:

$$d\Phi_r = F(\theta'_i) G d\Phi'_i = F(\theta'_i) G d\Phi_i \frac{\cos \theta'_i}{\cos \theta_i} P(\alpha) d\Omega', \quad (3.73)$$

where $F(\theta'_i)$ is the Fresnel coefficient and G a geometric attenuation factor that accounts for effects such as masking and shadowing (see figure 3.11) [87]. Masking occurs when a facet is hidden by another facet and does not receive light from a particular direction. Shadowing is when reflected light from a facet is hidden because it is blocked by another surface in a certain viewing direction. Dependence is suppressed for legibility, but besides being dependent on the local θ'_i angle, the Fresnel coefficient is also dependent on the refractive indices of the two media.

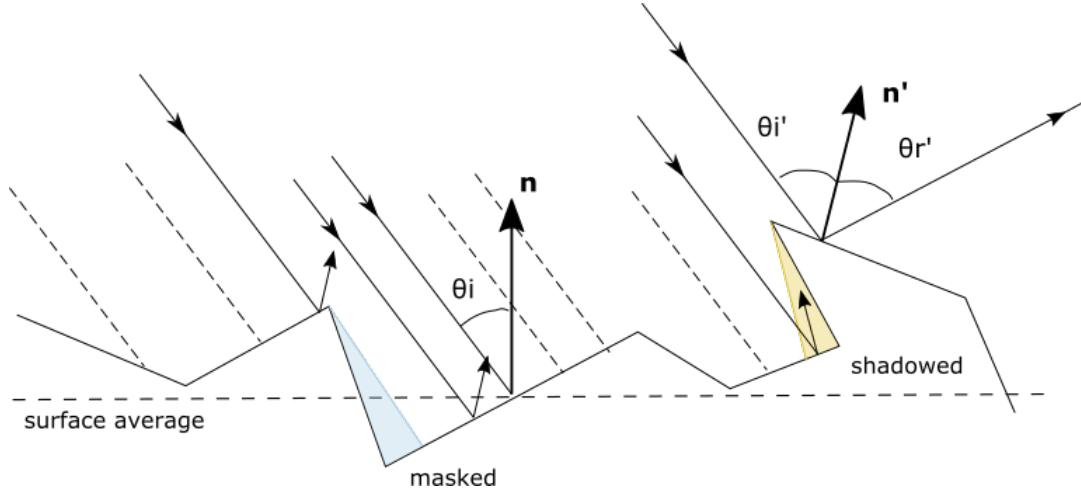


Figure 3.11: Geometry of rough surfaces. Note that if reflection is considered specular, then $\theta'_i = \theta'_r = \theta'$. Masking and shadowing effects are illustrated too.

The geometric attenuation factor accounts for the fraction of light that effectively gets reflected from direction \mathbf{i} into \mathbf{r} once the masking and shadowing effects are taken into account. To model this factor, we can use the Smith model which can be employed to any micro-surface distribution function [87]. The details of the model are complex but more information can be found in [16, 87].

Finally it is important to note that the geometric optical approximation does not take into account wavelike interactions, thus the coherent field is left out of the picture. Models using the GOA, need to include the specular spike intensity manually [16].

3.5 The Wolff and Oren-Nayar Model

In this section we describe a model that takes into account both diffuse reflection and the effect of surface roughness. Wolff developed a diffuse reflectance model for smooth dielectric surfaces coupling radiative transfer results for isotropic scattering to Fresnel attenuation and Snell refraction at the surface interface, both incoming and outgoing [20]. Oren and Nayar, in turn, worked on a generalisation of the Lambertian model for rough surfaces, to account for the dependence of the reflectance on the viewing angle. The Wolff and Oren-Nayar model described in [31] combines these two approaches, applying Wolff's diffuse reflectance factor for each micro-facet surface. A brief description of this model and account of its implementation is given in this chapter.

In diffuse reflection, light refracted to the inside of the diffuser can be reflected in the diffuser/original-medium interface multiple times, leading to more subsurface scattering. Figure 3.12 shows this effect schematically, where a first reflection at the diffuser/air interface is termed the first-order reflection, a second time is called second-order reflection and so on. Naturally, the higher-order reflections will be less and less probable.

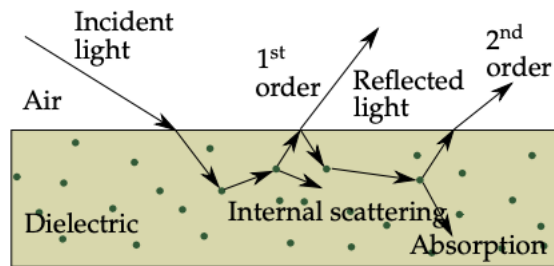


Figure 3.12: Schematic of internal scattering in the bulk of material, showing multiple reflections in the dielectric/air interface (from [16]).

Wolff writes down the following expression for the first-order diffusely reflected radiance, that is, that fraction which goes into the dielectric, scatters internally and comes back out:

$$\rho_1 L_i \left[1 - F\left(\theta_i, \frac{n_2}{n_1}\right) \right] [\cos \theta_i] \left[1 - F\left(\sin\left(\frac{\sin \theta_r n_1}{n_2}\right)^{-1}, \frac{n_1}{n_2}\right) \right] d\omega. \quad (3.74)$$

The term ρ_1 is called the first-order or single diffuse albedo and it expresses the probability that a photon refracted into the diffuser returns back to the original medium. The first Fresnel term is the fraction of incident light that gets refracted into the diffuse medium $[1 - F(\theta_i, \frac{n_2}{n_1})]$, while the second Fresnel term $[1 - F(\sin(\frac{\sin \theta_r n_1}{n_2})^{-1}, \frac{n_1}{n_2})]$, is the light that gets refracted out of the medium, where the viewing angle before refraction (remember figure 3.6) is given by Snell's law, together they are the Wolff term W :

$$W = [1 - F(\theta_i, \frac{n_2}{n_1})] \times [1 - F(\sin(\frac{\sin \theta_r n_1}{n_2})^{-1}, \frac{n_1}{n_2})]. \quad (3.75)$$

The first-order diffuse albedo is given by:

$$\rho_1 = \frac{\rho n_2^2}{4\pi n_1^2} \frac{H_\rho(\mu'_i) H_\rho(\mu'_r)}{\mu'_i + \mu'_r}. \quad (3.76)$$

where ρ is the single scattering albedo (eq. 3.46) and the μ' terms are the cosine of the internal incident and reflected angles, used as arguments for Chandrasekhar's H functions. In accordance with Fresnel laws, light can be reflected back into the dielectric to undergo subsurface scattering again, some fraction of that can be yet again reflected back onto the dielectric, and so on. In this way, the Nth-order diffuse reflection comes from light specularly reflected N-1 times, and it is expressed in the following way:

$$\rho_1^N L_i \left[1 - F\left(\theta_i, \frac{n_2}{n_1}\right) \right] [\cos \theta_i] K^{N-1} \left[1 - F\left(\sin\left(\frac{\sin \theta_r n_1}{n_2}\right)^{-1}, \frac{n_1}{n_2}\right) \right] d\omega. \quad (3.77)$$

So one can write a total diffuse albedo which is the sum of all contributions ($\rho_1 + \rho_1^2 K + \rho_1^3 K^2 + \dots$), which is nothing but a geometric series that can be given by:

$$\rho_d = \frac{\rho_1}{1 - K}. \quad (3.78)$$

The K term is an integral term dependent on equation 3.50 that accounts for all the internal reflections in the discontinuities in the bulk of the material, more details can be found in the original article [20]. In practice however, both ρ_1 and K are considered constant without compromising significantly the precision of the model. Hence, the BRIDF for smooth surfaces given by the Wolff model can be written as [18]:

$$\varrho_r^I(\theta_i, \theta_r) = \frac{1}{\pi} \cos \theta_r \rho_d W. \quad (3.79)$$

This is a modified Lambert's law. Smooth diffuse surfaces are typically darker than predicted by Lambert's law, especially for larger incident θ_i and viewing angles θ_r , resulting in a "rounder" appearance. Rough surfaces, however, are generally brighter than predicted by Lambertian reflectance. For example, the Moon gets its bright "flat" appearance due to this effect [31].

As we saw previously, the roughness of a surface affects the distribution of diffused light, increasing the observed radiance as the viewing direction approaches the incident direction. This effect is explained by the Oren-Nayar model [24], where a rough surface is described by a collection of micro-surfaces with random orientation. For larger viewing angles there's a foreshortening of the microspheres. In turn, microspheres whose surface normals are aligned with the incident angle receive larger amounts of light (see figure 3.10).

Oren and Nayar developed an analytical model based on the Torrance and Sparrow distribution function 3.69, where the micro-surfaces are distributed around the surface normal with a Gaussian form with zero average. Each micro-surface reflects light according to the Lambert law. Shadowing and masking effects are described by the Torrance and Sparrow geometric attenuation factor, G, mentioned in section 3.4.1 [66]. More details can be found in the original paper by Oren and Nayar [24].

In the Wolff and Oren-Nayar combined model, Lambert's law is substituted by the Wolff's modified Lambert law (eq. 3.79), so that each micro-surface reflects light according to the Wolff model.

3.5.1 The Modified Wolff Model

The implementation of the Wolff and Oren-Nayar model used in this thesis, henceforth, the modified Wolff model, has some slight differences and added features. Most of these

differences are because the original model is analytical, and the model we used is a Monte Carlo implementation of the model by Silva [16].

In regards to surface roughness, this implementation uses a MC method to generate the local normals, which besides the Torrance and Sparrow distribution function, can also use the Trowbridge-Reitz distribution. The latter models surface irregularities as spheroids and has been used to model the reflection of materials like leaves and bark [16]. For the shadowing and masking probabilities, accounted for by the geometric attenuation factor, the Smith model is used [87]. Additionally, since the Oren-Nayar GOA approach does not include the coherent field effect, the implemented model has an additional, separate, factor to account for the specular spike.

For the diffuse reflectance component, the modified Wolff model uses an approximation to the Chandrasekhar diffuse scattering law (eq. 3.76), by defining a constant multiple-scattering albedo ρ_l^1 . This quantity is the probability that the light refracted into the diffuser returns back to the interface with the first medium. In contrast with the single diffuse scattering albedo of the original model, ρ_l^1 does not depend on the optical interface with the first medium and is a function only of the scattering and absorption properties of the diffuser. The internal scattering follows a Lambertian distribution. The multiple scattering albedo is related to the total diffuse albedo in the original model by:

$$\rho_d = \frac{1}{P_T} \left(1 - \frac{1 - \rho_l^1}{1 - \rho_l^1 P_R} \right), \quad (3.80)$$

where the quantities P_R is the probability of internal reflection at the interface between the diffuser and the first medium. P_T is the probability that the light refracted into the diffuser returns back to the first medium. More details of how these two quantities are computed can be seen in the original work [16]. Silva et al. computed these values in a PTFE-air interface ($P_R = 49\%$, $P_T = 91\%$) and in a PTFE-water interface ($P_R = 2\%$, $P_T = 99\%$) [16].

This is of special relevance for this work. Since we are interested in studying the change in reflectance when the interface changes from air to a liquid interface, it is important to have a parameter that describes the diffuser separately from the optical interface.

The modified Wolff model described here was implemented in ANTS2 for the analysis of the reflection of PTFE in LXe by Neves et al. in [12]. In a similar way, this model is used in the MC analysis in ANTS2 of the experimental data of the diffuse reflectance of Spectralon® in a liquid interface.

Chapter 4

Experimental Set-up and Simulations

This chapter describes the experimental set-up developed to study diffuse reflectance at a PTFE-liquid interface as well as the simulations accompanying the experimental work. The Monte Carlo (MC) simulations developed in this thesis are doubly motivated. Not only they informed us during the phase of designing the experiment, but they also are a powerful tool for analysing and interpreting experimental data.

First, an overview of the set-up and each subsystem is given. Next, the use of total integrating spheres (TIS) in radiometry is discussed as well as the relevant mathematics. This is followed by a detailed explanation of the adaptation of the TIS for use with liquids. This includes explaining the purpose and function of the custom pieces that were specially made for the purpose. Next, a description of the light input system, composed of the LED matrix and collimation system, is given. Additionally, the developed Monte Carlo simulations of the collimation system are discussed. These simulations consist in ray tracing of randomly generated photons to study the angular distribution of the photons across the collimation system and into the sphere.

Finally, the last section details the use of the ANTS2 software package for the optical simulations of the experiment. ANTS2 was initially developed to study anger camera type detectors. It has also been used for designing the PMT arrangement in the LUX-ZEPLIN dark matter experiment[32]. For this thesis, ANTS2 was used to simulate the light propagation in the experimental set-up and to test the Lambert model and a modified version of the Wolff model against the experimental data.

4.1 Experimental Set-up Overview

The experimental set-up developed can be divided into four interconnected subsystems:

1. the Total Integrating Sphere and peripherals, which contains all the optical interfaces of interest for our study;
2. the light input system, with multiple LEDs over a broad range of wavelengths, and a collimation system;
3. the PMT for photo-detection and associated signal acquisition electronics;
4. the experiment control system, including microcontrollers, electronics and software.

The last two will be discussed in more detail in the next chapter. The collimation system, the TIS and the PMT are installed inside a vacuum chamber. Even though measurements in a controlled atmosphere/vacuum measurements are not required in our case, they are possible in the future. The internal surfaces of the chamber were painted with ultra matte black paint from TS Optics [88] and most metallic surfaces were anodised. Figure 4.1 shows a photo of the set-up inside the blackened chamber.

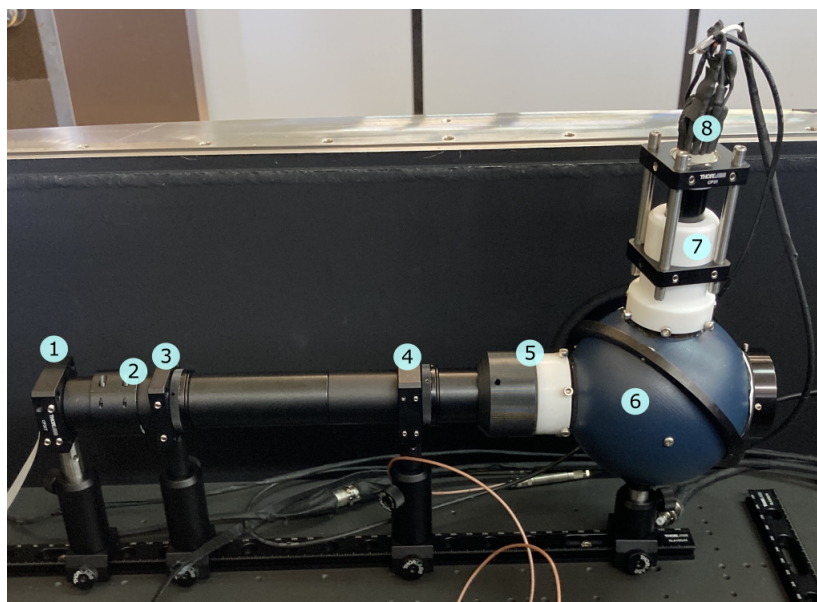


Figure 4.1: Photo of the experimental set-up inside the optical chamber: (1) LED matrix; (2) diffuser window; (3) first pinhole; (4) second pinhole; (5) light input port with a fused quartz window and Spectralon® pinhole on the inside; (6) Integrating Sphere; (7) PMT holder piece, also from where the sphere is filled with liquid; (8) PMT and PMT base.

The total integrating sphere connects to the collimation system through a custom made port that includes a fused quartz window as well as a Spectralon® pinhole. The window is important to isolate the inside of the sphere from the collimation system when performing measurements in a liquid interface. Attached to the port on the top is an adaptor to accommodate the PMT. The vertical posts guarantee the PMT is always in the same position. The sphere is also filled with liquid from this port when the PMT is removed. The PMT being used is the R762P head-on bialkali PMT from Hamamatsu®. It has an outer diameter of 19.7 mm and a length of 88 mm. It has a quartz window with 16.5 mm diameter and a photosensitive active area with 15 mm diameter.

The light input system consists of 7 LEDs of different wavelengths (255–490 nm) arranged in a PCB matrix followed by a UV fused silica ground glass diffuser from Thorlabs and a collimation system with two pinholes. The system has a total length of 259 mm, from the LED matrix to the Spectralon® pinhole at the sphere's entry. The system attaches to the quartz window port adaptor mentioned above. The LEDs are switched on and off, and the light intensity is controlled via an electronic board plugged to an Arduino Uno micro-controller board. The electronics is built in such a way so that only one LED, if any, is on at any moment.

This set-up allows to take measurements in multiple runs at different wavelengths, first in the air and then in the liquid interface, without any mechanical adjustments with the light input system and sphere. This guarantees that from one run to another, the

geometry is maintained exactly the same. Additionally, the TIS and the custom adaptor ports are designed to ensure that the only optical interfaces in contact with the interfacing medium are either the interior walls of the sphere (or similar material) or the quartz of the input and PMT windows. The interior surface of the sphere is what we wish to study, while the optical properties of fused quartz are very well known due to its widespread use in multiple applications from spectroscopy, UV and IR applications to the Apollo missions [89].

4.2 The Total Integrating Sphere

Total integrating spheres (TIS) are used in scientific and industrial applications to characterise light sources and measure the transmittance and reflection of samples [28]. The sphere uses a highly reflective diffuse material in its interior to, ideally, distribute the light uniformly across the entire surface. A photodetector placed at the face with the surface of the sphere collects the amount of light in proportion to the surface it covers. This is the best method to measure the directional-hemispherical reflectance without using a model to integrate over the whole hemisphere. It is not possible, however, to obtain the BRIDF using a TIS. While the BRIDF is defined with respect to the reflected radiant intensity in a viewing direction (θ_r, ϕ_r) , the TIS measures the light integrated over the entire hemisphere.

To measure the BRIDF of a sample for different incident and viewing angles, a goniometer has to be used. This instrument allows rotating both the sample and the photosensor to a precise angular position. It covers the entire range of incident and viewing angles only limited by the precision of the positioning system. This type of reflectance measurement is called an angle-resolved scattering method. One was employed, for example, in [18] to measure the reflectance of PTFE in the VUV range. In contrast to a total integrating sphere, however, a goniometer is not as precise for measuring total reflectance. It is impractical to take measurements over the entire hemisphere. Generally, the total reflectance needs to be extrapolated from the data, and analysis is complex and model-dependent.

In our case, since we are interested in studying how diffuse reflectance changes in a liquid interface a total integrating sphere can be a powerful tool. They have been used multiple times before to measure the directional-hemispherical reflectance of diffuse materials [17, 26]. The standard ISO/DIS13696 defines the total scattering as the ratio between the scattered power on a sample for a given wavelength and the incident radiation power, $P_s(\lambda)/P_i(\lambda)$. Total integrating spheres are generally the best method to measure this quantity [17]. Another use of TIS is in the ASTM F1048 standard test method to evaluate the roughness of a surface. This is done by defining the total integrated scattering as the ratio between the diffuse reflectance and the total reflectance of a surface.[90]. The amount of diffuse reflectance is then related to the root mean square of a height distribution describing the surface under study, according to the scalar diffusion theory of Beckmann [90].

4.2.1 Integrating Sphere Theory

A TIS works by diffusing light evenly over the entire surface of the sphere. In an ideal scenario, it guarantees that every point within the sphere receives the same amount of light. This is possible by combining two factors, a Lambertian reflecting surface (equation

3.40) and a spherical shape. This may seem obvious, but it is helpful to work through the geometry of the sphere and its implications. Start with two Lambertian surface elements, dA_1 and dA_2 , arbitrarily oriented, separated by a distance h . The energy fraction that arrives at dA_2 from dA_1 is given by [91]:

$$dF_{d_1-d_2} = \frac{\cos \theta_1 \cos \theta_2}{\pi h^2} dA_2, \quad (4.1)$$

where θ_1 and θ_2 are the angles the incident light makes in respect to the surface normals. The energy fraction from dA_1 to dA_2 is called the exchange factor. If we now consider two points on the internal surface of a sphere (figure 4.2), we can write:

$$h = 2R \cos \theta_1, \quad \text{with} \quad \theta_1 = \theta_2, \quad (4.2)$$

where R is the radius of the sphere. So, substituting this result in equation 4.1, we get the exchange factor inside a diffusely radiating sphere:

$$dF_{d_1-d_2} = \frac{dA_2}{4\pi R^2} = \frac{dA_2}{A_s}, \quad (4.3)$$

where A_s is the area of the sphere. This is an interesting result that shows that the radiation received by a surface element is independent of viewing angle or distance to the source. The fraction of light received is the same as the fraction the surface takes up within the area of the sphere. This is only made possible due to the spherical geometry.

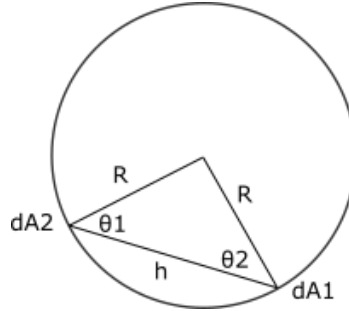


Figure 4.2: Exchange factor in a spherical geometry.

After the first reflection on the sphere, the input flux will be perfectly diffused over the surface. Thus, the amount of flux over the entire sphere surface will be $\Phi_S^1 = \Phi_i \rho_l (1 - f)$, where ρ_l is the Lambertian albedo (equation 3.40) and f is the fraction of the sphere area taken up by non-reflecting materials, also known as the port fraction. In a real application, at least one port opening for the light input and another for light detection are needed. Similarly, for the second reflection, the amount of flux over the entire sphere surface will be $\Phi_S^2 = \Phi_i \rho_l^2 (1 - f)^2$, and so, after n reflections:

$$\Phi_S^n = \Phi_i \rho_l (1 - f) [1 + \rho_l (1 - f) + \dots + \rho_l^{n-1} (1 - f)^{n-1}]. \quad (4.4)$$

The term in parenthesis expands into an infinite geometric series with common ratio $\rho_l (1 - f)$. Since $\rho_l (1 - f) < 1$, the series can be given by the closed form $1 / (1 - \rho_l (1 - f))$. It follows that the sphere radiance is given by [91]:

$$L_s = \frac{\Phi_i}{\pi A_s} * \frac{\rho_l}{1 - \rho_l (1 - f)} \quad [\text{W m}^{-2} \text{sr}^{-1}]. \quad (4.5)$$

It should be noted that this equation works only as an approximation since there will hardly be any surface that shows no specular reflection at all, and introducing these kind of interfaces in the sphere complicates things in a non-trivial way. It is nonetheless advantageous to understand the behaviour of the system.

The factor $\frac{\rho_l}{1-\rho_l(1-f)}$ is of particular relevance. It's a multiplier larger than one that works as a sensitivity factor, generally called M . An interesting thing about it is that the albedo ρ_l is in asymptotic relation, and even small changes in its value will have a significant impact on the multiplier factor. This means that integrating spheres can be extremely sensitive to small changes in the reflectance of the interior walls. Intuitively, this can be understood in relation to the high number of reflections within the sphere, having an exponentially increasing dependence on reflectivity as the number of reflections increases. A higher M value means a higher number of reflections before a photon is extinguished, so the integrating power is increased. The integrating power of the sphere is its capacity to deliver a uniform light distribution across the entirety of its surface [28].

Another useful relation is the throughput at a port with area A_p [28]:

$$T_{Port} = \frac{\Phi_i}{\pi A_s} \frac{\rho_l}{1 - \rho_l(1 - f)} A_p \Omega, \quad (4.6)$$

where Ω in this case is π sr, a full hemisphere. If the equation is used to calculate the throughput on a detector, the active area (photosensitive area) must be used instead of the whole area taken up by the detector and the solid angle must be given with respect to the detector's angular field of view, θ : $\Omega = \pi \sin^2 \theta$. Again, this equation is just an approximation with several limitations. Besides the approximation of the port fraction factor, which does not account for reflections, it also does not consider reflection and transmission coefficients at the detector's optical interface.

The two prevailing factors that characterise a TIS are the albedo ρ_l of the internal surface and the port fraction f . Another important, even if subtle, factor, is the sphere diameter or volume. It is readily seen from equation 4.5 that the radiance on each surface element decreases with the increasing area of the sphere. What this means in practice, is that the radiance for each point in the sphere will be proportionally more sensitive to changes in the reflectance of the walls [91].

4.2.2 The Newport 819C-SL-3.3 TIS

For the work developed in this thesis, the Newport® total integrating sphere model 819C-SL-3.3 was used (figure 4.3). The internal bulk of the TIS is made of Spectralon® with 3.3 inches internal diameter and four ports. Spectralon® is a reflectance reference used to calibrate spectral measurements in the visible and near-infrared range. It has the highest hemispherical reflectance in the visible range of all known materials, about 99% for light between 400–1500 nm. It is a thermoplastic resin made of pressed PTFE powder [27]. It is thermally stable up to 350°C and chemically inert to all except the most powerful bases like sodium amide and lithium compounds. However, its structure readily absorbs non-polar solvents like greases and oils, so care is needed to keep the surface free from these contaminants [28].

This TIS model has 4 ports. The 90°, 180° and north pole ports all have 1 inch diameter, while the 0° one is bigger with 1.5 inch diameter. Generally for this model, the 90° degree port is used for the photodetector. A baffle is installed between the 0° and

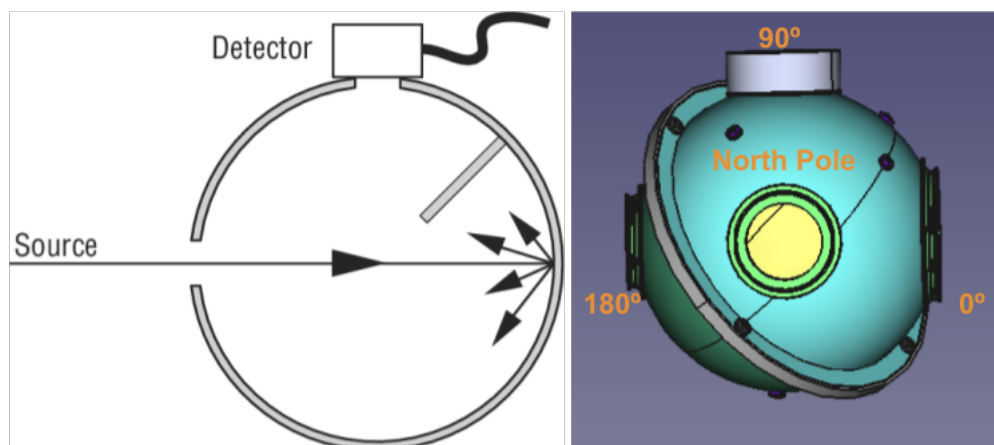


Figure 4.3: On the left a scheme (top view) of the sphere is given, from the Newport website [92]. On the right the top view of the 3D cad model is shown, with the 4 ports identified.

90° ports to avoid the detection of non-integrated light, as shown on the left-hand side of figure 4.3.

Commercially available TIS generally have a sphere multiplier factor (M) between 10 to 25, and it is generally advised to keep port fraction below 5% [28]. Considering the four ports of this model sphere, for a $\rho_l = 0.99$ (Spectralon® value for visible range) a port fraction of 16.3% and an M value of 5.8 is obtained. Bear in mind, however, that while taking data, two of the ports will be closed off by Spectralon® caps. In that case the port fraction becomes 7.2% and the M value becomes 12.1. This value is actually a lower limit on the M factor, in practice, the actual set up has a lower port fraction both due to the spectralon pinhole as well as to the fraction of specular reflection off the PMT window.

4.3 Adapting the TIS for a liquid interface

Some adaptations to the TIS are required to fill it with liquids and make it watertight. PTFE tape was used to seal the interstices on the sphere's diagonal where it opens (screws and a plastic fitting are holding it). The Spectralon® caps that cover the 0° (1.5") and the 90° (1.0") ports were also sealed with PTFE tape and rubber o-rings. Additionally, two custom adaptor ports were developed in conjunction with the LIP workshop, one for the PMT and another for the light input.

4.3.1 PMT Adaptor Port

To have the sphere filled with liquid and kept open to the atmosphere, the top port is used both to fit the detector and to fill the sphere. A custom port adaptor piece was developed to hold the PMT in place. Figure 4.4 shows a section view of the piece. The piece is made of PTFE and is wide enough to allow the PMT to fit, sitting on a ledge so that it is submerged when filled with liquid. A canal exists to evacuate the extra water and make sure the level is maintained stable.

Several tests were made to guarantee the water level was stable and the PMT window remained submerged for the duration of data taking. A tube was fitted to the evacu-

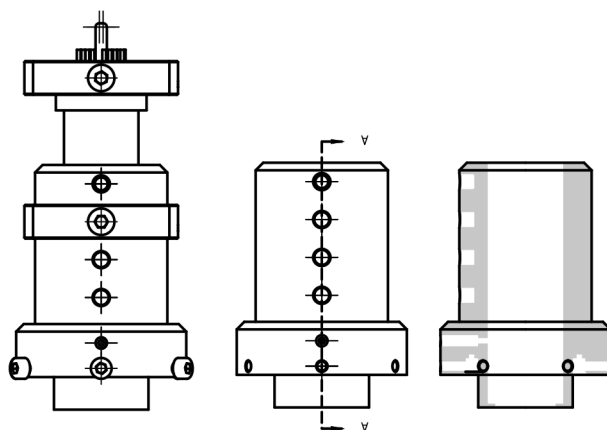


Figure 4.4: Schematic views of the PMT holder: (left) the front view of all the pieces including the PMT; (middle) PTFE adaptor piece attached to the sphere port 90 deg; (right) left-handed vertical section of the middle piece, rotated for legibility.

ation canal with the other end pointing upwards so that it works as a small reservoir. Using this method, it was verified that the liquid level was stable during the experiment, ensuring that the PMT window was always covered with liquid during data acquisition. Nonetheless, a small decrease in the liquid level in the tube was observed right after the filling, which is caused by the hidden interstices within the sphere being filled.

The PMT is held firmly in place using the rod structure shown in the figure 4.5. This structure prevents the PMT from rotating which would affect the accuracy of measurements due to possible asymmetries in the photocathode sensitivity. These rods are held together using two blank cages from Thorlabs, which were adapted in the workshop for this purpose. The top cage attaches to the PMT base while the bottom one screws in with a plastic screw onto the adaptor port piece. This fitting system also allows to easily removal and insertion of the PMT to fill the sphere without affecting mechanically the rest of the system.

The PMT adaptor was redesigned in aluminium with some technical improvements. Because the original piece is made of PTFE, the threads on the piece get very easily worn out, and the fitting of the bottom cage that holds the PMT gets looser with time. The new piece will allow for extra mechanical stability of the PMT. Additionally, some improvements were made to increase the liquid level stability by making additional internal reservoir canals in the piece. Even though the original design worked well with water, it was observed to be inefficient when using ethanol, which has much lower surface tension. Finally, the ledge that holds the PMT will be machined out of Spectralon® so that it is as optically close as possible to the interior surface wall of the sphere.

4.3.2 Light Input Port

The light input port (figure 4.6) needs to satisfy a number of requirements: (a) must isolate the collimation system from the sphere, which will at times be filled with liquids; (b) must have high transmittance across the relevant wavelengths from 255 to 490 nm and, ideally to an even broader range of wavelengths to accommodate possible future

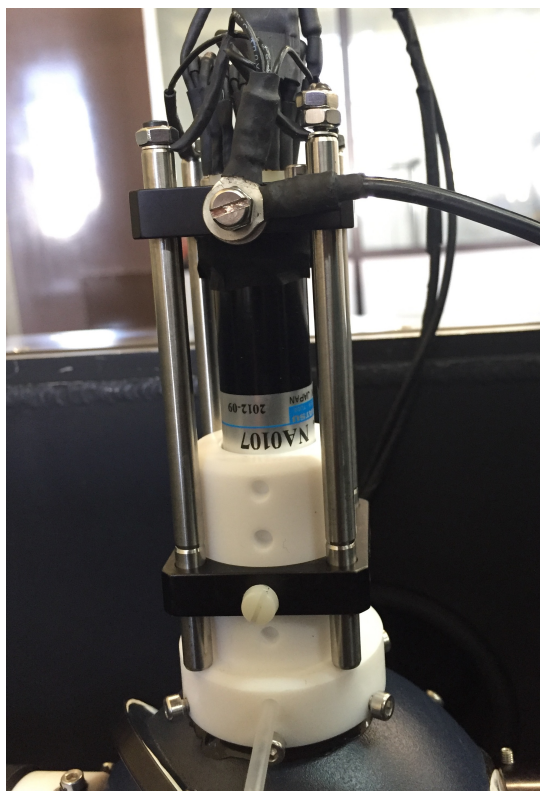


Figure 4.5: close up of the PMT holder with the holding posts to fix the PMT in position. The wiring on top is for base biasing and grounding of the posts.

iterations; (c) should minimise the amount of light scattered back into the collimation system;

To address points (a) and (b), a custom piece was developed and machined to interface the collimation system with the interior of the sphere through a fused quartz window. The 1" diameter window from Crystran Ltd. is made of 6 mm thick optically flat ($\lambda/20$) fused quartz. The flatness of the window is defined in fractions of a reference wavelength, 632.8 nm (He-Ne laser), so in this case that indicates a peak to valley deviation of 31.65 nm. Besides its high optical flatness, fused quartz has a high transmittance for a broad range of wavelengths from 200 nm up to 2500 nm, making it the best option for the input window [93]. To address point (c), the piece also attaches to a Spectralon® pinhole facing the interior of the sphere. This pinhole decreases the opening diameter from 25.4 mm to 5 mm, reducing the amount of light reflected back into the collimation system, which would be a source of systematic uncertainties. Between the pinhole and the fused quartz window fits a light trap made of black POM (figure 4.7). It was machined with multiple creases to trap light with multiple reflections until it is absorbed by the material, making sure that any light that manages to stray back through the pinhole gets absorbed.

Filling and emptying the space between the window and the interior of the sphere became more challenging with the introduction of the pinhole and light trap piece due to the formation of air bubbles. The solution was to carve two symmetric canals along the piece (see figure 4.6), with multiple openings to the inside of the pinhole and into the interior of the sphere as a way to evacuate the air inside as it is filled. When emptying the sphere, they serve the same purpose, to avoid any pockets of liquid left inside. An iteration of this piece was designed in aluminium. Again, the PTFE threads tear down

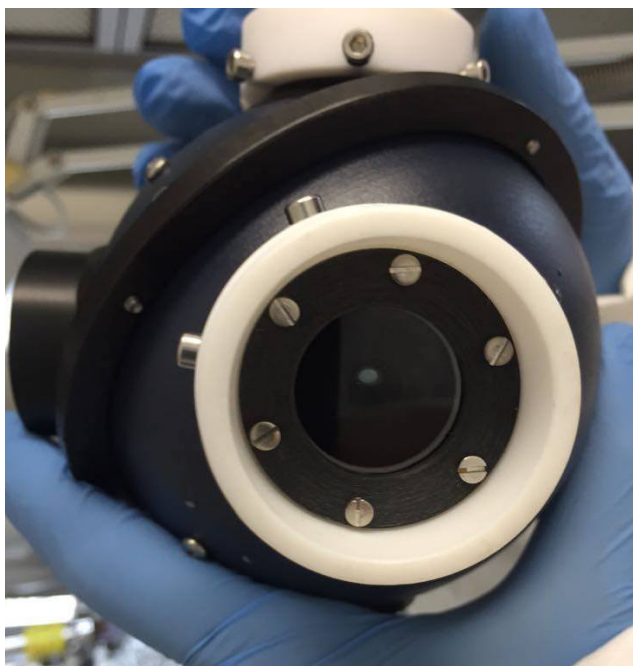


Figure 4.6: Light input port filled with water on the interior of the fused quartz window interface. The back of the pinhole can be seen, which is made of POM plastic with multiple creases to form a light trap.

very easily, so using aluminium should solve that. The upgraded piece has two additional evacuation canals at the top and bottom to make filling and emptying without air bubbles or water pockets easier.

4.4 The LED matrix and the collimation system

It was desirable to test the diffuse reflectance over a wide range of wavelengths. To that end, we decided to use LEDs as light sources, which are a cost-effective solution with readily available electronics to control them. We identified the following list of requirements for the light input system: (a) the photon flux should be highly collimated so as to limit the amount of photons arriving at the photocathode (to avoid damaging it), and to minimise the incident angle on the first reflection to further reduce the chances of reflecting back into the light input system as discussed above; (b) it should be possible to switch between different wavelengths without mechanical intervention in the system; (c) it should also be possible to fine tune the photon flux independently for each LED.

Seven Roithner LEDs from 250 to 590 nm were mounted on a circular PCB support (figure 4.8), henceforth “matrix”, that fitted to the collimation system tubes. The LED PCB matrix connects to an Arduino with a custom shield built to switch the LEDs on and off and adjusting the current fed to them, covering points (b) and (c) mentioned

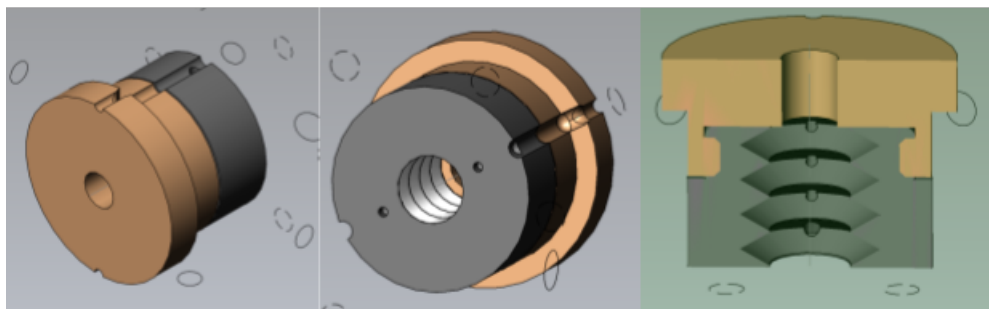


Figure 4.7: 3D CAD picture of the internal pinhole: (left) front; (centre) back; (right) cross section. The front piece is made of Spectralon® while the back piece is a light trap made of black POM. The evacuation canals on the outside of the piece can be seen. These are used to guarantee the space is completely filled with water without any air bubbles.

above. More details about the control electronics are given in the next chapter, section 5.1 on the experiment control. The LEDs are numbered from 1 to 7 according to the output channel that controls them on the Arduino. Four of the LEDs (255, 275, 285 and 310 nm) are surface mount devices (SMD), which are soldered directly onto conducting pads on the PCB. The remaining three (355, 405 and 490 nm) are dual in-line package (DIP) LEDs, with two conducting pins soldered through holes in the PCB. Table 4.1 lists the technical specifications of each LED.

Table 4.1: Roithner® LEDs used in the experiment.

LED	channel	peak wavelength (nm)	spectral FWHM (nm)	radiated power (mW)	viewing half-angle (°)
255	#1	255±5	11	3.5	60
275	#4	275±5	11	2.0	60
285	#7	285±5	11	1.2	63
310	#5	310±5	11	2.0	60
355	#6	356±4	10–20	1.2	30
405	#2	405±5	19	20	13
490	#3	490±10	30	12	28

Before reaching the TIS, the light is highly collimated to ensure that the photon flux is low enough for the PMT to be operated under photon counting conditions. Collimation is also essential to make sure the beam is narrow enough, so there is no backscattering on the reverse side of the Spectralon® pinhole on the input port. The collimation system was built with optomechanical components from Thorlabs®, with a total length of 259 mm and a running diameter of 1" (see figure 4.9). All the optical lens tubes employed in the system were anodised. The collimation system has two configurable pinholes, separated

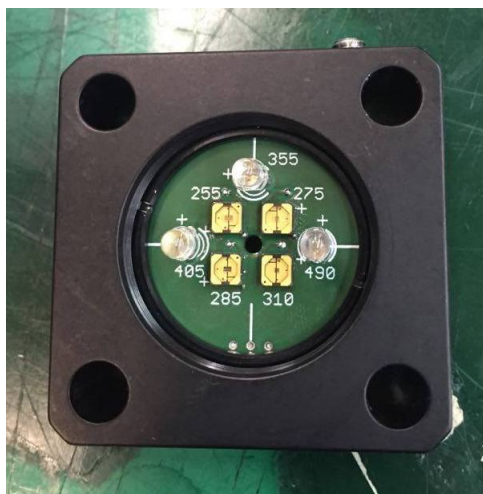


Figure 4.8: Photo of the PCB matrix. The three DIP LEDs were tilted ($\sim 8^\circ$) towards the centre of the diffuser, which was 50 mm away.

by 138 mm. Both pinholes are locked with a 1 mm diameter opening. The tubing system is fixed in place with the help of two SM1 threaded plate cages from Thorlabs®, which attach vertically to a dovetail optical rail through height-adjustable posts. This allows to adjust the position of the whole system in the horizontal plane across the rail and also vertically. Black optical absorbing paper from Thorlabs®, was applied to the last tube that fits into the quartz window port adaptor piece; this further reduces any possible amount of stray light and the associated uncertainties in the modelling.

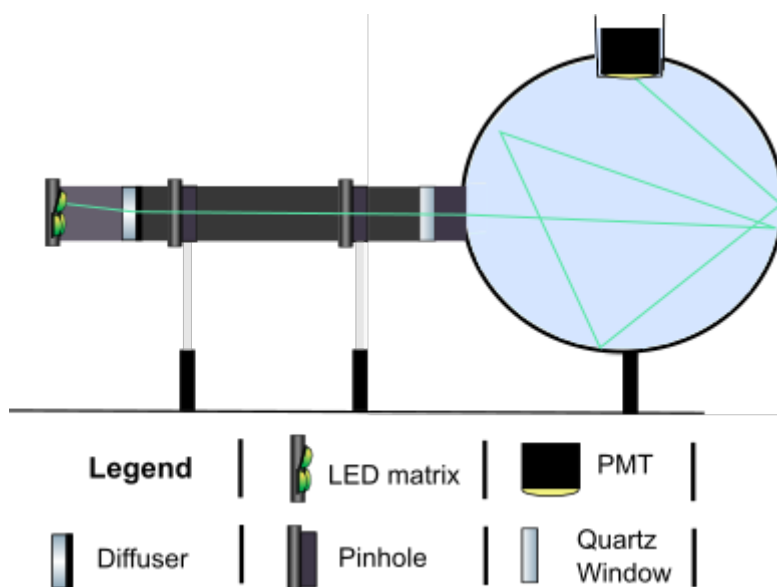


Figure 4.9: Schematic cross-section of the experimental set-up, including details of the collimation system, with the baffle in the sphere's interior not shown for simplicity.

The LED PCB matrix fits into a 0.5" long Thorlabs® optical tube, connected to another 0.5" length tube through a 1" SM1 tube sleeve coupler from Thorlabs®. Next, the DGUV10-220 diffuser from Thorlabs® made of UV fused silica ground glass is installed, 50 mm away from the LED matrix. The diffuser has 1" diameter and a thickness of 0.08" (2.0 mm), it has a high transmittance down to 200 nm: $>85\%$ from 200–250 nm

and $>90\%$ in the range 250–1200 nm. It was manufactured with a 220 grit (average particle is $63 \mu\text{m}$) polish. This coarse polish results in a broader diffusion pattern, according to the datasheet, the output angle distribution is Gaussian with a viewing half-angle of $\sim 7.5^\circ$. The diffuser makes the incident beam profile look the same irrespective of the LED, helping to eliminate systematic errors associated with the positioning of the LEDs. While the SMD LEDs have a broader viewing half-angle, the DIP LEDs have a much narrower angular profile and were tilted towards the centre of the diffuser to maximise the amount of light through the pinholes. The correct tilt angle for the DIP LEDs was found using the collimation system with a photo-diode at the other end, and changing the angle until the maximum signal was achieved. From the geometry of the system, the angle the LED axis makes with the surface normal is $\sim 8^\circ$.

4.4.1 Simulating the Collimation System

Upon the first reflection in the TIS, the beam profile must be well described to avoid undesirable systematic errors. A big part of that is understanding how the collimation system works from the LEDs to the fused quartz window. Simple ray tracing simulations were performed to study the incident beam profile. The incident flux is not directly obtained from these simulations, but it was instead measured directly by placing the PMT in front of the light beam with the 1.5" cap removed (detailed in chapter 5.4). Nonetheless, understanding the photon flux profile is of great relevance.

Figure 4.10 illustrates the positioning of the LEDs in the PCB matrix in the XOZ plane, the y axis giving the direction of propagation of the collimation system. From the previous section, we have roughly three different viewing half-angles to simulate: 60° (the SMD LEDs 1,4,6 and 7), 13° (the 405 nm DIP LED, number 2) and 30° (the remaining two DIP LEDs, 3 and 6). In terms of positioning in the matrix, because of azimuthal geometry, only two positions need to be simulated: one for the SMD LEDs at (2.55, 0, 0) mm and another for the DIP LEDs at (7, 0, 0) mm which will, additionally, be tilted towards the centre of the diffuser at (0, 50, 0) mm.

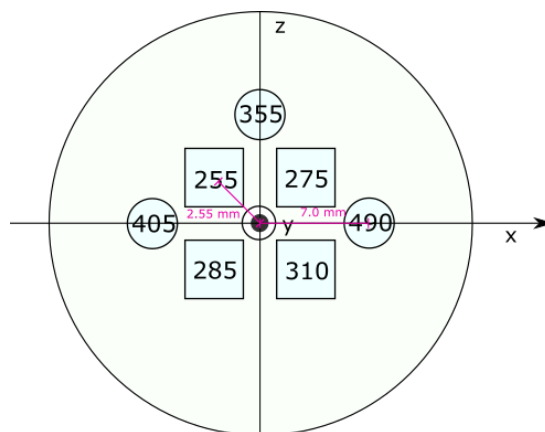


Figure 4.10: The geometric positioning of the LEDs in the PCB Matrix and reference axes used in simulations.

These simulations were coded in the Python programming language. A generic, non-geometry dependent class, *ledObject* serves as the basis of the simulations. It generates n photons in the $(0, \hat{e}_y, 0)$ direction and then applies a random rotation based on a given probability distribution function. It computes the correct tilt angle to have the LEDs

pointing towards a given point, and computes the effect of a Gaussian profile diffuser with a given half-angle. Finally, it propagates the photons across a system with two pinholes that can be at varying distances and with varying openings. It does not include reflections in the interior of the tube nor at the diffuser.

The simulations were run with the following configurations:

- a. the distance between LED matrix and diffuser set to 50 mm;
- b. the Gaussian distribution function of the diffuser with viewing half-angle (FWHM) of 7.5° ;
- c. the distance from diffuser to the first collimator set to 15 mm;
- d. the distance between collimators set to 138 mm;
- e. the distance from the second collimator to the fused quartz window set to 58 mm;
- f. the distance from the fused quartz window to the Spectralon® pinhole set to 20 mm.

The collimation system reduces the solid angle of the beam greatly, resulting in a small fraction of photons at the end of the two pinholes. To have good statistics, a total of 40×10^6 photons were simulated for each LED. The following three LED configurations were simulated:

1. SMD LED with 60° half viewing angle at (2.55, 0, 0) mm;
2. DIP LED with 13° half viewing angle at (7, 0, 0) mm tilted with a 8° yaw angle towards the centre of the diffuser;
3. DIP LED with 30° half viewing angle at (7, 0, 0) mm tilted with a 8° yaw angle towards the centre of the diffuser.

The LEDs angular distribution functions were simulated with a Gaussian function with the respective half viewing angle. Even if the real angular distribution is closer to a parabolic distribution, it can be well approximated by a Gaussian function due to the diffuser's effect. The plot in figure 4.11 shows the angular profiles for each simulated LED after the diffuser effect. It is possible to see that the profiles are close matching due to the effect of the diffuser. The shown angle is the polar angle with respect to the y propagation axis.

After propagating the photons through the system and removing the photons that don't get through the pinholes, the polar angle with respect to the propagation direction gets much smaller, as seen in figure 4.12. This is another important objective of the collimation system, to have all beam profiles look roughly the same after the collimation system. Table 4.2 shows the fraction of photons, in percentage, that go through both pinholes in the simulations performed for each LED configuration.

Figure 4.13 shows the spot photon distribution (x,z) at the input Spectralon® pinhole input at $y = 279$ mm. The photons are distributed within a circle of 2 mm diameter centred around 0. That means all photons should go through the Spectralon pinhole, since it has an internal diameter of 5 mm, and there should be no backscattering at the entrance to the sphere, as desired. The SMD LED polar angle distribution isn't as smooth as the others due to the lower number of statistics.

This concludes the propagation of photons inside the collimation system. Next we will discuss the simulations with ANTS2 of the propagation of photons inside the TIS.

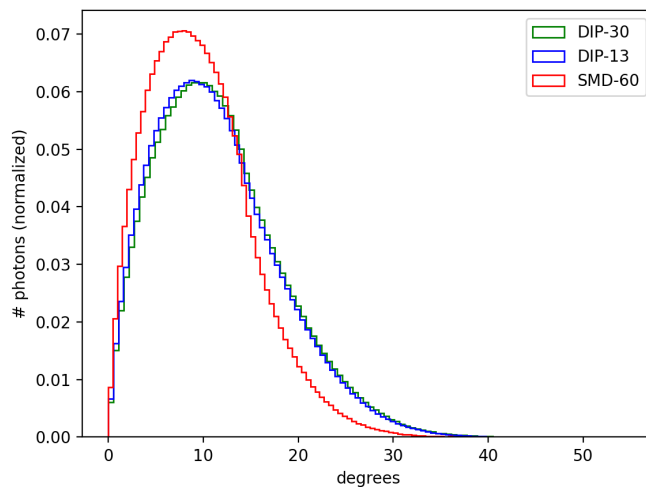


Figure 4.11: Polar angle distributions with respect to the direction of propagation after the diffuser. The histogram is not centred around 0 due to an effect of the solid angle, proportional to $\sin \theta$.

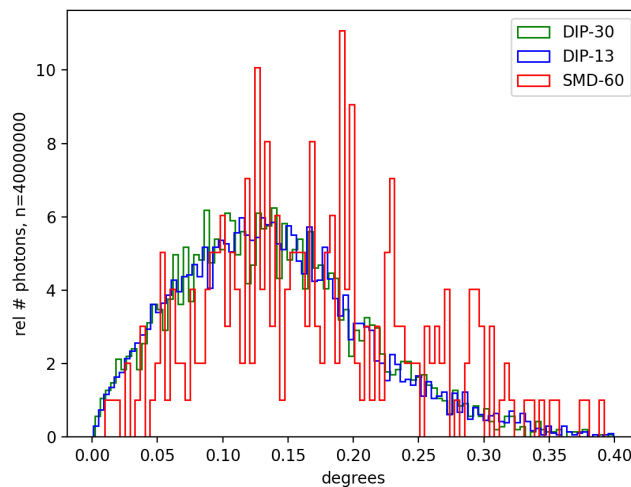


Figure 4.12: Polar angle distributions with respect to the direction of propagation after the two pinholes. Histograms are normalised for each LED for comparison.

Table 4.2: Fraction of photons through both pinholes for each LED configuration

LED	% of photons through
SMD LED, 60° half-angle	$6.5 \times 10^{-4} \pm 4.03 \times 10^{-5}$
DIP LED, 13° half-angle	$2.03 \times 10^{-2} \pm 2.25 \times 10^{-4}$
DIP LED, 30° half-angle	$8.87 \times 10^{-3} \pm 1.49 \times 10^{-4}$

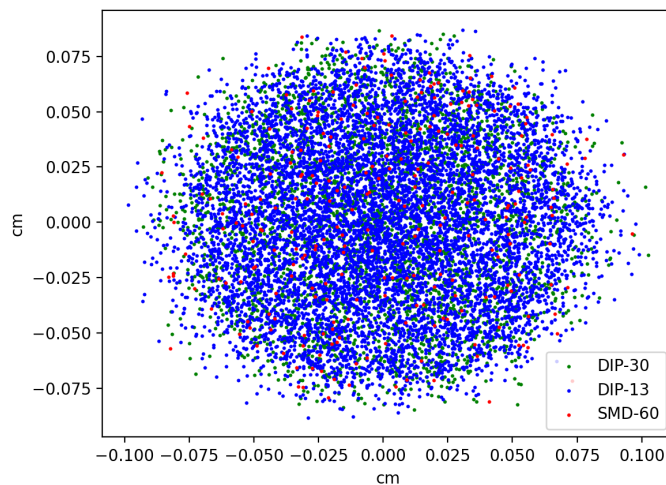


Figure 4.13: Scatter plot of the photon (x,z) "spot" distribution on the plane of the Spectralon® pinhole at $y = 279$ mm.

4.5 Photon Propagation Inside the Total Integrating Sphere

Simulations of the core of the experiment, the TIS and detection systems, were made with the ANTS2 software package. The core simulation module of ANTS2 is based on the TGeoManager class of the ROOT package from CERN [94], which stores and displays the simulated geometry allowing for 3D navigation. The software is capable of simulating particle and photon sources, primary and secondary scintillation photons as well as performing particle tracking, photon tracing and generating responses in photosensors. It also includes a reconstruction module with built-in GPU based implementations [30]. The software has a graphical user interface implemented with the QT framework.

There are two simulation modes in the software: particle and photon source. In our case a photon source was used, from point $(0, -43 \text{ mm}, 0)$ just behind the input pinhole in the y direction (normal incidence). Since the angle of the photons entering the sphere is close to zero (see section 4.4.1), this a good approximation. Each photon is traced according to the photon tracing cycle employed by ANTS2 [30]:

- position where the photon intersects the next material interface is computed;
- generates a random Rayleigh and absorption distance based on the respective mean free paths (average distance without an interaction) for the material in question;
- if the shortest of the two is within the distance, the photon is eliminated in the case of absorption, or, in the case of Rayleigh scattering, a new photon is generated with a new direction;
- at the interface with the different material, the interaction is computed according to the selected interaction for the interface in question. If no custom module is selected, the usual Fresnel equations are used to compute whether the photon gets reflected or refracted;
- for a given photon, the process stops if the photon is absorbed, detected or leaves

the geometry. Additionally, there's a setting to define the maximum number of allowed cycles to avoid infinite loops in the simulation.

The probability of a photon to be detected when it strikes the photosensor interface is [30]:

$$P_{det} = q(\lambda)P_t(\theta)P_A(x, y), \quad (4.7)$$

where $q(\lambda)$ is the quantum efficiency, or ratio of photoelectrons emitted to the number of incident photons of the photodetector. $P_t(\theta)$ is the angular dependence of detection probability and $P_A(x, y)$ the relative position detection probability dependence. Quantum efficiency is only relevant for absolute measurements; for relative ones, like gas vs. liquid interface, it cancels out. The angular dependency for the photocathode is not known. The detector area was taken to have the size of the active photosensitive area (15 mm diameter) and the surrounding area is made up of a totally absorbing material. The software has the option of simulating the signal from the photosensor, but, by default it outputs the number of photon counts. Since we use the PMT in photon counting mode, this was the mode of detection used in the simulations.

The 3D geometry is managed by the TGeoManager class of the ROOT package [94], including visualisation of the geometry and positioning of the objects and finding the next interface in photon tracing. The geometry of the experiment needs only to be as complex as needed to describe the relevant optical interfaces. In this case (figure 4.14), the geometry was built using primary forms from the TGeoManager class (spheres and cylinders) and logical associations between them.

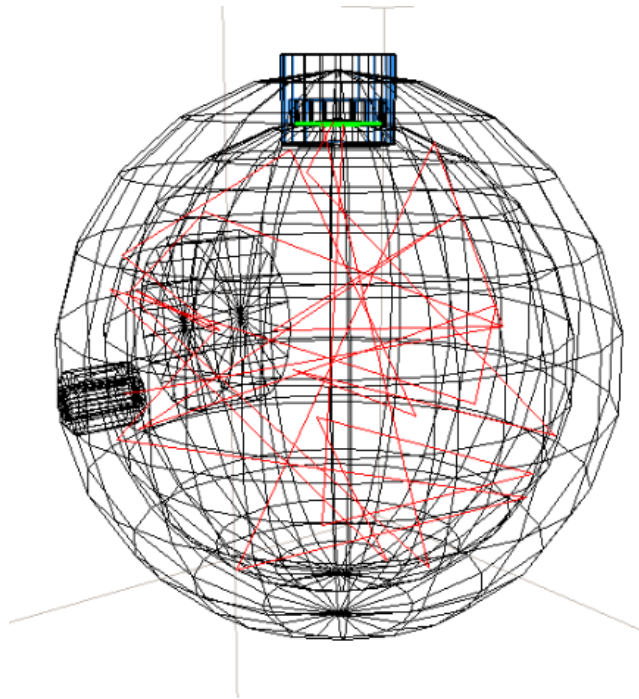


Figure 4.14: Geometry of the experiment implemented in ANTS2 as seen in the geometry visualisation window in the ANTS2 graphical user interface. The red lines show the optical path of a photon with multiple reflections before being detected.

Figure 4.14 shows the geometry built in ANTS2. There's an outer hollow sphere internal diameter of 83.82 mm (3.3") and an external diameter of 100 mm, making up the diffuse reflecting surface of the TIS. An inner sphere which is the filling medium,

either air or one of the liquids. The 180° degree port of the real TIS is represented simply by a 5 mm diameter cylindrical opening in the sphere, surrounded by a generic absorbing material representing the light trap. Note that the collimation system is not simulated as it is expected that photons that go back through the pinhole are absorbed. Future simulation work might quantify with more precision the effect of the input pinhole and light trap. Nonetheless, the photons are generated already at the Spectralon® pinhole before entering the sphere. On the top there is the cylindrical opening for the detector port, where the photodetector sits.

Each object in the geometry needs to have an associated material. There's an internal library of materials, or, alternatively, materials can be defined by the user. Table 4.3 summarises the list of materials used in the simulations performed, displaying the same units as those used in ANTS2. The wavelength-dependent values shown in table 4.3 refer to 405 nm. The Rayleigh scattering mean free path in the air was computed from the cross section values of table 1, computed by Bates in [95].

Table 4.3: Materials definitions in ANTS2, for 255 nm and 405 nm[*]

	λ [nm]	n	Absorption [mm ⁻¹]	Rayleigh mfp [m]	Usage
Air	405	1	0	22231	Inner sphere and input cylinder
	255	1	0	3470	
Water	405	1.339	0.53×10^{-5}	221	Inner sphere and input cylinder
	255	1.3604	7.5×10^{-5}	31	
Spectralon		1.35	0	NA	Outer sphere
Quartz	405	1.470	0	NA	PMT window material
	255	1.505	0	NA	
Absorber		1	0	NA	Surrounding input pinhole (light trap)

* If not indicated, values are constant for all wavelengths;

In the case of water, the absorption length values from 380—500 nm were taken from [96], the water used was reagent grade Type I (the purest reagent water standard). For 250–320 nm, the values were taken from [97], using purified water by ion exchange and four subsequent distillations. Neither article has information for the 355 nm wavelength, so in this instance the value was taken from [98], which refers to natural waters. A multiplying factor was estimated to fit the value to the data from the pure water observations. The water we used in our experimental runs was pure water Type II from José Manuel Gomes dos Santos, Lda. The Type I and Type II (Type I is the purest) water identifications are defined in the Standard Specification for Reagent Water from the American Society for Testing and Materials (ASTM) [29].

The Rayleigh scattering in water was computed with the cross section equation for molecules [99]:

$$\sigma_R = \frac{16\pi^5}{3} \frac{\alpha_m^2}{\lambda^4}, \quad (4.8)$$

where α_m is the mean polarizability given by the Lorentz-Lorenz equation [100]:

$$\frac{n^2 - 1}{n^2 + 2} = \frac{4\pi}{3} N\alpha_m, \quad (4.9)$$

where n is the refractive index of the medium and N the number of molecules per unit volume.

The refractive index for Spectralon® was taken from Labsphere’s technical guide and, since no wavelength dependent information is available, is kept constant at a value of 1.35 [101]. The refractive indices for water and fused quartz were consulted in the Refractive Index Database website [102]. The values consulted come from experimental measurements detailed in [103], for water, and [104], for fused quartz. The absorption length for fused quartz was taken to be 0 since it is only used for the detector window with a very small thickness, solely to account for the optical interface (Fresnel laws).

The absorber material has the optical interface configured for 100% absorption for all interfaces. The Air-Spectralon and Water-Spectralon optical interfaces are either computed by the Lambert model or the implementation of the Wolff and Oren-Nayar model discussed in section 3.5. The remaining interface with the detector window is described by the usual Fresnel equations.

This comprehensive simulation of the experiment was used to analyse the experimental data obtained. It allowed us to test how well the Lambert and modified Wolff models reproduce the experimental data and the relative roles of specular and diffuse reflectance when the interface changes from gas to liquid.

4.5.1 Photon Optical Path Length in the TIS

In this work, since part of the measurements are to be done with liquids, special attention was paid when selecting the sphere diameter, due to its impact on the average length travelled by photons. While integrating power is desirable, if the selected TIS is too big, the absorption length of the liquids can become dominant.

Using ANTS2 to simulate the TIS geometry as described above, the photon optical path length was investigated. For these simulations, a non-absorbing medium was simulated, so photons are only optically absorbed at the walls of the sphere, simulated with the classical Lambertian reflection. For a Lambertian albedo of $\rho_l = 0.92$, 99.5% of the photons would travel a distance below ~ 13 m. For $\rho_l = 0.99$, 99.5% of the photons would travel a distance below 20 m. The top panel of figure 4.15 shows how the average distance travelled by photons varies with the Lambertian albedo.

Meanwhile, in the case of pure water, at 405 nm an absorption length value of 188.7 m was measured by Pope et al. [96], and for 255 nm a value of 13.3 m was reported by Quickenden et al. [97]. The bottom panel of figure 4.15 shows the absorption length values (in meters) for pure water taken from the literature and used for simulating the water interface in this work. Given the distances travelled by the photons and the typical absorption length values for pure water, it is clear that photon absorption should not affect the measurements significantly, but it is still necessary to take it into account during the analysis, especially for the smaller wavelengths.

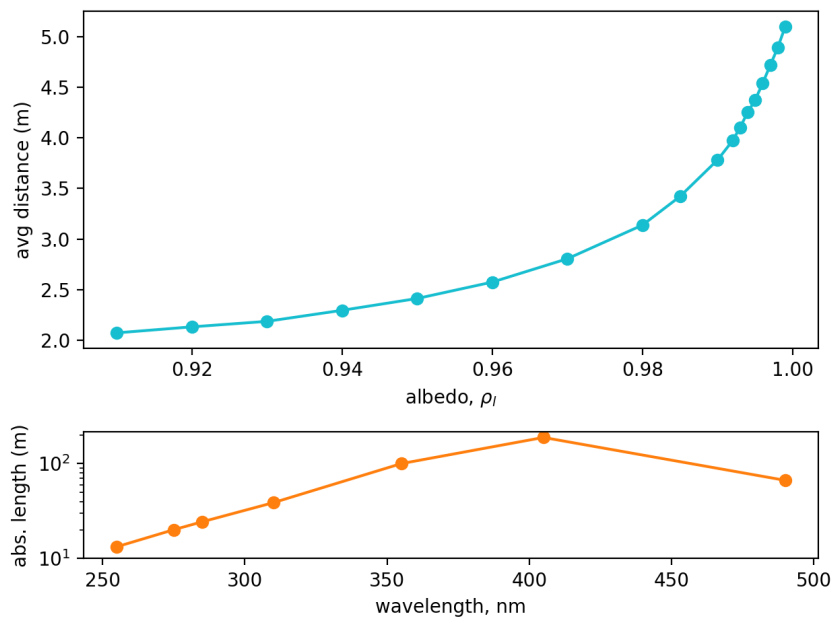


Figure 4.15: Top panel shows the average distance travelled by detected photons in a non-absorbing medium for increasing Lambertian albedo (simulated for the TIS geometry in ANTS2). Bottom panel shows the absorption length values for pure water taken from literature [96, 97, 98].

Chapter 5

Measuring Reflectance in a Liquid Interface

This chapter details how the experimental set-up that we developed (chapter 4) was used to measure the diffuse reflectance in a liquid-PTFE interface.

It starts by describing the experiment control system, that was developed to facilitate the operation of the experiment. This includes LED control, atmospheric sensor monitoring and a pump to fill and empty the sphere with liquids. Next, the PMT signal and data acquisition systems are discussed in detail, analysing dark count noise and possible sources of non-linearity in photon counting mode (e.g. photon pile-up).

Afterwards, the complete scheme for taking measurements is described in detail. A discussion follows on possible sources of systematic errors and how to avoid or account for them. Next a description of the experimental measures performed is given, both for the incident flux and for the flux in the TIS after multiple reflections. The chapter ends with the description of a future iteration of the system to measure continuously the incident flux while taking reflectance data.

5.1 Experiment Control

The experiment control consists of the following components: (a) LED control system, for switching on and off and tuning the input current; (b) pump system, to fill and empty the sphere with liquid; (c) sensor readout, for reading out temperature and pressure inside the optical chamber.

The LED control system consists of an Arduino Uno micro-controller board equipped with a custom made shield for the Arduino (figure 5.1, the schematic for the PCB is shown in figure 5.2). It permits to control the current flowing through one of the LEDs in the LED matrix, one LED at a time. This was achieved using the AD5293 digital potentiometer from Analog Devices with a resistance range between 0 and 20 k Ω . The current limiting resistors in series with the digital potentiometer were made hot-swappable to make it easier to switch between LEDs with different current ratings. The Arduino controls the digital potentiometer via Serial Peripheral Interface (SPI) [105].

The board uses two 6-channel open collector buffers to switch between the LEDs and making sure only one LED is on at any time. Even though only 7 LEDs are being switched, some buffer channels are wired together to allow for higher current loads. The buffers isolate the Arduino from the LED power system, and allow for sourcing the current to each LED individually. A decoder is used to set the logic for the 7 channels using just

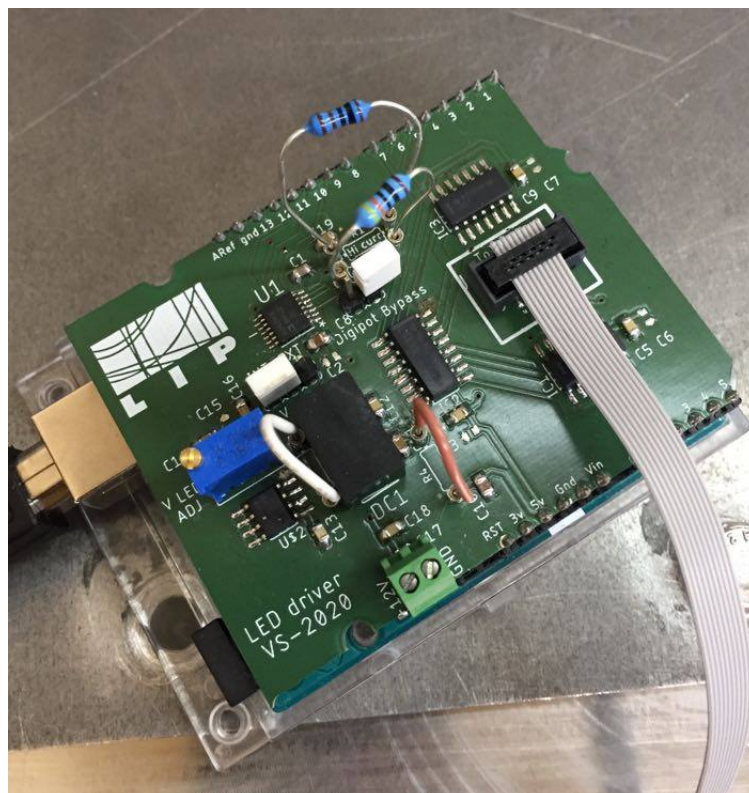


Figure 5.1: Photo of the Arduino shield for controlling the LEDs. The axial through-hole resistors are switched depending on the LEDs being used.

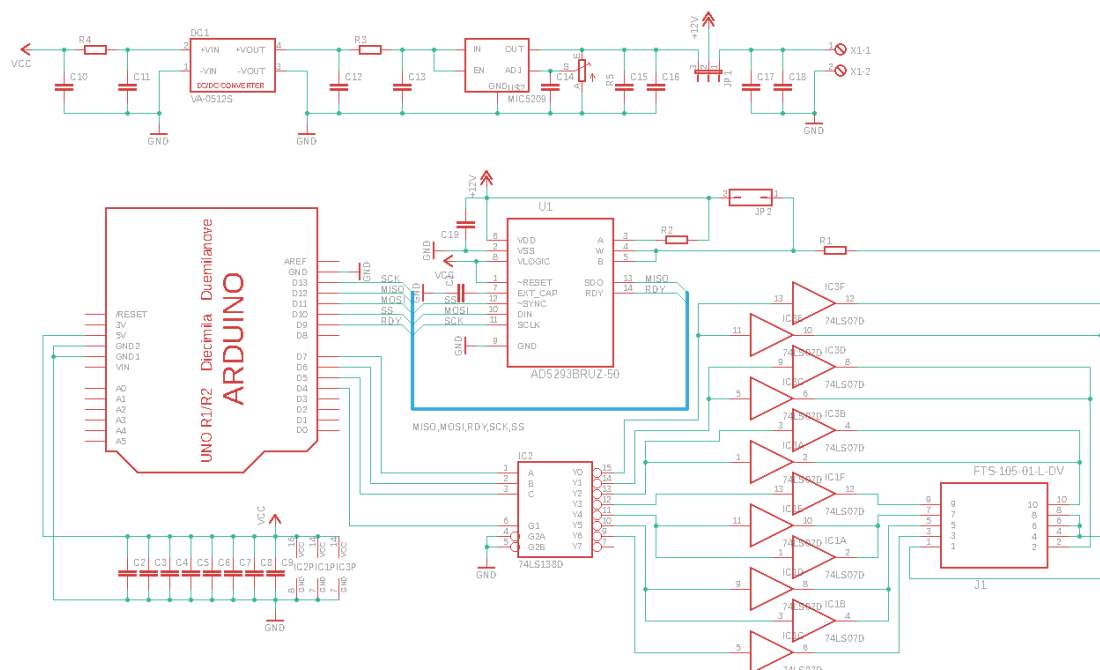


Figure 5.2: Schematic of the LED shield: the encoder output is connected to the input of the buffer channels, which are shown individually instead of a monolithic IC view, for clarity. Some of the buffer channels are wired together to allow for a higher current load.

combinations of three logic signals from the Arduino, freeing up the remaining output pins. Additionally, it guarantees only just one LED is on at any time. The board has a step-up DC/DC converter to feed 12V to the LEDs, but it can also be fed from an external power source, if deemed necessary.

A second Arduino Uno is used, along with a commercially available motor control shield, to control a small peristaltic pump to fill and empty the sphere. Using the pump, it is possible to fill the sphere in place, as removing it from its place to fill it can potentially introduce systematic errors. Additionally, it was observed that the uniform constant fill of the pump is better to avoid air bubble formation as opposed to filling manually, directly from the recipient.

Finally, an Arduino Mega is used to readout multiple pressure, temperature and humidity sensors. For this experiment, the relevant one is temperature, mainly due to its impact on the refractive index of materials and ultimately on reflectivity itself [106, 18].

Each Arduino can be monitored and controlled from the serial port using a set of custom commands developed for that effect. Table 5.1 has a list of the relevant Arduino commands implemented. All three Arduinos are powered from a USB hub which connects via USB to an ODROID single-board computer.

Table 5.1: Arduino commands for experiment control

Arduino	Command	function
LED ctrl (Uno)	<i>potenable</i>	enable writing to potentiometer
LED ctrl (Uno)	<i>pot xxxx</i>	set dynamic resistor value (10 byte, 0–1023)
LED ctrl (Uno)	<i>on x</i>	turn on LED x (1–7)
LED ctrl (Uno)	<i>off</i>	turn off LEDs
Pump ctrl (Uno)	<i>-xxx</i>	sets pump speed to xxx value (8 byte, 0–255)
Pump ctrl (Uno)	<i>fill</i>	turns on pump (filling direction)
Pump ctrl (Uno)	<i>empty</i>	turns on pup (emptying direction)
Sensors (Mega)	<i>x</i>	0 — 5, each value maps to temperature, pressure and altitude from BMP280 & BMP288
Sensors (Mega)	<i>mcpt</i>	temperature from MCP9808

5.2 Photodetection and Data Acquisition

For photodetection, the PMT R762P from Hamamatsu® with a bialkali photocathode was used. This PMT has a relatively small photocathode, 15 mm diameter, and a short pulse rise time, ~ 3 ns, making it ideal for photon counting. The PMT quantum efficiency, the ratio of emitted photoelectrons to the number of incident photons, has the maximum of 23.8% quantum efficiency at 380 nm. The PMT has a relatively low dark current, i.e the electric current generated on the PMT in the absence of any incoming photons, typically amounting to 45 ± 7 dark counts per second with the set-up we used.

For this experiment, the PMT was used in photon counting mode. Due to very high avalanche gain, PMTs are capable of detecting single photons. At very low light fluxes, photon pulses become separated in time enough to be counted by sufficiently fast electronics [107]. When operating in photon counting mode, the number of pulses is recorded irrespective of the pulse height (above a certain threshold value). A low-level discriminator (LLD) is used so that when the signal is above a certain threshold, the pulse is counted. The use of the LLD removes low amplitude dark current signal, improving the signal to noise ratio. Another advantage of photon counting over the analog mode is that it has more operating stability since the output counts are very resistant to variations in the supply voltage and PMT gain [107]. Because we are interested in having a very high sensitivity to reflectance changes, photon counting is the ideal mode of operation.

The set-up for counting photons used is depicted in the schematic 5.3. The PMT signal is fed to a linear amplifier. Figure 5.4 shows a typical single photoelectron pulse signal from the PMT after amplification. Next, the signal goes to the LLD, model 623B from LeCroy. The discriminator window was set to 15 ns. The threshold was set at the single photoelectron amplitude, too far above this value and almost no counts are observed, too far below and the counts get overwhelmed by the low amplitude dark current. The signal from the discriminator then goes both to a preset counter-timer (model N145) from Caen and to a TRB3 acquisition board. A two-fold high-voltage power supply from Caen was used the power PMT. All the electronic modules, except for the TRB3 board, sit in a Nuclear Instruments Model (NIM) crate.

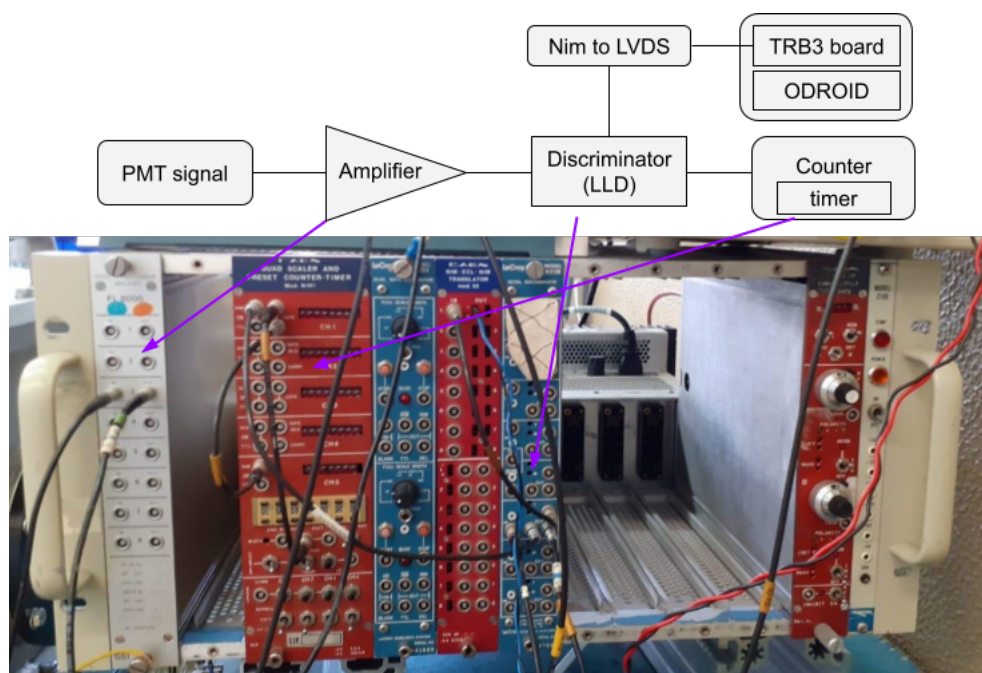


Figure 5.3: Diagram and photo of the electronic set-up for photon counting with the PMT.

The PMT is positively biased, at 1400V. Figure 5.5 shows a schematic of the voltage divider base used to feed the PMT. In some applications, a negative high voltage polarity might be used, by grounding the anode and applying the negative high voltage to the cathode [108]. Since we also wish to make measurements in water, the negatively charged cathode could create high levels of noise from possible discharges from the PMT contact with the water. For that reason, a positive polarity is the best option for our case.

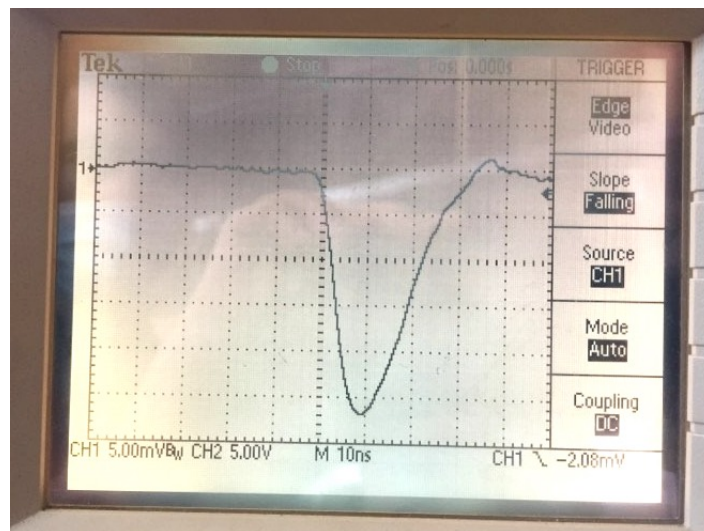


Figure 5.4: Photo of a typical photon pulse signal after amplification as seen on the oscilloscope.

The TRB3 acquisition board in use was borrowed from LIP's RPC group: an FPGA based, Time-to-Digital Converter [109]. These boards are in widespread use in nuclear and particle physics instrumentation, especially with Resistive Plate Chambers (RPC) [110]. It is controlled through an ODROID computer module where the Central Trigger System, event builder and web interface are hosted. The signal from the discriminator is fed through a NIM to LVDS (low-voltage differential signalling) converter and then to the TRB3 board. The acquisition is made in pulser mode, with the period set to $100 \mu s$. This means that the times of detected counts are saved to disk in uninterrupted windows of $100 \mu s$. The saved time-stamps are relative to Tref, the time of saving to disk since the beginning of the acquisition. With this information, the times of detected counts from the beginning of acquisition can be reconstructed. It is important to save the measured signals to disk, so a more detailed analysis can be made when necessary.

Dark counts in the air interface were observed to be typically around 45 ± 7 cps, which is various order of magnitude smaller than the photon fluxes during measurements (see for example figure 5.7). This value can be higher if the PMT isn't kept away in the dark. Additionally, dark counts with the sphere filled with water were seen to be significantly higher, as much as 128 ± 11 cps. The dark counts were measured again, with the sphere half-filled with water, giving 106 ± 10 cps. In another instance, the dark counts with the sphere filled with water were 104 ± 10 cps, and after drying out the PMT window and re-measuring the dark counts with an air buffer below the PMT window, a value of 99 ± 10 cps was found. These observations seem to indicate that the increase in counts should be due to some external source interacting with the water. One possibility is Cherenkov light from crossing atmospheric muons (produced in the upper atmosphere by cosmic rays). Crossing muons at the Pierre Auger observatory were seen to result in a signal dependent on the level of water [111]. Given the size of the sphere, the cosmic muon rate through the sphere should be no more than a couple of Hz, so it is unlikely that it explains the totality of the increase in dark counts. Other possible sources of the observed signal might be radioactivity from ^{40}K from the materials in the set-up or Radon in water. Relativistic electrons from beta decay or γ ray interactions with the water could give rise to Cherenkov photons. Despite these considerations, the dark count

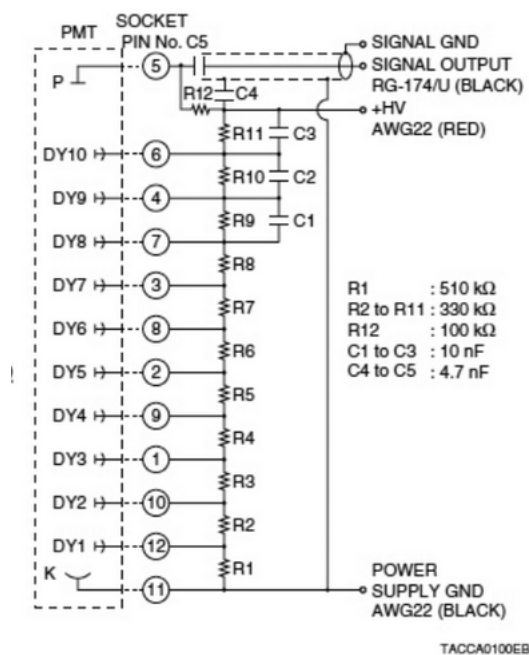


Figure 5.5: Schematic of the voltage divider base used with the R762P PMT from Hamamatsu®

rate is very small compared to the photon fluxes in question, so taking dark count control measurements during data taking is enough to consider its effect during data analysis.

5.2.1 Probability of Pulse Overlapping (Photon Pile-Up)

Besides the PMT's own time response, derived from its electron emission and multiplication process, the other electronic modules also add to the time it takes to resolve a single photoelectron pulse. The amplifier has its own time constant (~ 20 ns FWHM, fig. 5.4) and the discriminator a time window resolution (15 ns). It can happen that two photons arriving within a small enough interval of time will be counted as one. This is called photon pile-up and is especially relevant for higher fluxes of photons.

So, in practice, the measured count rate m will underestimate the true number of counts, n , because some pulses will be too close to each other to be resolved by the PMT and associated electronics. This relation can, to a first approximation, be given by [112]:

$$n = \frac{m}{1 - m\tau}, \quad (5.1)$$

where τ is the dead time of the entire acquisition system, the minimum delay between two resolved photons. In our case, photon fluxes being measured are moderately high so it is important to understand the pile-up effect. To that end, it is crucial to know the dead time of the system. Taking the signal of the PMT acquired with the TRB3 board and plotting (figure 5.6) the time difference between two consecutive photons, a lower limit peak of 45 ns can be seen. Since both the time window and amplifier response time are significantly below this value, the TRB3 acquisition board should be the limiting component. It should be noted here that measurements were taken with pre-set counter and the TRB3 board in tandem. The measured counts with both methods were in good

agreement. Thus, the value of 45 ns was selected as the dead time of the entire acquisition system.

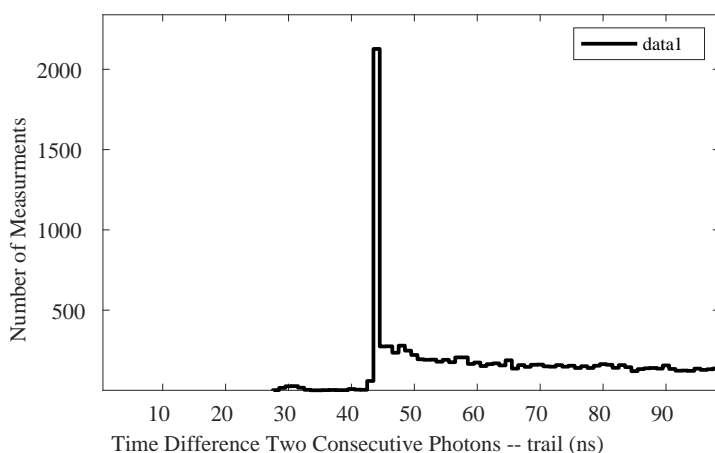


Figure 5.6: Example plot of time-stamp difference between two consecutive photons in ns. Example signal acquired with the PMT on top of the sphere with LED 255 nm on.

Figure 5.7 shows the expected number of observed counts per second as a function of the real counts per second, assuming $\tau = 45$ ns. The maximum and minimum fluxes with the PMT aligned in front of the collimation system are also plotted for reference. For the LED 490 nm, there's a deviation of 5.56%, so correcting the value is necessary. During data taking, measurements were made in two modes of operation (see 5.3), high and low current, to mitigate possible uncertainties due to photon pile-up.

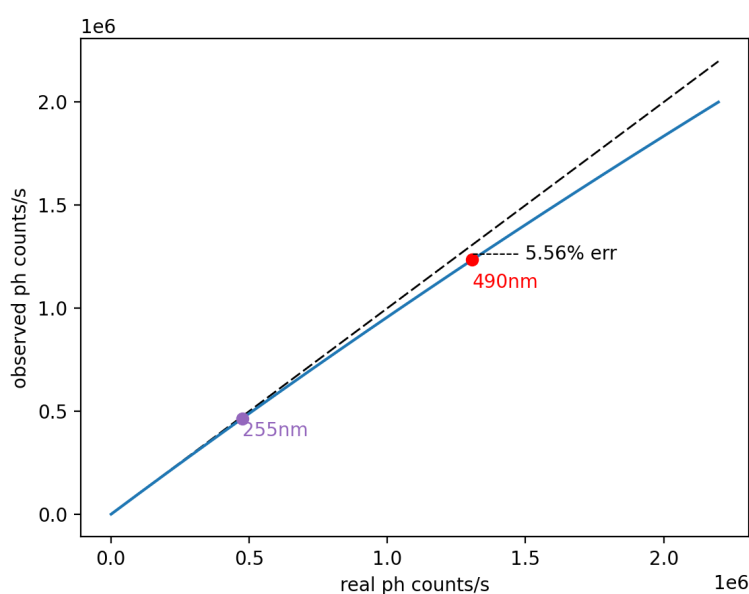


Figure 5.7: The dependence of the rate of observed photons on the true rate of photons.

5.3 Measuring the Reflectance of the TIS

This section describes the methodology to measure the photon flux inside the TIS after multiple reflections. The operating current for each LED should not be too low, so that dark counts become dominant, and it should not be too high so that photon pile-up begins to cause high non-linearity. Respecting the two previous points, two operating modes for each LED were configured, one for higher current/higher counts and another with lower current/lower counts. No low count mode was configured for LED 355 nm since it would need a different set of DIP resistors just for it. The use of these two modes helps to take into account possible photon pile-up non-linearities. It also helps to reduce possible systematic errors related with variations in the sourced current or instabilities of photon emission of the LEDs.

Additionally, the LED fluxes were also adjusted so that the observed flux in the air interface was similar between all SMD LEDs and between all DIP LEDs, respectively. It was not possible to have the same flux for both the SMD and DIP LEDs due to the very different power ratings. The advantage of this is that the difference in the count rate increase in the liquid interface for the different wavelengths becomes apparent right away when taking measurements.

Table 5.2 summarises the resistor configuration for each LED used in data taking; note that while the digital potentiometer is set from the ODROID computer, R1 and R2 need to be switched manually. The current for the LEDs was calculated from Ohm's law from the voltage measurement at the terminals of R1. The voltage V_{R1} was always monitored during data taking so that the stability of the current to the LEDs could be measured. The uncertainties in the measurements of the voltage and R1 were propagated to the computation of current. The uncertainty in R1 was taken to be the voltmeter's uncertainty in the last digit of the measurement.

The measurements were made first with the air-filled sphere and then with the water-filled sphere. The sphere is installed inside the light-tight chamber. The measurement procedure was the following:

- a dark count control measurement is taken;
- for each LED, data is taken first in high count mode and then in low count mode;
- another dark count control measurement is taken before powering off the PMT and opening the chamber;
- the PMT is removed and the sphere is filled with ultra-pure water from the top with the peristaltic pump, until the liquid comes out through the evacuation tube (section 4.3.1);
- the PMT is inserted back again, ensuring the tube is filled with extra water, indicating the PMT window is appropriately submerged;
- another dark count control measurement is taken, now in the water-filled sphere;
- for each LED, data is taken again, first in high count mode, and then in low count mode;
- a final dark count control measurement is taken.

Measurements with ethanol were also attempted. The data, however, wasn't used for analysis because there were issues with air bubbles that formed presumably in the area of the light trap and also near the PMT window. We believe this happens because ethanol

Table 5.2: LED configuration used in data taking.

LED	R1 (k Ω)	R2 (k Ω)	Digi Pot (k Ω)	Current (mA)
#1 255 nm	0.999	0.429	0.02	3.992 ± 0.009
(low counts)	0.999	0.429	2.813	1.593 ± 0.0025
#4 275 nm	0.999	0.429	2.423	1.771 ± 0.003
(low counts)	0.999	0.429	12.97	0.506 ± 0.001
#7 285 nm	0.999	0.429	2.031	2.048 ± 0.0029
(low counts)	0.999	0.429	7.891	0.791 ± 0.001
#5 310 nm	0.999	0.429	5.726	0.999 ± 0.001
(low counts)	0.999	0.429	19.98	0.356 ± 0.001
#6 355 nm*	0.999	0.429	19.98	0.40 ± 0.0027
#2 405 nm	269	160	19.98	$2.01 \pm 0.01 \times 10^{-2}$
(low counts)	530	230	19.98	$1.05 \pm 0.12 \times 10^{-2}$
#3 490 nm	269	160	19.98	$2.10 \pm 0.01 \times 10^{-2}$
(low counts)	530	230	19.98	$1.10 \pm 0.12 \times 10^{-2}$

* LED #6 355 nm has no low counts configuration, since it would need a different set of DIP resistors just for it;

has a smaller surface tension than water, and the evacuation canals at the top and at the light trap do not work as well as they do with water. The new iterated pieces currently being worked on at the workshop already address these issues, so this should be fixed in the future iteration of the system (sections 4.3.1 and 4.3.2).

Considerable efforts were made to minimise systematic errors that can affect the measured values largely. Possible sources of systematic errors are: (a) changes to the geometry of any part of the experimental set-up; (b) dust particles or any source of dirt in the interior of the sphere or input fused quartz window; (c) air bubbles when taking data with liquids.

The system and the procedure for taking data were designed to minimise any physical intervention with the system, so the geometry is kept exactly the same. The LEDs can be switched on and off, and their power varied without any interference to the set-up. The sphere can also be filled with minimum intervention. It is only necessary to remove the PMT, which is always mounted in the same position thanks to the plate cages system.

When working with total integrating spheres with high reflectance, dust particles can be a concerning source of systematic errors [28]. Dust particles affect the reflectance factor of the TIS, which is highly sensitive to reflectance changes. The input quartz window also needs to be kept clean at all times. To take these into account, special attention needs to be taken to cleanliness when dealing with the TIS and peripherals (using gloves and covering the hair). Compressed air was also used to clean the sphere after assembling everything. When the sphere wasn't installed in the optical chamber, it was kept in a clean room with all openings covered by aluminium foil. Additionally, the optical chamber was kept in an argon atmosphere to prevent dust accumulation in

the surfaces of interest. Plastics are more permeable to heavier gases, so the diffusion of argon in the PTFE can also aid in removing contaminants [113].

Regarding air bubbles, as discussed previously, several tests were made to guarantee no air bubbles are left in the TIS after it is filled with water. Finally, the measurements were repeated several times over a few weeks. If the data is consistent across those runs, we can conclude there wasn't any significant effect from any of these possible sources of systematic errors.

5.4 Measuring the input flux

The PMT was installed horizontally through the 0° (1.5") port to measure the input flux of photon influx, as seen in figure 5.8. The main difficulties with this measurement are (1) to ensure that all input light falls upon the PMT's photocathode and (2) that the light reflected in the PMT window does not add up as an additional contribution to the input flux.

The first one was addressed by taking measurements at two different distances from the input pinhole. The first distance, d_1 , is equal to 83.3 ± 0.1 mm, which corresponds to the distance from the Spectralon® input pinhole to the plane of the first reflection on the 0° port. The distance d_2 is closer, 45.9 ± 0.1 mm, to the input pinhole. If all input light is falling upon the PMT window, then the flux measured at distance d_1 will be equal to measurement at the shorter distance d_2 .

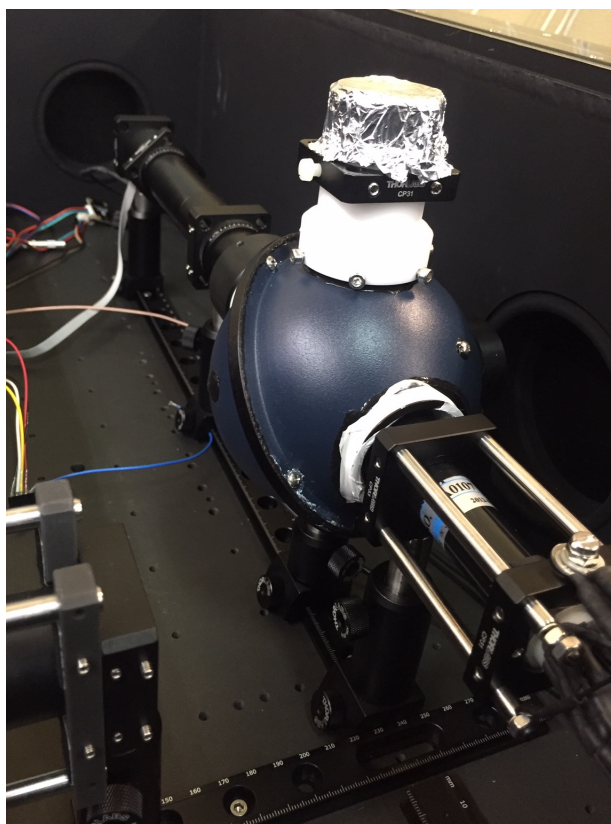


Figure 5.8: Set-up for measuring the input flux of photons, the PMT is installed horizontally on the 0° (1.5") port. Photo was taken with the optical chamber open. Measurements are of course done with the chamber closed, in the dark.

The second one by using a black tube from the input pinhole to the PMT window to absorb any photons specularly reflected from the surface of the PMT window, to stop them from eventually being reflected back onto the PMT window. The black tube has a total length of 118 mm and a diameter of 1 in being threaded to an SM1 plate cage. The end of the tube has black pinhole installed to cover the Spectralon® surface of the input pinhole. This is important to remove reflections from that surface. Both the pinhole and black tube are anodised aluminium, for which specular reflection should be at most 5% [114]. In turn, the fraction of reflected photons on the PMT window should amount at most to $\sim 4\%$ for the 255 nm LED, for which the quartz window has the highest refractive index. Thus, the superior limit on the probability of light returning to the PMT after being reflected off the its window is 0.2%. This is the probability of double reflection, first on the PMT window and then on the aluminium pinhole back to the PMT.

A custom made plastic POM ring threads into the same cage to reduce the tube's inner diameter to that of the external diameter of PMT (19.7 mm). The PMT can slide through the system and be fixed into different positions by screwing the positioning rods that attach to the cage plates.

For each LED configuration (table 4.1), measurements are made, first, with the PMT set at distance d_1 , 83.3 mm away from the input pinhole. Afterwards, the PMT is powered off and moved to distance d_2 , 45.9 mm away from the input pinhole, by adjusting the position of the positioning rods (figure 5.8), and the procedure is repeated. Dark count control measurements are made at the start and end of the procedure.

This set-up does not allow for taking measurements in a liquid interface, but we have designed a new piece that will allow us to do this. It comprises two parts, a port adaptor similar to the one used in the north pole port to support the PMT and a black tube similar to the one used for the input flux measurements described above. The black tube will run the length of the sphere, and have diagonal slits above and below to allow for liquid to fill it, without adding any significant optical uncertainty. The port adaptor piece will be similar to the top PMT support piece but having to fit to the 1.5" port. A crucial aspect of this piece that it will allow to position the PMT at different distances from the Spectralon® pinhole. In the liquid interface, this will make it possible to constraint the absorption length of the liquid. Additionally, the same adaptor piece will also be used to install samples for taking measurements of their reflectance. It will be possible to position the samples in one of two positions, either with a 0° or an 8° in relation to the sphere's surface normal. The 8° degree positioning is generally used for diffuse reflectance measurements with TIS to avoid having specularly reflected light go back through the input port [28].

5.5 Designing a New Set-Up: continuous input flux measurements

A new iteration to the experimental set-up is being finalised for measuring the input flux of photons while taking the reflectance data (figure 5.9). The idea is to add a beam sampler (BSF10-UV from Thorlabs®), which works similarly to a beam splitter but divides the light beam into two beams of different proportions – the sampled beam corresponds to 1–10% of the original beam, and the remained goes into the sphere. The VUV reflectance measurements with a TIS of [17] employed a similar method, with a beam splitter, to have a reference of the incident flux of photons while measuring diffuse reflectance. This

is important because it makes it possible to correct for changes of photon flux from run to run. Even though the current fed to the LEDs was seen to be very stable, the fact is we are operating the LEDs with lower currents than their designed regime, especially in the case of the 405 nm and 490 nm LEDs. There could be unexpected oscillations in the photon flux when operating in such a low current regime, and this method will allow to correct for any such changes.

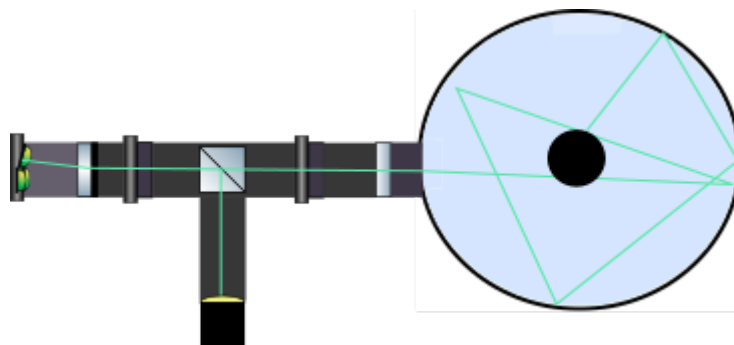


Figure 5.9: Schematic top-view of the new experimental set-up proposed. The beam sampler and the second PMT are shown.

Figure 5.9 shows a schematic of the new proposed detection scheme. The beam sampler is added between the two pinholes with a 45° in relation to the incident direction. A fraction of the input flux is measured by a second PMT, perpendicular to the collimation system. The beam sampler works by reflecting 1–10% of light, letting through the remainder of the beam. One of the advantages of this method is that since only a small percentage of the beam is sampled, a PMT can be used in photon counting mode to measure count rate with very high precision, without the worry of photon pile-up or even damaging the PMT. Additionally, beam samplers, in general, have a broader working wavelength than regular beam splitters.

Due to space constraints, the set-up was designed to have the beam sampler between the two pinholes. However, that means the system will have to be calibrated by measuring with the other PMT from the 0° ($1.5''$) port, similarly to what was described in the previous section. This calibration is needed to correctly account for the effect of the second pinhole. Nonetheless, this calibration would always be necessary to correct for uncertainties in the transmittance and reflection of the beam sampler.

Chapter 6

Results and Data Analysis

This chapter presents the results obtained in the course of this thesis. Two types of measurements were made: (1) measurements of the incident flux, following the steps detailed in 5.4; (2) measurements of the flux after multiple reflections inside the Spectralon® total integrating sphere as detailed in section 5.3.

The experimental results were compared with the Monte Carlo simulations performed in ANTS2. For that purpose, different reflectance models were used, namely a purely Lambertian model, and the modified Wolff model described in section 3.5. The results obtained with both models are compared. The same procedure and analysis can be made for any other reflectance models. For the modified Wolff model, a study of the changes in the diffuse albedo when changing the interface from air to water is also presented.

6.1 Measurements of the Incident Flux

Measurements were taken at two different distances from the input pinhole to test if the PMT was collecting all of the light entering the sphere. Each distance corresponds to the distance between the quartz surface of the PMT and the internal surface of the Spectralon pinhole. The larger distance ($d_1=83.3\pm 0.1$ mm) matches the distance between the input pinhole and the plane of the first reflection on the 0° . The shorter distance ($d_2=45.9\pm 0.1$ mm) is roughly at half that distance.

Table 6.1 summarises the results from measuring the incident photon flux, $\Phi_{in}(\lambda)$, entering the TIS, as described in section 5.4. Each measurement was taken once, for a duration of 60 seconds. A better idea of the effect of systematics in LED fluctuations and the optical stability of the system would require more statistics. However, the ratio of the counts between d_1 and d_2 gives us an idea of the stability of the measurement with respect to the systematics we wished to constraint. Ideally, since the beam is very well collimated (~ 2.5 mm diameter at the plane of first reflection) all light should fall entirely on the much larger photocathode (15 mm diameter). However, internal reflections in the collimation system could result in a fraction of photons incident in an area outside of the photocathode, being a possible source of systematic errors.

The photon fluxes are significantly larger in the measurement of the incident beam when compared with the photon flux inside the TIS, which causes the high-count measurements to be affected more significantly by photon pile-up – a 5.6% correction for the 490 nm LED. However, even with these kinds of fluxes (high counts), for most LEDs, the difference between the fluxes measured in d_1 and d_2 is small and not much different from the difference observed with the low count measurements. The exception is LED 255 nm

for which the low count measurement is clearly more stable.

Overall, the differences in flux for both distances are very small. Taking the average for the difference in flux observed at d_1 and d_2 yields 0.1 ± 2.2 %. Since the average does not point to any apparent additional flux measured at d_2 it seems that interreflections from the collimation system are reduced to a minimum. However, the larger variance indicates that possible LED fluctuations are the dominating factor in the observed differences.

Table 6.1: Incident flux measurements for each LED.

LED [nm]	$d_1=83.3$ mm [kcps]	$d_2=45.9$ mm [kcps]	$\frac{d_1}{d_2}$	$d_1=83.3$ mm [kcps]	$d_2=45.9$ mm [kcps]	$\frac{d_1}{d_2}$
High Counts				Low Counts		
255	466.1	495.4	0.94	50.8	50.1	1.01
275	489.3	484.4	1.01	45.1	45.1	1.00
285	418.4	416.0	1.01	40.97	40.61	1.01
310	354.9	350.4	1.01	101.1	102.7	0.98
355	1692	1657	1.02	NA	NA	NA
405	1199	NA	NA	428.6	422.9	1.01
490	1234	NA	NA	504.6	507.4	0.99

For each measurement, we acquired data for 60 seconds. Fluctuations in the LED's output and the optical system's stability are the primary source of uncertainty and not Poissonian fluctuations.

6.2 Measurements of the Flux in the Total Integrating Sphere

Measurements of the TIS throughput were taken for each LED in both air and water interfaces, as detailed in section 5.3. The temperature inside the chamber read 19.9°C during data taking. Table 6.2 summarises the results from these measurements. For each LED, the rate of counts in air and water are shown with the estimated uncertainty. For context, the number of runs taken into account to compute the uncertainty is also shown. The uncertainties are compared with the standard deviation of a Poisson distribution. We defined a gain as the ratio between the photon flux at the PMT window measured in water and the flux measured in air: $\Phi_{TIS}^{water} / \Phi_{TIS}^{air}$. In a perfect system, the only variations would be photoelectron emission statistics in the photocathode and electron multiplication (Poisson distribution). In reality, imperceptible variations in the geometry of the system from run to run might affect the measurements, or, alternatively, dust particles in the interior of the sphere can also affect its reflectance factor [28]. Nonetheless, these variations are small when translated into the computation of the gain. The measurements are consistent across the various runs even though they were made over a few weeks and the sphere and PMT were removed and installed a number of times, indicating that the set-up is mechanically stable and robust.

Table 6.2: Photon fluxes measured in the TIS for each LED (high counts).

LED [nm]	Φ_{TIS}^{air} [kcps]	$\sigma_{Poisson}$ [kcps]	#runs	Φ_{TIS}^{water} [kcps]	$\sigma_{Poisson}$ [kcps]	#runs	gain*	#runs
255	62.8±1.2	±0.3	3	92.1±0.8	±0.3	2	1.44±0.022	3
275	65.5±0.9	±0.3	3	99.8±0.7	±0.3	2	1.51±0.006	3
285	60.2±2.9	±0.3	3	92.4±0.05	±0.3	2	1.48±0.05	3
310	61.4±1.8	±0.3	3	101.4±1.0	±0.3	2	1.62±0.006	3
355	373.0±8.3	±0.6	3	537.6±5.0	±0.7	3	1.44±0.025	5
405	309.8±0.5	±0.6	2	474.7±3.0	±0.7	2	1.59±0.06	4
490	370.8±1.2	±0.6	2	507.5±2.2	±0.7	2	1.425±0.06	4

* The gain was computed taking into account also the low count measurements;

The sphere's attenuation factor is defined as the ratio of the detected photon flux in the TIS for both air (Φ_{TIS}^{air}) and water (Φ_{TIS}^{water}) and the input photon flux. The incident photon flux is different between the air and liquid due to the difference in the probability of reflection in the interface quartz-air and quartz-liquid. From the Fresnel equations, it can be seen that the transmittance will be higher for the water interface. To a first approximation, the incident flux can be corrected by the following factor:

$$\Phi_{in}^{water} = \Phi_{in} * \frac{T(0, n_{quartz}, n_{water})}{T(0, n_{quartz}, n_{air})}, \quad (6.1)$$

function of the Fresnel transmittance (T) for both interfaces, which was computed for normal incidence given the very small incident angles at the input of the TIS. This correction amounts to a difference between the incident flux in water and air of +3.81% ($\lambda=255$ nm) at most. Higher-order corrections originating from at least two reflections, first in the interface between the quartz and the interior of the sphere and then in the interface between the quartz and the collimation system, were not included due to their small value. For example, the second order correction amounts to, at most (255 nm), a factor of 1.03×10^{-4} . Additionally, the pile-up correction (section 5.2.1) was applied to all high count measurements, resulting in a correction of up to 2.5 % for the fluxes measured in the TIS.

Figure 6.1 plots the attenuation factor, Φ_{in}/Φ_{TIS} , for both interfaces across the wavelength range covered by the LEDs. The shaded area indicates the upper and lower limits based on the uncertainty of the attenuation factor. As expected from the Spectralon® reflectance, the attenuation decreases as the reflectance increases with increasing wavelength. In the water interface, the attenuation is smaller, attending to the expected increase in diffuse reflectance.

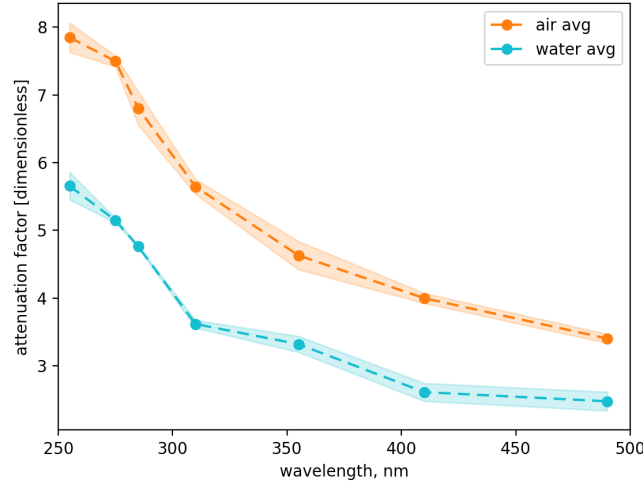


Figure 6.1: Attenuation factor, Φ_{in}/Φ_{TIS} in air and water interfaces. Computed for all runs, both high and low counts.

6.3 Analysis with a Monte-Carlo simulation in ANTS2

6.3.1 The analytical approach

The reflectance factor of the Spectralon® walls of the sphere can be estimated as a starting point from equation 4.6. Equation 4.6 can be arranged for M to yield:

$$M = \frac{T_{det} \pi A_s}{\Phi_{in} A_d \Omega_d}, \quad (6.2)$$

where A_d is the detector's active area with a value of 47.12 mm². The surface area of the sphere A_s is 2207 mm². Ω_d is the projected solid angle associated with the detector's field of view. In this case, since the photomultiplier is placed at the surface level of the sphere, Ω_d can be taken to be π to good approximation. The port fraction assumes that non-Spectralon® surfaces are completely non-reflecting, which is a very coarse approximation in the case of the PMT window. This fact was corrected for by multiplying the port fraction corresponding to the PMT window by the Fresnel transmission coefficient for each wavelength. With this correction the port fraction has a value of 2.992% at 255 nm and 3.005% at 490 nm. From M and from the estimated port fraction, the albedo ρ_l can be computed:

$$\rho_l = \frac{M}{1 + M(1 - f)}. \quad (6.3)$$

The Lambertian albedo, ρ_l , is essentially the reflectance factor (equation 3.36). In fact, when considering pure Lambertian reflectance, the reflectance factor, REFF, corresponds to the bi-hemispherical reflectance. Recall equation 3.39; integration of the incident and viewing solid angles each over the full hemisphere yields the bi-hemispherical reflectance [70]:

$$R(2\pi, 2\pi) = \frac{1}{\pi} \int_{w_r} \int_{w_i} \varrho_r(\theta_i, \phi_i, \theta_r, \phi_r) d\Omega_i d\Omega_r = \rho_l. \quad (6.4)$$

Using equation 6.2 with the measured counts at the detector (table 6.2) and Φ_{in} (table 6.1), ρ_l can be computed for each LED. This analytic approach can be directly compared with the Lambertian model.

This method has several limitations; one of them is not taking into consideration reflections at the input and detector ports, which can be partially corrected for as mentioned above. Another limitation is that it does not consider the Spectralon® baffle inside the sphere, which is possible with the simulations in ANTS2. Nonetheless, it provides a good reference point for cross-checking the results obtained with the more advanced methods described below.

6.3.2 The Lambertian Model

Monte Carlo simulations in ANTS2 were used to test different models of reflectance. The simulations were performed for the Lambertian model and the modified version of the Wolff model, but the same method can be used to test any other reflectance model. The geometry and optical parameters used are the ones described in section 4.5 (table 4.3). For each wavelength, 2.5 million photons were simulated. This number was chosen to have good statistics so that the results were repeatable. The albedo of the reflectance model in use is changed manually until the same attenuation factor as the one observed experimentally (fig. 6.1) is obtained in the simulation (to 0.1% precision). The upper and lower limits for the albedo were obtained by repeating the same process for the upper and minimum bounds on the attenuation factor. Figure 6.2 compares the ρ_l values obtained with equation 6.2 with the ones obtained with the Lambert model in ANTS2 for the air interface. The reflectance values of a Spectralon® calibration standard from Labsphere [115] are also shown for comparison, where the shaded area represents the uncertainty in the calibration datasheet.

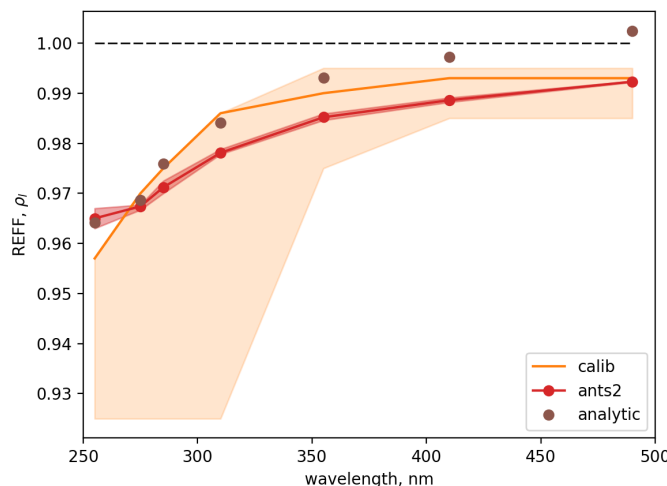


Figure 6.2: Reflectance factor obtained for the analytic method and a simulation with the Lambert model in ANTS2. The calibration reference values from Labsphere are shown for comparison [115].

The same procedure to find ρ_l in the air interface can be used for the water interface. Figure 6.3 shows the Lambertian albedo in both air and water interfaces. For the 490 nm

wavelength, only the lower limit of the attenuation factor was reachable at an albedo value of 0.99985. Nonetheless, a clear increase in ρ_l can be observed when the interface changes from air to liquid. The increase in the percentage of the bi-hemispherical reflectance with the changing interface is $+2.94 \pm 0.3\%$ at 255 nm and $+1.09 \pm 0.08\%$ at 405 nm. Additionally, note that the uncertainty bands for the water case are much smaller because small differences in albedo above 0.99 translate in bigger changes in the photon count rates.

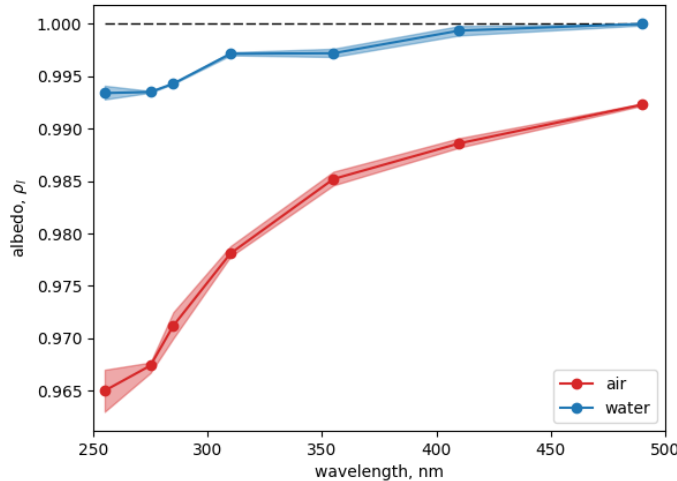


Figure 6.3: Lambertian albedos estimated in ANTS2 simulations in both air and water interfaces in accordance with the attenuation factors obtained experimentally.

6.3.3 The Modified Wolff Model of diffuse reflection

Since the Lambert model is an ideal approximation that does not include specular reflection or surface roughness, it is of great interest to also test a model that does. In this section, we detail the analysis in ANTS2 with the modified Wolff model (section 3.5).

The modified Wolff model considers multiple order internal reflections between the diffuser and the original medium, and as such, it depends directly on the refractive indices of the optical interfaces since the Fresnel equations define the amount of light that enter and leave the scattering medium. The left panel of the figure 6.4 shows the wavelength-dependent Fresnel transmission (normal incidence) at the relevant optical interfaces, while the right panel shows the refractive index values used in the simulations as a function of wavelength. As discussed in section 4.5, the refractive index of Spectralon® was kept constant at 1.35. It will be important to study in the future how the refractive index of Spectralon® changes with wavelength.

In ANTS2, the modified Wolff model has the following optical parameters:

- 1 – σ_α , as described in section 3.4;
- 2 – the slope distribution model to be used, which makes use of the σ_α parameter;
- 3 – the specular spike coefficient, which is introduced manually as an addition to the GOA model (section 3.4);
- 4 – the multiple-scattering albedo, ρ_l^1 .

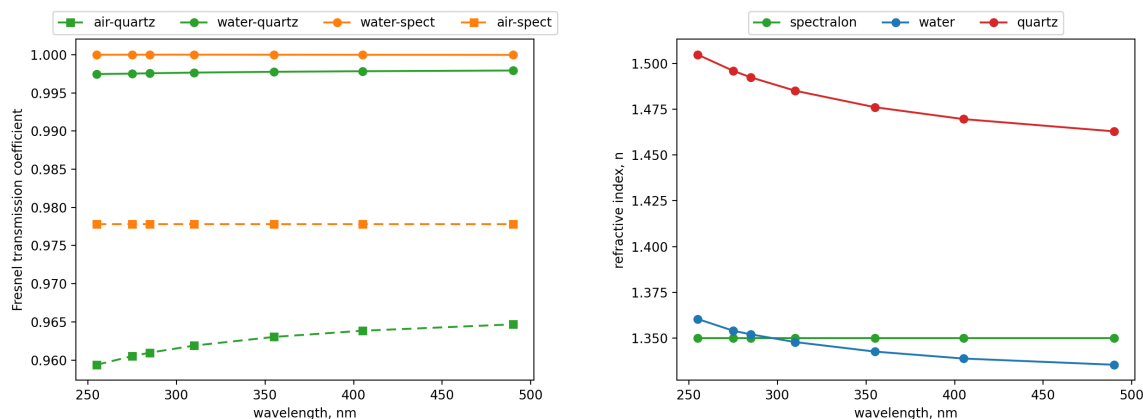


Figure 6.4: On the left, Fresnel transmission coefficient at the optical interfaces. On the right the refractive index for different wavelengths.

In line with the work developed in [16], the slope distribution model used was the Trowbridge-Reitz distribution. Spectralon[®] is known to be fairly rough [27], so σ_α was fixed at 0.12. Also, in [16] it was observed that for diffusers with broader specular lobes a specular spike was not observed. For that reason, the specular spike wasn't considered in these simulations. The multiple-scattering albedo was left as a free parameter.

Figure 6.5 shows the results obtained for the multiple-scattering albedo, ρ_t^1 , in both air and water. The multiple-scattering albedo in the air interface is higher than the Lambertian albedo because, as the Fresnel reflection coefficient is higher for the Spectralon-air interface, the light stays longer inside the bulk material increasing the absorption probability. The multiple-scattering albedo in water is very close to the Lambertian albedo because the Wolff model gets closer to the Lambertian model when the refraction indices of the two media get closer, like is the case for water and Spectralon[®].

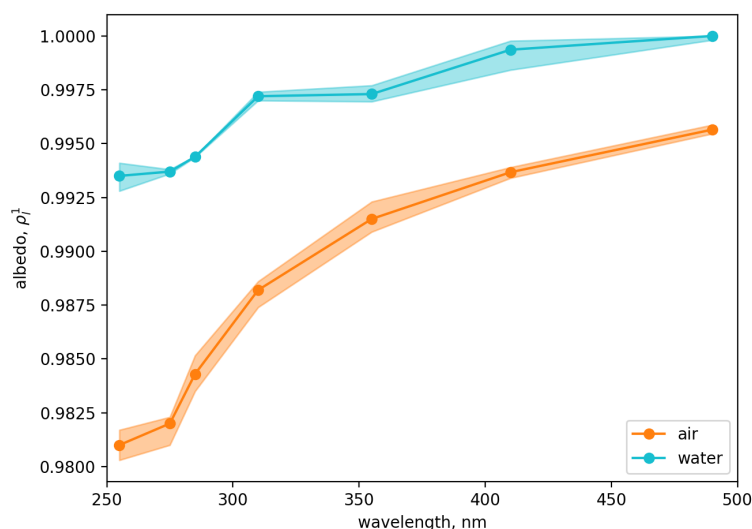


Figure 6.5: Multiple-scattering albedo from the Wolff model estimated in ANTS2 simulations in both air and water interfaces according to the attenuation factors obtained experimentally.

When changing from air to the water interface, an increase in ρ_l^1 is observed. It is unclear why this happens, since by design ρ_l^1 should depend solely on the diffuser properties and not on the optical properties of the interfacing medium. It will be interesting in the future to do an analysis of these results with the Chandrasekhar model (section 3.3.3) instead of the internal-Lambertian model used in this implementation. It could also be worthwhile to investigate further the effects of surface roughness.

Similarly to what happened with the Lambert model, only the lower limit value of the attenuation factor was possible to reach at an albedo value of 0.99981. One possible explanation for this is that the absorption length for 490 nm was overestimated in the analysis. In fact, all results are affected by uncertainties in the absorption length in water. In that regard it is useful to test the degeneracy of the absorption length in water with the multiple-scattering albedo. To test how the absorption length of water affects the estimation of ρ_l^1 , simulations in ANTS2 were performed using the attenuation factor in water at 255 nm. The simulation was repeated for different values of absorption length. Figure 6.6 shows how ρ_l^1 varies with varying absorption length for the fixed attenuation factor value observed experimentally for the 255 nm wavelength.

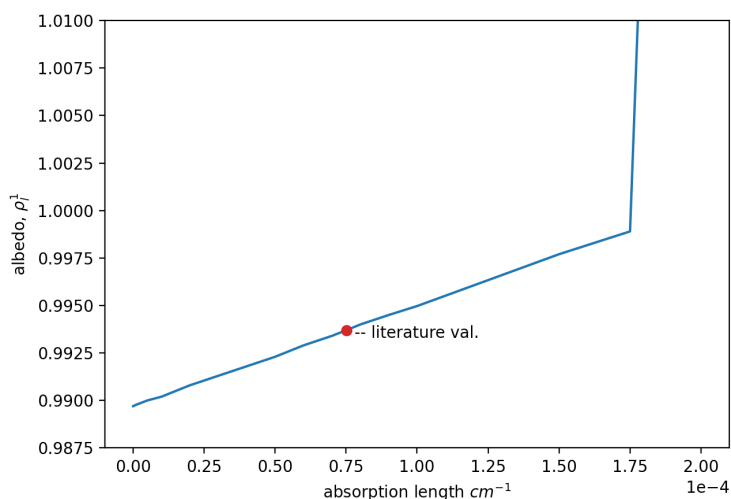


Figure 6.6: Dependence of the multiple-scattering albedo of the Wolff model on the absorption length of water, for the 255 nm wavelength.

Naturally, as the absorption length approaches zero, it stops affecting the albedo. On the other hand, as the absorption length increases, it reaches a value where the albedo reaches one, and the target attenuation factor value is no longer reachable. This stresses the need to constraint the absorption length of the water being used, which will be possible with the new port adaptor piece under development described in section 5.4.

Chapter 7

Conclusions and Future Work

The main goal of the work presented in this thesis was to study how the reflectance of PTFE changes when it is immersed in a liquid medium. To that end, an experimental set-up employing a Spectralon® (PTFE based) total integrating sphere was developed. The 819C-SL-3.3 total integrating sphere from Newport with a 3.3" internal diameter was adapted for use while filled with liquid. The adaptations include two custom ports designed and developed in the course of this work. One of these custom ports was equipped with a sealed fused quartz window to isolate the sphere from the collimation system. A Spectralon® pinhole at the input to the sphere minimises light backscattered into the collimation system. The other custom port (north pole) was designed to fit the PMT vertically and ensure the PMT window is submerged when taking data with liquids. The same port allows for filling and emptying the sphere without interfering with the set-up. As the light sources, 7 LEDs with peak emission wavelengths in the range from 255 to 490 nm were used. These were mounted on the same compact PCB (LED matrix), equipped with a diffuser to reduce the differences in the spatial pattern of light emission between the LEDs. A control system for the LEDs, including electronics and firmware, was developed to switch on and off the different LEDs (one at a time) and adjust the current without mechanical interference with the set-up.

Two types of measurements were made with the set-up. The incident photon flux from the collimation system into the sphere in an air interface was measured with the PMT in a horizontal position aligned with the beam. The photon flux at the TIS output port after multiple reflections was measured with the PMT in a vertical position. This output flux was measured first in air and then with the TIS filled with pure water. The measurements from multiple runs are consistent throughout, and there is no indication of significant systematic errors from the mechanical handling of the system. The proposed scheme (section 5.5) to measure the incident flux in parallel using a beam sampler will help to reduce the uncertainties related with the incident flux even further.

In parallel, we developed a Monte Carlo simulation with the ANTS2 software package to test both the classic Lambertian model and a modified version of the Wolff and Oren-Nayar model. The models were used to study the difference in the observed photon flux in the TIS for an air and a water interfaces and its relation to the change in the diffuse reflectance of the Spectralon® surface. To our knowledge, this is the first experiment to systematically study diffuse reflection models in a liquid interface.

Analysis with the Lambertian model showed good agreement between the reflectance of the Spectralon® with the calibration reference values from Labsphere 6.2 in the air interface. The Lambertian model allows for direct comparison with the bi-hemispherical

reflectance. An increase in the reflectance when changing from air to a liquid interface was observed. The observed increase in the percentage of the reflectance was $+2.94 \pm 0.3\%$ at 255 nm and $+1.09 \pm 0.08\%$ at 405 nm. These results are in good agreement with the result by Voss et al. [33], who saw a $+2\%$ increase in the reflectance of Spectralon® in the water interface at 633 nm (He-Ne laser).

The analysis with the modified Wolff model was made by fitting the multiple scattering albedo to match the fluxes observed experimentally. The Wolff model takes into account the changes in the refractive indices at the optical interfaces, so the change in interface covers part of the reflectance increase. However, a clear increase in the multiple scattering albedo was still observed for the liquid interface, albeit smaller than the one observed for the Lambertian albedo. The reason for this is unclear since the multiple scattering albedo is a function only of the scattering and absorbing characteristics of the diffuser itself and independent of the optical interfaces. It would be of interest in the future to test the Chandrasekhar model of internal scattering to further investigate this matter. Chandrasekhar's results in radiative transfer have been used before to model Spectralon® calibration data for the Medium Resolution Imaging Spectrometer (MERIS) aboard ENVISAT, the European Space Agency's advanced polar-orbiting Earth observation satellite [26]. Another direction that might prove worthwhile is to study the effects of surface roughness in these results in more detail.

One parameter that has a high impact on the estimated albedo in the liquid interface is absorption length. A clear degeneracy with the absorption length of water was observed (figure 6.6). The new proposed adaptor port piece (section 5.4) will allow us to measure the incident flux in a liquid interface as well as vary the distance between the PMT and the input pinhole. This update will be of great relevance to constraint substantially the uncertainty on the absorption length. The new set-up will help to clarify if the difficulty in reproducing the experimental results with simulation for the 490 nm wavelength was due to an overestimation of the absorption length or not.

Additionally, in the interest of a more exhaustive analysis, it will be of great interest to perform measurements with other liquids with different properties. For example, to see if the diffuse reflectance might also be dependent on physical parameters like the dipole moment of the liquid molecules. Table 7.1 lists liquids of interest for future tests as well as some of the possibly relevant parameters. The absorption length values were taken from [96] and [116]. The values of the dipole moments were taken from the CHERIC, Chemical Engineering and Materials Research Information Center, database [117].

Very soon, the upgrades described in previous sections, relative to the adaptor port pieces for the sphere, will enable taking measurements with these other liquids, ethanol and glycerine. These new measurements will provide valuable experimental data to further study diffuse reflectance models.

This work is relevant to the development of the noble liquid scintillation detectors which employ PTFE as the primary reflector material in contact with the target liquid [1]. Accurate optical simulations of the target medium and the reflecting PTFE are crucial to the understanding of light collection and ultimately, detector sensitivity [13]. There is also an interest for the computer graphics community and for photometric computer vision algorithms in understanding diffuse reflectance and its behaviour in a liquid interface [31, 18]. Finally, Spectralon® is the best-known diffuser material in the visible range. It is widely used as a calibration reference in remote sensing and space applications [26]. There is interest in modelling the diffuse reflectance of Spectralon® itself, as past works show [27, 26].

Table 7.1: Possible liquids to be used in the TIS

	$n[*]$	Absorption (mm^{-1})	dipole mom. (debye))
water	1.339 [102]	0.53×10^{-5} [96]	1.8 [117]
ethanol	1.372 [102]	$6.7 \pm 0.5 \times 10^{-4}$ (530 nm) [116]	1.7 [117]
glycerine	1.482 [102]	NA [†]	3 [117]

* Unless otherwise stated, presented values are for 405 nm;

† There are no measurements for the extinction coefficient, k , above 140 nm, but the optical constant values indicate the absorption length should be very high for wavelengths above [118].

Ultimately, the work developed in this thesis is a valuable addition to studies of diffuse reflectance. Minor upgrades can be used to test the reflectance of various samples in a liquid interface, for example, the PTFE samples used in the LZ experiment. The samples can be installed with 0 or 8° degrees relative to the surface normal of the sphere. Generally, the 8° position is used to avoid having specularly reflected light going back through the input port. Often, the samples are tested with both 0 and 8° degree positions so that the specular fraction of reflection can be factored out [28]. This functionality would also be interesting to test further the predictions of the specular and diffuse reflection components of various models.

Bibliography

- [1] DS Akerib, CW Akerlof, D Yu Akimov, A Alqahtani, SK Alsum, TJ Anderson, N Angelides, HM Araújo, A Arbuckle, JE Armstrong, et al. “The LUX-ZEPLIN (LZ) experiment”. In: *Nuclear Instruments and Methods in Physics Research Section A: Accelerators, Spectrometers, Detectors and Associated Equipment* 953 (2020), p. 163047.
- [2] Elena Aprile, Xenon Collaboration, et al. “The XENONnT Dark Matter Experiment”. In: *APS 2017* (2017), J9–003.
- [3] D Akimov, JB Albert, P An, C Awe, PS Barbeau, B Becker, V Belov, MA Blackston, L Blokland, A Bolozdynya, et al. “First Detection of Coherent Elastic Neutrino-Nucleus Scattering on Argon”. In: *arXiv preprint arXiv:2003.10630* (2020).
- [4] LUX-ZEPLIN LZ Collaboration, DS Akerib, CW Akerlof, A Alqahtani, SK Alsum, TJ Anderson, N Angelides, HM Araújo, JE Armstrong, M Arthurs, et al. “Projected sensitivity of the LUX-ZEPLIN experiment to the $0\nu\beta\beta$ decay of Xe-136”. In: *Physical Review C* 102.1 (2020), p. 014602.
- [5] XENON Collaboration. “Observation of two-neutrino double electron capture in Xe-124 with XENON1T”. In: *Nature* 568.7753 (2019), pp. 532–535.
- [6] N Ackerman, B Aharmim, M Auger, DJ Auty, PS Barbeau, K Barry, L Bartoszek, E Beauchamp, V Belov, C Benitez-Medina, et al. “Observation of Two-Neutrino Double-Beta Decay in Xe-136 with the EXO-200 Detector”. In: *Physical Review Letters* 107.21 (2011), p. 212501.
- [7] “Dark matter in cosmology”. In: *Particle Dark Matter: Observations, Models and Searches*. Cambridge University Press, 2010, pp. 1–2.
- [8] Fritz Zwicky. “The redshift of extragalactic nebulae”. In: *Helvetica Physica Acta* 6 (1933), pp. 110–127.
- [9] Gianfranco Bertone. *Particle dark matter: observations, models and searches*. Cambridge University Press, 2010.
- [10] Vitaly Chepel and Henrique Araújo. “Liquid noble gas detectors for low energy particle physics”. In: *Journal of Instrumentation* 8.04 (2013), R04001.
- [11] E. Aprile and T. Doke. “Liquid Xenon Detectors for Particle Physics and Astrophysics”. In: *Reviews of Modern Physics* (2009).
- [12] F Neves, A Lindote, A Morozov, V Solovov, C Silva, P Bras, JP Rodrigues, and MI Lopes. “Measurement of the absolute reflectance of polytetrafluoroethylene (PTFE) immersed in liquid xenon”. In: *Journal of Instrumentation* 12.01 (2017), P01017.

- [13] DS Akerib, S Alsum, HM Araújo, X Bai, AJ Bailey, J Balajthy, P Beltrame, EP Bernard, A Bernstein, TP Biesiadzinski, et al. “Calibration, event reconstruction, data analysis, and limit calculation for the LUX dark matter experiment”. In: *Physical Review D* 97.10 (2018), p. 102008.
- [14] Victor R Weidner and Jack J Hsia. “Reflection properties of pressed polytetrafluoroethylene powder”. In: *Josa* 71.7 (1981), pp. 856–861.
- [15] KF Poole and MM Michaelis. “Hialvac and Teflon outgassing under ultra-high vacuum conditions”. In: *Vacuum* 30.10 (1980), pp. 415–417.
- [16] Claudio Frederico Pascoal da Silva. “Reflection Distribution of the Fluoropolymers for the Xenon Scintillation Light”. In: *PhDT* (2010).
- [17] Puja Kadkhoda, Detlev Ristau, and Ferdinand von Alvensleben. “Total scatter measurements in the DUV/VUV”. In: *Laser-Induced Damage in Optical Materials: 1998*. Vol. 3578. International Society for Optics and Photonics. 1999, pp. 544–554.
- [18] Claudio Silva, J Pinto da Cunha, A Pereira, Vitaly Chepel, MI Lopes, V Solovov, and F Neves. “Reflectance of polytetrafluoroethylene for xenon scintillation light”. In: *Journal of Applied Physics* 107.6 (2010), p. 064902.
- [19] Thomas James Whitis. “Measurement of Time Projection Chamber Optical Properties and Xenon Circulation System Development for The LZ Experiment”. PhD thesis. Case Western Reserve University, 2019.
- [20] Lawrence B Wolff. “Diffuse-reflectance model for smooth dielectric surfaces”. In: *JOSA A* 11.11 (1994), pp. 2956–2968.
- [21] P Agnes, IFM Albuquerque, T Alexander, AK Alton, DM Asner, HO Back, K Biery, V Bocci, G Bonfini, W Bonivento, et al. “Simulation of argon response and light detection in the DarkSide-50 dual phase TPC”. In: *Journal of Instrumentation* 12.10 (2017), P10015.
- [22] Johann Heinrich Lambert. *Photometria sive de mensura et gradibus luminis, colorum et umbrae*. Klett, 1760.
- [23] S Bricola, A Menegolli, M Prata, MC Prata, GL Raselli, M Rossella, and C Vignoli. “Noble-gas liquid detectors: measurement of light diffusion and reflectivity on commonly adopted inner surface materials”. In: *Nuclear Physics-Section B-PS-Proceedings Supplements* 172 (2007), pp. 260–262.
- [24] Michael Oren and Shree K Nayar. “Generalization of the Lambertian model and implications for machine vision”. In: *International Journal of Computer Vision* 14.3 (1995), pp. 227–251.
- [25] D Akimov, V Belov, A Konovalov, A Kumpan, O Razuvaeva, D Rudik, and G Simakov. “Fast component re-emission in Xe-doped liquid argon”. In: *Journal of Instrumentation* 14.09 (2019), P09022.
- [26] Grégory Bazalgette Courrège-Lacoste, Jos JM Groote-Schaarsberg, Rudolf Sprik, and Steven Delwart. “Modeling of Spectralon diffusers for radiometric calibration in remote sensing”. In: *Optical engineering* 42.12 (2003), pp. 3600–3608.
- [27] MP Levesque and M Dissanska. “Measurement and modeling of the SpectralonTM spectro-polarimetric bidirectional reflectance distribution function (BRDF)”. In: *Defence Research and Development Canada* (2016).

- [28] LLC SphereOptics. “Integrating sphere, design and applications”. In: *Technical Information* (2007), pp. 1–4.
- [29] American Society for Testing and Materials (ASTM). *Standard Specification for Reagent Water, ASTM D1193 - 06(2018)*. URL: <https://www.astm.org/Standards/D1193.htm>.
- [30] A. Morozov, V. Solovov, R. Martins, F. Neves, V. Domingos, and V. Chepel. “ANTS2 package: simulation and experimental data processing for Anger camera type detectors”. In: *Journal of Instrumentation* (2016).
- [31] Lawrence B Wolff, Shree K Nayar, and Michael Oren. “Improved diffuse reflection models for computer vision”. In: *International Journal of Computer Vision* 30.1 (1998), pp. 55–71.
- [32] BJ Mount. *LUX-ZEPLIN (LZ) technical design report*. Tech. rep. Argonne National Lab.(ANL), Argonne, IL (United States); Pacific Northwest . . . , 2017.
- [33] Kenneth J Voss and Hao Zhang. “Bidirectional reflectance of dry and submerged Labsphere Spectralon plaque”. In: *Applied Optics* 45.30 (2006), pp. 7924–7927.
- [34] Dragomir M Davidović, Jovan Vukanić, and Dušan Arsenović. “Two new analytic approximations of the Chandrasekhar’s H function for isotropic scattering”. In: *Icarus* 194.1 (2008), pp. 389–397.
- [35] Elena Aprile, A Curioni, Karl-Ludwig Giboni, M Kobayashi, UG Oberlack, and S Zhang. “Compton imaging of MeV gamma-rays with the liquid xenon gamma-ray imaging telescope (LXeGRIT)”. In: *Nuclear Instruments and Methods in Physics Research Section A: Accelerators, Spectrometers, Detectors and Associated Equipment* 593.3 (2008), pp. 414–425.
- [36] M Auger, DJ Auty, PS Barbeau, L Bartoszek, E Baussan, E Beauchamp, C Benitez-Medina, M Breidenbach, D Chauhan, B Cleveland, et al. “The EXO-200 detector, part I: detector design and construction”. In: *Journal of Instrumentation* 7.05 (2012), P05010.
- [37] Pietro Benetti, E Calligarich, R Dolfini, A Gigli Berzolari, F Mauri, L Mazzone, C Montanari, A Piazzoli, A Rappoldi, GL Raselli, et al. “Detection of energy deposition down to the keV region using liquid xenon scintillation”. In: *Nuclear Instruments and Methods in Physics Research Section A: Accelerators, Spectrometers, Detectors and Associated Equipment* 327.1 (1993), pp. 203–206.
- [38] Craig E Aalseth, F Acerbi, P Agnes, IFM Albuquerque, T Alexander, A Alici, AK Alton, P Antonioli, S Arcelli, R Ardito, et al. “DarkSide-20k: A 20 tonne two-phase LAr TPC for direct dark matter detection at LNGS”. In: *The European Physical Journal Plus* 133.3 (2018), p. 131.
- [39] DN McKinsey, LZ Collaboration, et al. “The LZ dark matter experiment”. In: *Journal of Physics Conference Series*. Vol. 718. 4. 2016, p. 042039.
- [40] DS Akerib, CW Akerlof, D Yu Akimov, SK Alsum, HM Araújo, X Bai, AJ Bailey, J Balajthy, S Balashov, MJ Barry, et al. “LUX-ZEPLIN (LZ) conceptual design report”. In: *arXiv preprint arXiv:1509.02910* (2015).
- [41] JA Nikkel, T Gozani, C Brown, J Kwong, DN McKinsey, Y Shin, S Kane, C Gary, and M Firestone. “Liquefied Noble Gas (LNG) detectors for detection of nuclear materials”. In: *Journal of Instrumentation* 7.03 (2012), p. C03007.

- [42] M Szydagis, N Barry, K Kazkaz, J Mock, D Stolp, M Sweany, M Tripathi, S Uvarov, N Walsh, and M Woods. “NEST: a comprehensive model for scintillation yield in liquid xenon”. In: *Journal of Instrumentation* 6.10 (2011), P10002.
- [43] E Aprile, Jelle Aalbers, F Agostini, M Alfonsi, L Althueser, FD Amaro, Vasile C Antochi, E Angelino, F Arneodo, Derek Barge, et al. “Search for light dark matter interactions enhanced by the migdal effect or bremsstrahlung in XENON1T”. In: *Physical review letters* 123.24 (2019), p. 241803.
- [44] JD Lewin and PF Smith. “Review of mathematics, numerical factors, and corrections for dark matter experiments based on elastic nuclear recoil”. In: *Astroparticle Physics* 6.1 (1996), pp. 87–112.
- [45] A Bueno, MC Carmona, J Lozano, and S Navas. “Observation of coherent neutrino-nucleus elastic scattering at a beta beam”. In: *Physical Review D* 74.3 (2006), p. 033010.
- [46] Chris Hagmann and Adam Bernstein. “Two-phase emission detector for measuring coherent neutrino-nucleus scattering”. In: *IEEE transactions on Nuclear Science* 51.5 (2004), pp. 2151–2155.
- [47] Jayden L Newstead, Rafael F Lang, and Louis E Strigari. “Atmospheric neutrinos in a next-generation xenon dark matter experiment”. In: *arXiv preprint arXiv:2002.08566* (2020).
- [48] Pilar Coloma, MC Gonzalez-Garcia, Michele Maltoni, and Thomas Schwetz. “COHERENT enlightenment of the neutrino dark side”. In: *Physical Review D* 96.11 (2017), p. 115007.
- [49] DS Akerib, CW Akerlof, SK Alsum, HM Araújo, M Arthurs, X Bai, AJ Bailey, J Balajthy, S Balashov, D Bauer, et al. “Projected WIMP sensitivity of the LUX-ZEPLIN dark matter experiment”. In: *Physical Review D* 101.5 (2020), p. 052002.
- [50] J Aalbers, F Agostini, M Alfonsi, FD Amaro, C Amsler, E Aprile, L Arazi, Francesco Arneodo, P Barrow, L Baudis, et al. “DARWIN: towards the ultimate dark matter detector”. In: *Journal of Cosmology and Astroparticle Physics* 2016.11 (2016), p. 017.
- [51] Masahiro Ibe, Wakutaka Nakano, Yutaro Shoji, and Kazumine Suzuki. “Migdal effect in dark matter direct detection experiments”. In: *Journal of High Energy Physics* 2018.3 (2018), pp. 1–36.
- [52] E Aprile, Jelle Aalbers, F Agostini, M Alfonsi, L Althueser, FD Amaro, Vasile C Antochi, E Angelino, JR Angevaare, F Arneodo, et al. “Excess electronic recoil events in XENON1T”. In: *Physical Review D* 102.7 (2020), p. 072004.
- [53] HongGuang Zhang, Abdusalam Abdukerim, Wei Chen, Xun Chen, YunHua Chen, XiangYi Cui, BinBin Dong, DeQing Fang, ChangBo Fu, Karl Giboni, et al. “Dark matter direct search sensitivity of the PandaX-4T experiment”. In: *Science China Physics, Mechanics & Astronomy* 62.3 (2019), p. 31011.
- [54] E Aprile, Jelle Aalbers, F Agostini, M Alfonsi, L Althueser, FD Amaro, Vasile C Antochi, E Angelino, JR Angevaare, F Arneodo, et al. “Projected WIMP sensitivity of the XENONnT dark matter experiment”. In: *Journal of Cosmology and Astroparticle Physics* 2020.11 (2020), p. 031.

- [55] Paulo Alexandre Brinca Costa Brás. “Finding a needle in a haystack: Background studies & WIMP detection efficiency in LUX”. PhD thesis. 2015.
- [56] Mark Guy Boulay, Deap Collaboration, et al. “DEAP-3600 dark matter search at SNOLAB”. In: *Journal of Physics: Conference Series*. Vol. 375. 1. IOP Publishing. 2012, p. 012027.
- [57] DS Akerib, HM Araújo, X Bai, AJ Bailey, J Balajthy, P Beltrame, EP Bernard, A Bernstein, TP Biesiadzinski, EM Boulton, et al. “Chromatographic separation of radioactive noble gases from xenon”. In: *Astroparticle Physics* 97 (2018), pp. 80–87.
- [58] D-M Mei and A Hime. “Muon-induced background study for underground laboratories”. In: *Physical Review D* 73.5 (2006), p. 053004.
- [59] MJ Chant. “Dielectric properties of some insulating materials over the temperature range 4· 2–300 K”. In: *Cryogenics* 7.6 (1967), pp. 351–354.
- [60] Properties Handbook. *Teflon PTFE*.
- [61] DS Akerib, HM Araújo, X Bai, AJ Bailey, J Balajthy, E Bernard, A Bernstein, A Bradley, D Byram, SB Cahn, et al. “Radiogenic and muon-induced backgrounds in the LUX dark matter detector”. In: *Astroparticle Physics* 62 (2015), pp. 33–46.
- [62] E Aprile, K Arisaka, F Arneodo, A Askin, L Baudis, A Behrens, K Bokeloh, E Brown, JMR Cardoso, B Choi, et al. “Material screening and selection for XENON100”. In: *Astroparticle Physics* 35.2 (2011), pp. 43–49.
- [63] Emily Grace, Alistair Butcher, Jocelyn Monroe, and James A Nikkel. “Index of refraction, Rayleigh scattering length, and Sellmeier coefficients in solid and liquid argon and xenon”. In: *Nuclear Instruments and Methods in Physics Research Section A: Accelerators, Spectrometers, Detectors and Associated Equipment* 867 (2017), pp. 204–208.
- [64] S Kravitz, RJ Smith, L Hagaman, EP Bernard, DN McKinsey, L Rudd, L Tvrznikova, GD Orebi Gann, and M Sakai. “Measurements of angle-resolved reflectivity of PTFE in liquid xenon with IBEX”. In: *The European Physical Journal C* 80.3 (2020), pp. 1–20.
- [65] C Silva, J Pinto da Cunha, A Pereira, MI Lopes, V Chepel, V Solovov, and F Neves. “A model of the reflection distribution in the vacuum ultra violet region”. In: *Nuclear Instruments and Methods in Physics Research Section A: Accelerators, Spectrometers, Detectors and Associated Equipment* 619.1-3 (2010), pp. 59–62.
- [66] Kenneth E Torrance and Ephraim M Sparrow. “Theory for off-specular reflection from roughened surfaces”. In: *Josa* 57.9 (1967), pp. 1105–1114.
- [67] Richard P Feynman, Robert B Leighton, and Matthew Sands. “The feynman lectures on physics; vol. i”. In: *American Journal of Physics* 33.9 (1965), pp. 750–752.
- [68] Max Born and Emil Wolf. *Principles of optics: electromagnetic theory of propagation, interference and diffraction of light*. Elsevier, 2013.
- [69] Lawrence B Wolff. “Relative brightness of specular and diffuse reflection”. In: *Optical Engineering* 33.1 (1994), pp. 285–294.

- [70] Fred E Nicodemus, Joseph C Richmond, Jack J Hsia, IW Ginsberg, and T Limperis. “Geometrical considerations and nomenclature for reflectance”. In: *NBS monograph* 160 (1992), p. 4.
- [71] Gareth Hougham, Patrick E Cassidy, Ken Johns, and Theodore Davidson. *Fluoropolymers 2: Properties. Topics in Applied Chemistry*. Springer, 1999.
- [72] Michael I Mishchenko. “Vector radiative transfer equation for arbitrarily shaped and arbitrarily oriented particles: a microphysical derivation from statistical electromagnetics”. In: *Applied optics* 41.33 (2002), pp. 7114–7134.
- [73] Bruce Hapke. *Theory of reflectance and emittance spectroscopy*. Cambridge university press, 2012.
- [74] GH Goedecke. “Radiative transfer in closely packed media”. In: *JOSA* 67.10 (1977), pp. 1339–1348.
- [75] Knut Stamnes. “The theory of multiple scattering of radiation in plane parallel atmospheres”. In: *Reviews of Geophysics* 24.2 (1986), pp. 299–310.
- [76] N Huber, J Heitz, and D Bäuerle. “Pulsed-laser ablation of polytetrafluoroethylene (PTFE) at various wavelengths”. In: *The European Physical Journal Applied Physics* 25.1 (2004), pp. 33–38.
- [77] Subrahmanyam Chandrasekhar. *Radiative transfer*. Courier Corporation, 2013.
- [78] Kari Lumme, Hannu Karttunen, and William M Irvine. “Roughness of the lunar soil”. In: *Earth, Moon, and Planets* 33.1 (1985), pp. 19–29.
- [79] Virginija Jankauskaitė, Kristina Žukienė, and Stasė Petraitiienė. “Quantitative description of polychloroprene and piperylene–styrene blend films surface morphology”. In: *Polymer Engineering & Science* 47.6 (2007), pp. 824–829.
- [80] Jean M Bennett. “Measurement of the rms roughness, autocovariance function and other statistical properties of optical surfaces using a FECO scanning interferometer”. In: *Applied Optics* 15.11 (1976), pp. 2705–2721.
- [81] Françoise Varnier, Monique Rasigni, Georges Rasigni, Jean-Pierre Palmari, and A Liebaria. “Height and slope distributions for surfaces of rough metallic deposits”. In: *Applied optics* 21.20 (1982), pp. 3681–3684.
- [82] JA Sanchez-Gil and M Nieto-Vesperinas. “Light scattering from random rough dielectric surfaces”. In: *JOSA A* 8.8 (1991), pp. 1270–1286.
- [83] Wolfgang Freude and Gerhard K Grau. “Rayleigh-Sommerfeld and Helmholtz-Kirchhoff integrals: application to the scalar and vectorial theory of wave propagation and diffraction”. In: *Journal of lightwave technology* 13.1 (1995), pp. 24–32.
- [84] JA Sánchez-Gil, AA Maradudin, and ER Mendez. “Limits of validity of three perturbation theories of the specular scattering of light from one-dimensional, randomly rough, dielectric surfaces”. In: *JOSA A* 12.7 (1995), pp. 1547–1558.
- [85] Bruce Hapke and Hugh van Hoen. “Photometric studies of complex surfaces, with applications to the moon”. In: *Journal of Geophysical Research* 68.15 (1963), pp. 4545–4570.
- [86] Robert L Cook and Kenneth E. Torrance. “A reflectance model for computer graphics”. In: *ACM Transactions on Graphics (ToG)* 1.1 (1982), pp. 7–24.

- [87] Bruce Smith. “Geometrical shadowing of a random rough surface”. In: *IEEE transactions on antennas and propagation* 15.5 (1967), pp. 668–671.
- [88] Astroshop.pt. *TS optics ultra matte black paint*. URL: <https://www.astroshop.pt/guarda-luzes-dispersas-ofuscamento/ts-optics-anti-reflective-paint-matt-black-150ml/p,63295>.
- [89] F Nürnberg, B Kühn, and K Rollmann. “Metrology of fused silica”. In: *Laser-Induced Damage in Optical Materials 2016*. Vol. 10014. International Society for Optics and Photonics. 2016, 100140F.
- [90] Aissa Manallah and Mohamed Bouafia. “Application of the technique of total integrated scattering of light for micro-roughness evaluation of polished surfaces”. In: *Physics Procedia* 21 (2011), pp. 174–179.
- [91] KF Carr. “Integrating sphere theory and applications Part I: integrating sphere theory and design”. In: *Surface coatings international* 80.8 (1997), pp. 380–385.
- [92] Newport®. *Newport Total Integrating Sphere, 819C-SL-3.3*. URL: <https://www.newport.com/p/819C-SL-3.3>.
- [93] Rei Kitamura, Laurent Pilon, and Miroslaw Jonasz. “Optical constants of silica glass from extreme ultraviolet to far infrared at near room temperature”. In: *Applied optics* 46.33 (2007), pp. 8118–8133.
- [94] R Brun, A Gheata, and M Gheata. “The ROOT geometry package”. In: *Nuclear Instruments and Methods in Physics Research Section A: Accelerators, Spectrometers, Detectors and Associated Equipment* 502.2-3 (2003), pp. 676–680.
- [95] DR Bates. “Rayleigh scattering by air”. In: *Planetary and Space Science* 32.6 (1984), pp. 785–790.
- [96] Robin M Pope and Edward S Fry. “Absorption spectrum (380–700 nm) of pure water. II. Integrating cavity measurements”. In: *Applied optics* 36.33 (1997), pp. 8710–8723.
- [97] TI Quickenden and JA Irvin. “The ultraviolet absorption spectrum of liquid water”. In: *The Journal of Chemical Physics* 72.8 (1980), pp. 4416–4428.
- [98] Raymond C Smith and Karen S Baker. “Optical properties of the clearest natural waters (200–800 nm)”. In: *Applied optics* 20.2 (1981), pp. 177–184.
- [99] AJ Cox, Alan J DeWeerd, and Jennifer Linden. “An experiment to measure Mie and Rayleigh total scattering cross sections”. In: *American Journal of Physics* 70.6 (2002), pp. 620–625.
- [100] Akhlesh Lakhtakia. *Selected papers on linear optical composite materials*. Vol. 120. Society of Photo Optical, 1996.
- [101] Labsphere®. *Technical Guide, Reflectance Materials and Coatings*. URL: <https://www.labsphere.com/site/assets/files/2553/a-guide-to-reflectance-materials-and-coatings.pdf>.
- [102] Mikhail N. Polyanskiy. *Refractive index database*. URL: <https://refractiveindex.info> (visited on 03/15/2021).
- [103] George M Hale and Marvin R Querry. “Optical constants of water in the 200-nm to 200- μ m wavelength region”. In: *Applied optics* 12.3 (1973), pp. 555–563.

- [104] Ian H Malitson. “Interspecimen comparison of the refractive index of fused silica”. In: *Josa* 55.10 (1965), pp. 1205–1209.
- [105] Frédéric Leens. “An introduction to I 2 C and SPI protocols”. In: *IEEE Instrumentation & Measurement Magazine* 12.1 (2009), pp. 8–13.
- [106] Lasse Ylianttila and Josef Schreder. “Temperature effects of PTFE diffusers”. In: *Optical materials* 27.12 (2005), pp. 1811–1814.
- [107] HAMAMATSU PHOTONICS K. K. *Photomultiplier Tubes, Basics and Applications*. HAMAMATSU PHOTONICS K. K., 2007.
- [108] SO Flyckt and C Marmonier. “Photomultiplier tubes– principles & applications, Photonis, 2002”. In: URL http://www2.pv.infn.it/~debari/doc/Flyckt_Marmonier.pdf ().
- [109] Andreas Neiser, J. Adamczewski-Musch, Matthias Hoek, Wolfgang Koenig, Grzegorz Korcyl, Sergey Linev, Ludwig Maier, Jan Michel, Marek Palka, Manuel Penschuck, et al. “TRB3: a 264 channel high precision TDC platform and its applications”. In: *Journal of Instrumentation* 8.12 (2013), p. C12043.
- [110] P Assis, A Bernardino, A Blanco, F Clemêncio, N Carolino, O Cunha, M Ferreira, P Fonte, L Lopes, C Loureiro, et al. “A large area TOF-tracker device based on multi-gap Resistive Plate Chambers”. In: *Journal of Instrumentation* 11.10 (2016), p. C10002.
- [111] P Allison, F Arneodo, Xavier Bertou, NG Busca, PL Ghia, C Medina, G Navarra, L Nellen, H Salazar Ibarquen, S Ranchon, et al. “Observing muon decays in water Cherenkov detectors at the Pierre Auger Observatory”. In: *arXiv preprint astro-ph/0509238* (2005).
- [112] Romualdas Kalutis. “Photon Counting in Astrophotometry. Fundamentals and Some Advices for Beginners”. In: *Turkish Journal of Physics* 23.2 (1999), pp. 335–346.
- [113] Junius David Edwards and Samuel Fisher Pickering. *Permeability of rubber to gases*. 387. US Government Printing Office, 1920.
- [114] Jennifer L Marshall, Patrick Williams, Jean-Philippe Rheault, Travis Prochaska, Richard D Allen, and DL DePoy. “Characterization of the reflectivity of various black materials”. In: *Ground-based and Airborne Instrumentation for Astronomy V*. Vol. 9147. International Society for Optics and Photonics. 2014, 91474F.
- [115] Labsphere®. *Spectralon® Wavelength Calibration Standard*. URL: https://www.labsphere.com/labsphere-products-solutions/materials-coatings-2/targets-standards/diffuse-reflectance-standards/wavelength_standards/.
- [116] Humberto Cabrera, Jehan Akbar, Dorota Korte, Imrana Ashraf, Evelio E Ramirez-Miquet, Ernesto Marin, and Joseph Niemela. “Absorption spectra of ethanol and water using a photothermal lens spectrophotometer”. In: *Applied spectroscopy* 72.7 (2018), pp. 1069–1073.
- [117] CHERIC. *Chemical Engineering and Materials Research Information Center*. URL: <https://www.cheric.org/research/kdb/hcprop/cmprch.php>.
- [118] RD Birkhoff, LR Painter, and JM Heller Jr. “Optical and dielectric functions of liquid glycerol from gas photoionization measurements”. In: *The Journal of Chemical Physics* 69.9 (1978), pp. 4185–4188.

